BEAM-CAVITY INTERACTIONS IN HIGH POWER CYCLOTRONS

PAR

Lukas STINGELIN

ingénieur physicien diplômé EPF
de nationalité suisse et originaore de Muttenz (BL)

Zusammenfassung

Im Ringzyklotron des Paul Scherrer Instituts (PSI) wird ein hochintensiver Protonenstrahl von 72MeV auf 590MeV beschleunigt. Dies geschieht in vier Kavitäten sehr hoher Güte, die im Grundmode schwingen. Infolge seiner Zeitstruktur kann der Strahl in diesen Kavitäten parasitäre Schwingungsmoden höherer Ordnung (HOM) anregen. Messungen zeigen, dass diese zum Teil durch den Strahlspalt in die Vakuumkammer abgestrahlt werden.

Da man einerseits bis heute keine Mittel zur Verfügung hat, den potentiell schädlichen Einfluss dieser HOMs auf den Strahlbetrieb des Zyklotrons vorauszusagen und andererseits davon auszugehen ist, dass sie bei der Beschleunigung von noch höheren Strahlströmen eine Rolle spielen, beschäftigt sich diese Arbeit mit der Strahl-Kavitäts-Wechselwirkung.

Erste Berechnungen der Wechselwirkung eines Strahlpaketes mit einer Kavität wurden mit den Eigenmode- (E3), Zeitbereich- (T3) und Particle-In-Cell (TS3)-Lösern von MAFIA durchgeführt. Das strukturierte Gitter und die limitierte Rechenleistung von MAFIA verunmöglichen aber realistische Simulationen.

Da eine selbstkonsistente Lösung im Zeitbereich mit den heutigen Rechenanlagen nicht möglich ist, wird in dieser Arbeit ein vereinfachtes Rechenverfahren entwickelt: Der parallele Eigenlöser *Omega3P* vom *Stanford Linear Accelerator Center* (SLAC) ermöglicht erstmals, Eigenmoden des ganzen Ringzyklotrons zu berechnen. Die HF-Felder lassen sich durch diese Eigenmoden darstellen und deren Anregung durch den Strahlstrom kann im Frequenzbereich berechnet werden. Damit lassen sich die Trajektorien der Strahlpakete im statischen Feld der Sektormagnete, unter Berücksichtigung der Raumladungskräfte und des strahlangeregten elektromagnetischen Feldes, bestimmen.

Die quantitative Genauigkeit des Modells ist allerdings noch beschränkt. Einerseits, weil die Geometrie der simulierten Hochfrequenzstruktur stark vereinfacht werden muss, da sonst die Grenzen der verfügbaren Computer-Ressourcen gesprengt werden. Andererseits, weil stark absorbierende Oberflächen noch nicht genau genug simuliert werden können.

Simulationsresultate bestätigen, dass bis zu dem heute routinemässig beschleunigten Strahlstrom von ca. 2mA nur kleine Deformationen der Ladungsverteilung durch die angeregten Felder festzustellen sind. Mit dieser Arbeit wird ein Simulationswerkzeug zur Verfügung gestellt, welches für weitergehende Studien zur Leistungserhöhung von Hochstromzyklotronen verwendet werden kann.

Abstract

The ring cyclotron of the Paul Scherrer Institute (PSI) accelerates an intense proton beam from 72MeV up to 590MeV. This happens in four cavities of very high quality factor, oscillating in the fundamental mode. The beam can excite parasitic oscillation modes (HOMs), because of its time structure. Measurements showed that their field can leak out into the vacuum chamber.

Until now, there is no tool available to predict the potentially harmful effect of these HOMs onto the beam operation of the cyclotron. It is foreseeable that these effects might play a role if even higher beam currents have to be accelerated. This dissertation therefore deals with the numerical analysis and measurement of beam-cavity interactions.

First calculations for a single cavity, interacting with a proton bunch were performed with MAFIA's eigenmode- (E3), time domain- (T3) and particle-in-cell (TS3) solvers. However, the structured grid and the limited computing performance of MAFIA make realistic simulations impossible.

A simplified computation method is developed in this dissertation since a self-consistent simulation is impossible on today's computers: The parallel eigensolver *Omega3P* of the *Stanford Linear Accelerator Center* (SLAC) allowed us to calculate eigenmodes of the entire ring cyclotron for the first time ever. The rf fields are expanded onto a superposition of these modes and the excitation is calculated in frequency domain. Trajectories of the particles in the static magnetic field, superposed with the space charge fields and the beam excited HOMs, are then simulated.

However, the quantitative accuracy of this model is still limited. On the one hand, because of the simplification in the geometry of the simulated rf structure, which otherwise would lead to a problem size going beyond the available computing resources. On the other hand, because it is not yet possible to simulate strongly absorbing boundaries more accurately.

The simulation results confirm that up to proton beam currents of 2mA, corresponding to the routinely accelerated beam intensities, only a small deformation of the charge distribution appears. This thesis leads to a new simulation tool for further studies of intensity increases in high power cyclotrons.

Acknowledgments

Contents

Chapter 1

INTRODUCTION

The Paul Scherrer Institute (PSI) is a Swiss Federal Research Institute and operates one of the leading high intensity proton accelerators. The acceleration of the protons is achieved in three stages: The ion source is located in the high-voltage part of the Cockcroft-Walton 870keV DC preaccelerator. The protons are directed into the injector 2 cyclotron and are accelerated over about 80 turns up to 72MeV before they get extracted and transferred to the ring cyclotron. There the final energy of 590MeV is reached after about 220 revolutions.

When the accelerated protons are made to traverse thin rings of graphite (target M and E), they produce the world's most intense particle beams of pions and muons, which are brought to secondary beam areas in the experimental hall for particle physics, material science and solid-state physics experiments. About 63% of the proton beam is left after the two targets and reaches the neutron spallation source (SINQ). The neutrons are mainly used for solid-state physics and material science. Other applications of the proton facility are human cancer therapy and the development of radioisotopes for medical diagnostics.

Cancer therapy and a large fraction of the experiments require a stable and uninterrupted beam. To run the SINQ facility at its design current of 2mA, the primary current of the cyclotrons has to be increased to about 3mA. Therefore most of the development and upgrade activities are devoted to increasing the beam current and to improve the availability of the cyclotron. Both aspects are very important for the usefulness of high intensity cyclotrons, such as the *PSI "dream-machine"* [70] for Accelerator Driven Systems (ADS), e.g. the transmutation of radioactive waste.

In the last decade, a program of high priority was to study intensity limitations by analyzing space charge effects by *Adam* [1] and *Adelmann* [3]. This work lead to a better understanding of the beam dynamics of space charge dominated cyclotrons. Beam-cavity interactions, on the other hand, have never been analyzed in detail. In fact, the intense proton beam can excite electromagnetic fields in the cavities and the beam chamber, which eventually deteriorate the quality of the beam and lead to increased beam losses in the accelerator. The last publication on beam-cavity interactions in cyclotrons can be found in the proceedings of the "*Symposium on Separated Orbit Cyclotrons and Beam-Cavity Interactions*" [63] back in 1966.

However, the observation of beam excited modes in the main cavities lead to the

question of, whether or not beam-cavity interactions in high intensity machines really can be neglected. By using the computing power of today and applying state of the art numerical methods, this thesis sets out to answer this question.

1.1   The Sector-Focused Cyclotron

If particles are to remain isochronous with a fixed frequency of the accelerating voltage, the static magnetic fields must increase with radius to compensate the relativistic mass increase with the energy of the accelerated particles [13]. But, in a non-relativistic *Lawrence-Cyclotron*[1], this is limited by the requirement for the vertical focusing. The relativistic *Thomas-Cyclotron* [2] reaches the additional vertical focusing by adding a sinusoidal variation of the field with azimuth. The *sector-focusing* concept[3] finally improves the focusing properties of a relativistic cyclotron by a particular azimuthal variation of the static magnetic field in spiral form.

The most troublesome obstacle for the cyclotron designer is the occurrence of beam resonances [13, 61, 11], i.e. regions in which the radial or axial focusing oscillation (see section 2.4.1) is synchronous with some component of the electric or magnetic field, leading to coherent oscillation and, as a consequence, to the loss of the beam. In marked contrast to the synchrotron, where the operating point can be carefully selected to be as far as possible from all resonances, the cyclotron is forced to live with an operating mode which often involves direct passage through several major resonances. In a synchrotron such resonance transitions would be disastrous, in a cyclotron, due to the much smaller number of turns, resonance transitions can be accomplished, but only by a careful design study and careful field control. Therefore, it is of interest to simulate the effect of beam excited Higher Order Modes (HOMs) onto the stability of the beam.

In fact, with respect to beam-cavity interactions, the cyclotron might be situated between synchrotron and linear accelerators. Similar to synchrotrons, the particles are circulating around several times. But in contrast to synchrotrons they are extracted from the cyclotron after a relatively short time. This is similar to the case of linear accelerators, but in cyclotrons, there are several particle bunches of different energies interacting with the same rf structure.

1.1.1   The PSI Ring Cyclotron

The PSI ring cyclotron (see fig. 1.1 and 1.2) is a isochronous, separated orbit, sector focusing cyclotron with separated sectors. It has a fixed beam energy of 590 MeV at extraction, corresponding to 80% of the speed of light. It was built and commissioned in 1974. A continuous upgrade program enabled to increase the average current intensity from the design value of 100μA to about 2mA at present, corresponding to a beam power above 1MW. The 72 MeV beam from the injector cyclotron is injected into an orbit

---

[1]E.O. Lawrence in 1929
[2]L.H. Thomas in 1938
[3]developed in the 1950's
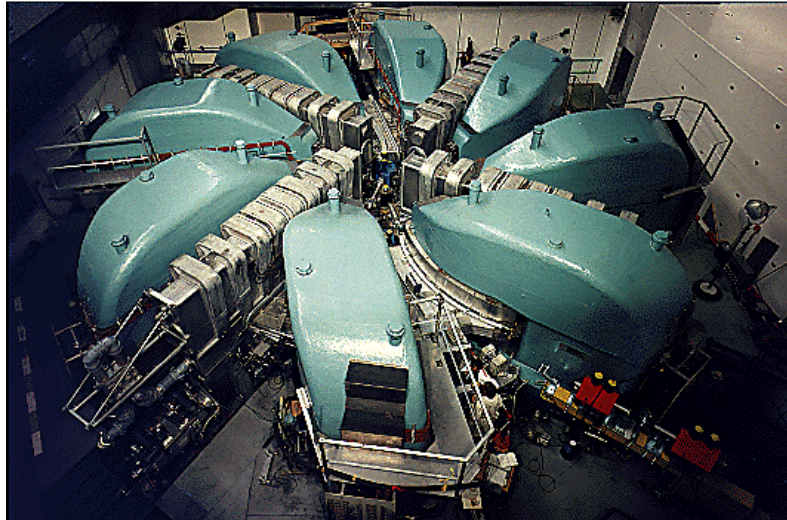
Figure 1.1: **Top view on PSI ring cyclotron. (Diameter ≈ 13m).** The four accelerating cavities, made of pure aluminum, are located between the green colored sector magnets. Their rectangular box-shape can be guessed underneath the eight stiffening yokes, which prevent the structure from collapsing due to the atmospheric pressure.
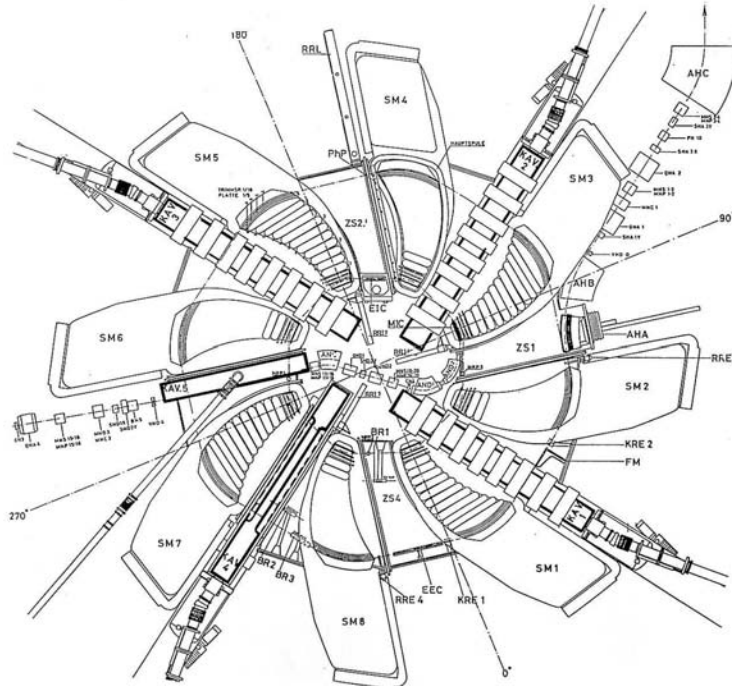
Figure 1.2: **Schematic view on beam plane of PSI ring cyclotron.** Sector magnets (SM1-SM8) hold the particles on their isochronous trajectory. The main cavities (KAV1-KAV4) provide the accelerating voltage and the flattop cavity (KAV5) is used at the third harmonic for improvement of the phase acceptance. The beam is injected from the left across KAV5.
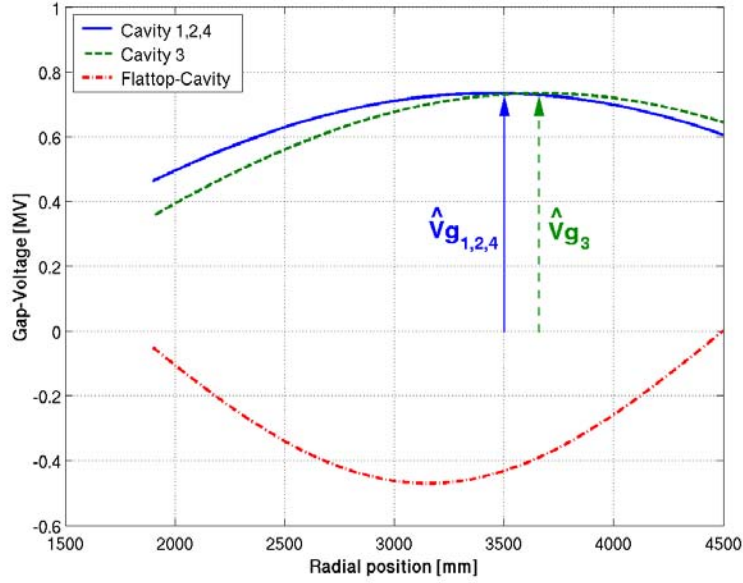
Figure 1.3: **Gap voltage in function of cyclotron radius.** The plot for cavity 3 corresponds to the voltage distribution in the new copper cavity. The location of this cavity is shifted outward by 10cm. Upper bounds of cavity voltages are denoted as $\hat{V}_g$ ($\approx$730kV). The flattop cavity is operated in decelerating mode, and its gap voltage is therefore negative.

in the center of the Ring, accelerated over about 220 revolutions and extracted at the full energy. The principle components of the ring cyclotron are eight sector magnets, with a total weight of 2000 t, four accelerator cavities (50 MHz), and a flattop cavity operating at the third harmonic (150 MHz). The resulting strong, phase-independent energy gain per revolution gives good turn separation and hence beam extraction, with low beam losses of about 0.03%. This is a mandatory condition for high current operation.

Cavity Parameters

Since the purpose of the cavities is to accelerate the particles by an electric rf field, one of the main parameters of the cavity is the *gap voltage* V_G. This parameter is related to the energy gain ΔU_{kin} for a particle of charge q and velocity v by

$$\Delta U_{kin} = q \left| \int_{z=0}^{d} \vec{E}_n(\vec{x}) e^{j\frac{\omega_n z}{v}} d\vec{x} \right| = qT(v) \int_{z=0}^{d} \vec{E}_n(\vec{x}) d\vec{x} \qquad (1.1)$$

$$V_G \equiv \int_{z=0}^{d} \vec{E}_n(\vec{x}) d\vec{x} \qquad (1.2)$$

with transit time correction T for a cavity of width d and a particle path along the z-direction. In the particular case of a cyclotron, the particles cross the same cavity gap several times at different radial positions and energies on their trajectory from injection to extraction.

In the case of the cyclotron, the particles get different energy "kicks" at different radial positions, as illustrated in the radial gap voltage distribution of the ring cyclotron cavities in figure 1.3.

If the cavity resonates with angular frequency ω, it stores electromagnetic field energy U_C and dissipates a part of the supplied power in its metallic walls. In function of this wall loss P_w, the parameters *shunt-impedance* R and *unloaded quality factor* Q_0 can be defined by

$$P_w = \frac{\hat{V}_G^2}{2R} \qquad\qquad Q_0 = \omega\frac{U_C}{P_w} \qquad\qquad (1.3)$$

for a gap voltage distribution with upper bound $\hat{V}_G$.

The main cavities are operated at the fundamental mode of 50.633MHz, corresponding to the 6th harmonic of the rotation frequency of the proton bunches in the cyclotron. The cavities are built of pure aluminum in a box shape geometry of height 3300mm (see figure 1.4 for a cross section). Electrodes are added for a coarse adjustment of the initial resonance frequency to correct for fabrication errors. An other positive effect of the electrodes is that they reduce the transit time effects. Unloaded quality factors are about 30'000 and the shunt-impedance reaches about 1MΩ. The resonance frequency is tuned by means of a hydraulic system to compensate for changes in air pressure and thermo-mechanical deformations.

The rf power for the main cavities is generated by a five stage amplifier chain, outside the accelerator vault, and transported to the cavity over a distance of roughly 40 m by an air filled 50Ω coaxial line. The cavity is coupled critically to this line by means of an inductive loop.

Cryogenic vacuum pumps are flanged directly to the main cavities, and serve to pump the entire ring cyclotron. The vacuum pressure is about 10^{-6}mbar.

The construction of the flattop cavity is basically the same as for the main cavities. The operating frequency of this cavity is at 151.89MHz, the third harmonic of the operating frequency of the main cavities, and its unloaded quality factor of about 28'000 is comparable to the quality factor of the main cavities.

In the course of an upgrading and maintenance program it is planned to replace the four accelerating cavities in the PSI 590 MeV Ring Cyclotron with more powerful ones. This will allow accelerating voltages above 1MV.

1.1.2   Space Charge Limitation

A particular property of the isochronous cyclotron is the lack of focusing forces in longitudinal direction[4] [1]. Therefore, the longitudinal space charge forces appear at much

---

[4]Beam propagation direction
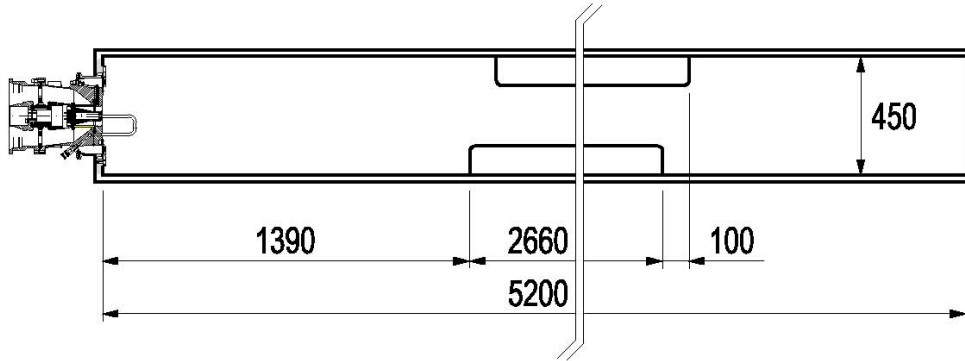
Figure 1.4: **Top view on main cavity at beam plane (Dimensions in mm).** The cavity is coupled to the coaxial line by means of an inductive loop, visible on the left.

lower beam currents than the transversal space charge forces. An analytical estimation of the space charge limits is given by *Joho* [36, 37] for the case of the PSI ring cyclotron. It is shown there that the transversal space charge limit appears at about 20mA, and that the longitudinal space charge limit is much lower, and depends on the gap voltage V_G as $I_{max} \propto V_G^3$, and is currently at about 2mA.

The transversal space charge forces decrease the focusing frequency, but do not change the fact that the beam remains focused in transversal direction. On the other hand, the longitudinal part of the space charge forces leads to an increased energy spread which accumulates during the particle propagation in the cyclotron. This smears out the turn separation and leads to increased extraction losses.

1.2   Phenomenology of Beam-Cavity Interaction

Figure 1.5 shows a set of particle bunches of charge q traveling through a cavity. It is supposed that the energies of the particles *in* one bunch are equal and that the cavity is tuned to the resonance frequency $f_0 = \omega_0/(2\pi)$. If there is no electromagnetic field in the cavity, an excitation seems to be impossible because the beam does not see any Lorentz forces and therefore can not absorb or induce any energy. However, there are always small oscillations induced by thermal motion observed as thermal noise. If at this moment the phase of this "Brownian motion" is equal to Ψ, one can represent the superposition of oscillations as

$$V_{Th} = \sum_i U_i \sin\left(\omega_0 t + \theta_i\right) = U_0 \sin\left(\omega_0 t + \Psi\right) \tag{1.4}$$

The mode amplitudes U_i and phases θ_i are arbitrary and only give evidence of the fact that every periodic function can be expressed as a sum of sines. All oscillations of this mode have the same damping by the finite conductivity of the cavity walls. For one particular oscillation with phase $\theta_i = \alpha$, $\vec{E}$ is maximal at the passage of q. This component of oscillation will rise faster than the others and, when it becomes observable
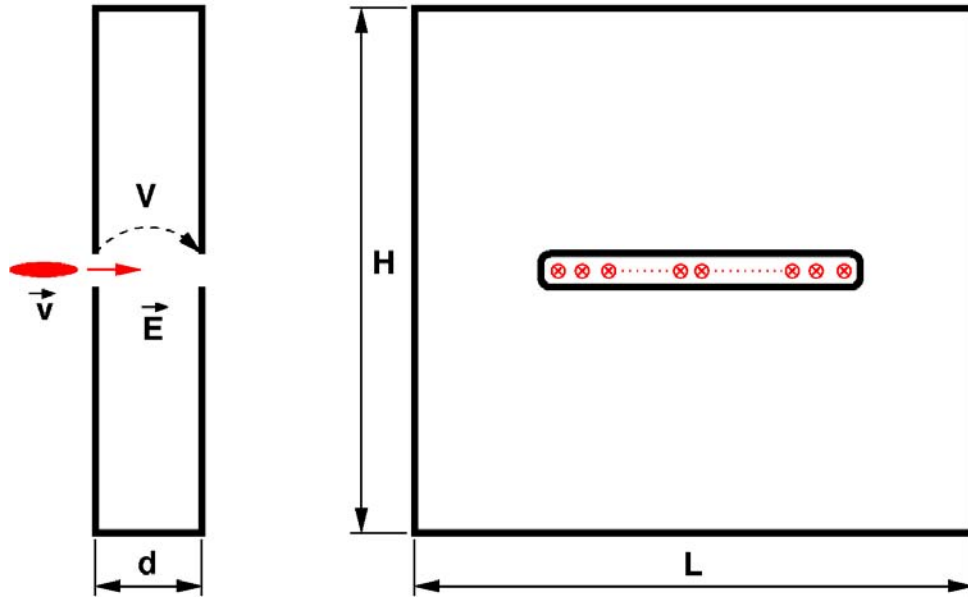
Figure 1.5: **Illustration of the cavity excitation by a particle bunch.**
View on a cross section of a box shaped cavity

macroscopically, remains singular. This is called the *principle of maximal excitation* by *Blaser* [12]. The phase of the excited oscillation is opposed to the phase of the exciting bunches. Otherwise one would have a perpetuum mobile: the particle bunch induces an electromagnetic field in the cavity, this field accelerates the particle even more and increases the electromagnetic field. But this is in contradiction to the energy conservation law.

If $V(t)$ is the time dependent cavity gap voltage during the excitation process, it has to fulfill the principle of energy conservation for the stored energy U_C in the cavity, the power lost in the cavity walls P_W and by beam loading P_Q. The beam loading can be approximated by the energy gain $\Delta E_{kin} = qV$ from the particles, when they cross the cavity gap. This is repeated at each period of time $\Delta t = 2\pi/\omega_0$ by the current $I_0 = q/\Delta t$. The energy conservation law can then be written as

$$\frac{dU_C}{dt} = P_W + P_Q = -\frac{V^2}{2R} + \frac{\Delta E_{kin}}{\Delta t} = -\frac{V^2}{2R} + \frac{\omega_0 qV}{2\pi} \tag{1.5}$$

R is the shunt impedance. Only the fundamental cavity mode is considered as lumped RCL equivalence circuit according to figure 1.6.
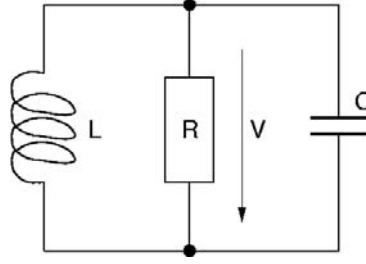
Figure 1.6: **Equivalence circuit of the cavity.** V is the amplitude of the gap voltage.

The total energy in the cavity is proportional to V^2 and consists of electric energy- and magnetic energy. These energies oscillate between electric- and magnetic field energy and on the average, have therefore to be equal. The total energy stored in the cavity can then be expressed at the time when all the energy is stored in the capacity C as

$$U_C = \frac{CV^2}{2} \tag{1.6}$$

In the case of a cyclotron with n turns located at x_k, the total beam-interaction is the sum over all interactions for the bunches k with velocity v_k (see figure 1.7).
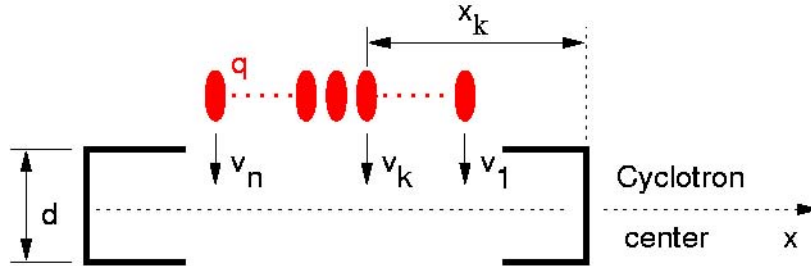
Figure 1.7: **Beam passage of n-bunches.** Top view on beam plane

For simplification of the equations, the cavity shape is supposed to be symmetric and the gap voltage approximated as $V_G(x)$ with upper bound $\hat{V}_G = V(t)$. The energy transfer per gap crossing can then be written as

$$\sum_{k=1}^{n} qV_G(x_i) \equiv \alpha q \hat{V}_G \tag{1.7}$$

for a constant $\alpha < n$. Introducing this generalized expression into the differential equation (1.5) of energy conservation for the fundamental mode:

$$C\frac{dV_G}{dt} = -\frac{V_G}{2R} + \frac{\omega_0 \alpha q}{2\pi} \tag{1.8}$$

With its general time dependent solution

$$V(t) = \frac{2\alpha q R \omega_0}{2\pi} \left(1 - e^{-\frac{\Delta t}{2RC}}\right) \tag{1.9}$$

One can see that the gap voltage in the cavity rises negative-exponentially during the bunch passage. An upper limit of the excitation is given by the static case for a time going to infinity in equation (1.9), and is simplified even more to

$$V_\infty \equiv \frac{2\alpha q R \omega_0}{2\pi} = 2\alpha R I_0 < 2n R I_0 \qquad (1.10)$$

An upper limit on the beam-excited amplitude is now given by setting $V_\infty = 2nRI_0$. The power dissipation in a cavity excited by a beam of $I_{DC} = 2$mA current and a shunt impedance of 1MΩ and 200 turns can reach values of $P_v = V_\infty^2/(2R) \approx 300$kW in the case of the cavities in the ring cyclotron, for example. This is comparable to the power losses in the walls of the cavity during beam production. For such an important excitation of the cavity mode it is required that

1. The sum over all the n beam bunch to cavity mode interactions is non zero

2. The resonance of the mode is a harmonic value of the bunch passing frequency

An other type of modes are the ones which have no beam excited gap voltage V_∞ as long as the beam is positioned perfectly in the horizontal plane. If the beam is moved slightly out of the horizontal plane of symmetry, the modes with vertical field distribution in the beam plane can also be excited. Though the amplitudes of excitations are small for small deflections of the beam, the effects can grow as the beam passes through the accelerator. The excitation left behind a cavity by one bunch can cause the next bunch to receive a greater deflection. This greater deflection means more excitation, and so on. This effect will be discussed in the following section:

1.2.1 Simple Theory for Vertical Beam-Cavity Interaction

An elegant analytical description of the beam-cavity interaction phenomena was developed by *Lee-Whiting* [44]. This simplified theory can also be used to find upper bounds for the growth of the excitation of Higher Order Modes (HOMs) with vertically deflecting forces. Focusing forces of the cyclotron are ignored for the following development.

If a cyclotron has N cavities and M orbit turns, the deflection in the beam-position r before cavity n can then be defined as $y_{r,n}$. The cavity-field strength parameter in cavity n is denoted as F_n. Assuming that the deflection in the next cavity can be expressed recursively in function of a coefficient C_r, it is

$$y_{r,n+1} = y_{r,n} + C_r F_n. \qquad (1.11)$$

If the field strength parameter F_n depends linearly on the deflections in all the turns at cavity n

$$F_n = \sum_{s=1}^{M} G_s y_{s,n}. \qquad (1.12)$$

The coefficient G_n represents an average for turn number s. Combining (1.11) with (1.12), one gets a linear relationship between the deflections at cavity $(n + 1)$ and deflections at cavity n.

The initial deflection y_{11} has to be regarded as given and $y_{M+1,1}$ has to be calculated. Defining a matrix $B_{r,s}$ by

$$\boldsymbol{B}_{r,s} \equiv C_r G_s \tag{1.13}$$

it can be shown that with trace Tr

$$\boldsymbol{B}^2 = \mathsf{Tr}(\boldsymbol{B})\boldsymbol{B} \tag{1.14}$$

It follows then by recursion that

$$\frac{y_{M+1,1}}{y_{1,1}} = 1 + \frac{\alpha \sum_{r=1}^{M} \sum_{s=1}^{M} G_r C_s}{1 - \alpha \sum_{r=2}^{M} \sum_{s=1}^{r-1} G_r C_s} \tag{1.15}$$

$$\alpha \equiv \frac{[1 + \mathsf{Tr}(\boldsymbol{B})]^N - 1}{\mathsf{Tr}(\boldsymbol{B})} \tag{1.16}$$

Equation (1.16) can now be used to obtain an upper bound growth for the case in which all the products $G_r C_s$ are small. Replacing G_r by an upper bound G, and C_s by an upper bound C, the previous equation yields

$$\frac{y_{M+1,1}}{y_{1,1}} < 1 + NM^2 GC. \tag{1.17}$$

In fact, the growth factor for the passage through one cavity is $1 + GC$; there are NM passages through cavities, and the beam excites each cavity M times.

1.3   Outline of the Analysis

With the commercial code MAFIA, it is possible to simulate a single cavity only. Measurements show that the electromagnetic fields of higher order modes leak out of the cavity into the vacuum chamber. The use of a different code is therefore inevitable.

A self-consistent calculation of the beam-cavity interaction in the cyclotron is currently out of scope due to the following problems:

- More than 1000 proton bunches with different energies propagate simultaneously through the cyclotron and interact mutually and with the excited HOMs. The huge amount of interacting proton bunches leads to a tremendous number of macro particles.

- In order to reach steady state, about 45'000 particle crossings have to be calculated, leading to more than 8 million time steps and consequently to noise problems.

In the Advanced Computations Department (ACD) of the Stanford Linear Accelerator Center (SLAC) a suite of 3D electromagnetic codes is under development to provide higher accuracy and to model larger problems through the combined use of unstructured grids and parallel processing. Especially the eigenmode solver Omega3P is capable of modeling very large complex structures and finding tightly clustered eigenvalues and makes the following calculation method possible:

1. Solve for a set of eigenmodes in the cyclotron structure (frequency domain). They are used as basis functions for the representation of the rf fields in the cyclotron in step 3 and 4.

2. Calculate the design trajectory of one bunch from injection to extraction in the cyclotron (time-domain). The position and velocity parameters are used in step 3.

3. Evaluate the amplitude of the beam-excited rf-modes (frequency domain).

4. Subsequently track one bunch, composed of a large set of macro particles, through these rf fields superposed with its space charge fields (time domain).

In addition, this method assumes that particle oscillations can be decoupled into movements in vertical and horizontal direction for the calculation of a fast space charge correction by a Particle In Cell Needle (PICN) model.

1.4   Organization of the Report

Starting from Maxwell's and Lorentz' equations, the theory necessary for a numerical analysis of beam-cavity interactions is outlined in chapter 2. There the mode expansion of the rf-fields and particle tracking with space charge correction are introduced. Implementation details and the validation of the simulation tools are presented in chapter 3. Simulation results and measured data are described and compared in chapter 4.

Chapter 2

DESCRIPTION FROM FIRST PRINCIPLES

A more formal description of the beam-cavity interaction can be found from an analysis based on Maxwell's equations similar to methods developed for quantum electro dynamics [60]. The mode expansion technique is used in order to reduce the problem to an analysis of a set of mode amplitudes. A Fourier transformation of the equations in frequency domain provides directly the field solution in steady state condition for a periodic excitation of the electromagnetic fields in the cavity by the current of a bunched proton beam. Time domain calculations on the other hand require to integrate for a relatively long time, until the modes are fully excited and steady state condition is reached. However, computing in time domain could provide a more self consistent description if heavy perturbations of the particle distributions occur by the excited fields.

2.0.1 The Partial Differential Equations

The homogeneous Maxwell equations are given by [35]

$$\nabla \times \vec{E} + \frac{\partial}{\partial t}\vec{B} = 0 \qquad\qquad \nabla \cdot \vec{B} = 0 \qquad (2.1)$$

where the Nabla operator[1] represents differential operator for curl and divergence. The inhomogeneous Maxwell equations read

$$\nabla \times \vec{H} - \frac{\partial}{\partial t}\vec{D} = \vec{J} \qquad\qquad \nabla \cdot \vec{D} = \rho \qquad (2.3)$$

Lorentz force density $\vec{L}$ from the electromagnetic fields acts onto the evolution of charged particles according to

$$\vec{L} = \rho\vec{E} + \vec{J} \times \vec{B} \qquad (2.4)$$

---
[1]

$$\nabla \equiv \begin{bmatrix} \frac{\partial}{\partial x} \\ \frac{\partial}{\partial y} \\ \frac{\partial}{\partial z} \end{bmatrix}, \qquad \nabla \cdot \vec{a} \equiv div(\vec{a}), \qquad \nabla \times \vec{a} \equiv curl(\vec{a}), \qquad \nabla\varphi \equiv grad(\varphi) \qquad (2.2)$$

Where the meaning of the symbols are $\vec{E}(\vec{x}, t)$ for electric field, $\vec{B}(\vec{x}, t)$ for magnetic induction, $\vec{D}(\vec{x}, t)$ for electric displacement field, $\vec{H}(\vec{x}, t)$ for magnetic field, $\rho(\vec{x}, t)$ for density of charge and $\vec{J}(\vec{x}, t)$ for the density of current

$$\vec{J}(\vec{x}, t) = qn(\vec{x}, t)\vec{v}(\vec{x}, t) \qquad\qquad \rho(\vec{x}, t) = qn(\vec{x}, t) \qquad\qquad (2.5)$$

$$n(\vec{x}, t) = \frac{N}{V} \int f(\vec{x}, \vec{v}, t)dv^3 \qquad\qquad n(\vec{x}, t)\vec{v}(\vec{x}, t) = \frac{N}{V} \int \vec{v}f(\vec{x}, \vec{v}, t)dv^3 \qquad (2.6)$$

with the distribution function $f(\vec{x}, \vec{v}, t)$, for a large number of particles N, volume of integration V and charge q of one particle.

In the notation of potential vector $\vec{A}(\vec{x}, t)$ in the Coulomb gauge with $\nabla \cdot \vec{A} = 0$ for

$$\vec{B} = \nabla \times \vec{A} \qquad\qquad \vec{E} = -\frac{\partial}{\partial t}\vec{A} - \nabla\Phi \qquad\qquad (2.7)$$

the equations are rewritten for the case of vacuum where $\vec{B} = \mu_0\vec{H}$ and $\vec{D} = \varepsilon_0\vec{E}$ and with linear operator $\mathfrak{L}$ for the Laplace operator[2] and reduced excitation $\vec{F}(\vec{x}, t)$

$$\mathfrak{L} = c^2\triangle \qquad\qquad \vec{F}(\vec{x}, t) = c^2\mu_0(\vec{J} - \frac{\partial}{\partial t}\varepsilon_0\nabla\Phi) \qquad\qquad (2.9)$$

and the Poisson equation for the electrostatic potential of the charges [35]

$$\triangle\Phi = -\frac{\rho}{\varepsilon_0} \qquad\qquad \Phi = \frac{1}{4\pi\varepsilon_0} \int \frac{\rho(\vec{x}', t)}{|\vec{x} - \vec{x}'|}d^3x' \qquad\qquad (2.10)$$

This leads to the boundary condition problem with linear partial differential equation of second order:

$$\frac{\partial^2}{\partial t^2}\vec{A} = \mathfrak{L}\vec{A} + \vec{F}(\vec{x}, t) \qquad\qquad (2.11)$$

Satisfying the boundary conditions of $\vec{E}$ for the perfect electric conducting cavity walls S with normal unity vector $\hat{n}$

$$\hat{n} \times \vec{E}(\vec{x} \in S, t) \equiv 0 \qquad\qquad (2.12)$$

yields the boundary condition on $\vec{A}$ with no volume charges on the surface and a non-static electric tangential $\vec{A}$ field

$$\hat{n} \times \vec{A}(\vec{x} \in S, t) \equiv 0 \qquad\qquad (2.13)$$

The vector fields can be expanded onto a complete set of orthogonal basis-functions $\vec{\xi}_n(\vec{x})$:

$$\vec{A}(\vec{x}, t) = \sum_n a_n(t)\vec{\xi}_n(\vec{x}) \qquad\qquad \vec{F}(\vec{x}, t) = \sum_n F_n(t)\vec{\xi}_n(\vec{x}) \qquad (2.14)$$

$$\vec{f}(\vec{x}) = \sum_n f_n\vec{\xi}_n(\vec{x}) \qquad\qquad \vec{g}(\vec{x}) = \sum_n g_n\vec{\xi}_n(\vec{x}) \qquad (2.15)$$

---

[2]

$$\triangle \equiv \nabla^2 = \frac{\partial^2}{\partial x^2} + \frac{\partial^2}{\partial y^2} + \frac{\partial^2}{\partial z^2} \qquad\qquad (2.8)$$

With initial conditions $\vec{f}$ and $\vec{g}$

$$\vec{A}(t=0,\vec{x}) = \vec{f}(\vec{x}) \qquad\qquad \frac{\partial \vec{A}}{\partial t}(t=0,\vec{x}) = \vec{g}(\vec{x}) \qquad (2.16)$$

The choice of Coulomb gauge gives the advantage of a divergence-free field solution and an additional set of curl-free functions for the equation $l_n \vec{F}_n = \nabla \Phi_n$ is therefore not needed. On the other hand, as explained in *Greiner* [31], the Coulomb gauge leads to an intrinsically non-covariant formulation of the theory. But this is no disadvantage because the beam-excited cyclotron-fields are located in the fixed laboratory frame.

The basis-functions $\vec{\xi}_n(\vec{x})$ can be chosen to be a set of eigenmodes of the homogeneous boundary condition problem

$$\mathfrak{L}\vec{e}_n + \lambda_n \vec{e}_n = 0 \qquad\qquad \text{with} \quad \lambda_0 \le \lambda_1 \le \ldots \le \lambda_n \to \infty \qquad (2.17)$$

satisfying (2.13) with electric-field distribution $\vec{e}_n(\vec{x})$. The corresponding magnetic-field of the mode is related by the curl-equations in (2.1)

$$\omega_n \vec{b}_n(\vec{x}) \equiv \nabla \times \vec{e}_n(\vec{x}) \qquad (2.18)$$

with phase-difference of $\pi/2$ to the electric field. These electric and magnetic eigen-fields are calculated directly by the eigensolver. Total energy U_n of mode n can be normalized to

$$U_n = \frac{\varepsilon_0}{2} \int\limits_V |\vec{e}_n(\vec{x})|^2 dx^3 = \frac{\mu_0}{2} \int\limits_V |\vec{b}_n(\vec{x})|^2 dx^3 = \frac{\varepsilon_0}{2} \qquad (2.19)$$

and satisfies the orthogonality relation

$$\int\limits_V \vec{e}_m(\vec{x}) \vec{e}_n(\vec{x}) dx^3 = \delta_{mn} \qquad (2.20)$$

They are coupled to the electric and magnetic solutions of the problem by the potential equations (2.7) and the mode expansion (2.14) with space-charge term $\nabla \Phi$:

$$\vec{E}(\vec{x},t) = -\sum_n \dot{a}_n(t) \vec{e}_n(\vec{x}) - \nabla \Phi(\vec{x}) \qquad \vec{B}(\vec{x},t) = -\sum_n \omega_n a_n(t) \vec{b}_n(\vec{x}) \qquad (2.21)$$

Using equation (2.11),the precedent equations can be rewritten as

$$\partial_t^2 \vec{A} = \sum_n \ddot{a}_n(t) \vec{e}_n(\vec{x}) = \mathfrak{L}\vec{A} + \vec{F}(\vec{x},t) = \sum_n a_n(t) \mathfrak{L}\vec{e}_n(\vec{x}) + \sum_n F_n(t) \vec{e}_n(\vec{x}) \qquad (2.22)$$

$$= -\sum_n a_n(t) \lambda_n \vec{e}_n(\vec{x}) + \sum_n F_n(t) \vec{e}_n(\vec{x}) \qquad (2.23)$$

Leading to the following equation for the time-dependent variables:

$$\ddot{a}_n(t) = -\lambda_n a_n(t) + F_n(t) \qquad (2.24)$$

with the projection of the excitation

$$F_n(t) = \int\limits_V \vec{F}(\vec{x},t) \vec{e}_n(\vec{x}) dx^3 \qquad (2.25)$$

The fields are therefore represented by a superposition of uncoupled oscillators, driven by the excitation F_n.

2.0.2   Cavity with Wall Losses

If the cavity wall losses are taken into account, the spectrum of the modes changes from a Dirac function to a resonance curve with a well defined bandwidth. An excitation of a mode with a current results in a finite mode amplitude limited by the power losses in the wall. The ohmic wall losses are given [20] by the wall currents $\vec{J}_S$:

$$P_L = \frac{R_m}{2} \oint_S \vec{J}_S(\vec{x}) \vec{J}_S(\vec{x})^* dS = \frac{R_m}{2} \oint_S \vec{H}(\vec{x}) \vec{H}(\vec{x})^* dS \qquad (2.26)$$

With wall surface resistivity [35] R_m (j defines the imaginary part[3]):

$$R_m = \mathfrak{Re}(Z_m) = \mathfrak{Re}\left(\frac{1-j}{\sigma_m \Delta_m}\right) = \frac{1}{\sigma_m \Delta_m} \qquad (2.28)$$

and skin depth [35] [30] Δ_m of the metal at frequency ω_0:

$$\Delta_m = \sqrt{\frac{2}{\omega_0 \mu \sigma_m}} \qquad (2.29)$$

and conductivity σ_m of the metal. The symbols ε and μ stand for the *real* electric permittivity and magnetic permeability ($\vec{B} = \mu\vec{H}, \vec{D} = \varepsilon\vec{E}$). The magnetic field of an eigenmode with resonance frequency ω according to (2.1 and 2.3) is a solution of

$$\nabla \times \nabla \times \vec{H} - k^2 \vec{H} = 0 \qquad\qquad\qquad k = \frac{\omega}{c} \qquad (2.30)$$

The corresponding electric field in the volume is given by (2.3)

$$\vec{E} = -\frac{j}{\omega\varepsilon} \nabla \times \vec{H} \qquad (2.31)$$

On the boundary it is required by Ohm's law and (2.3) that $\hat{n} \times \vec{E} = -Z_m \vec{H}_t$ where the tangential component of the magnetic field is denoted by $\vec{H}_t$. Substituting into (2.31), the boundary condition for the magnetic field can then be stated in the form

$$\hat{n} \times \nabla \times \vec{H} = -j\varepsilon\omega Z_m \vec{H}_t \qquad (2.32)$$

The source free modes in a *lossy* cavity exist only for complex values of ω and k. Eigenmodes are no longer orthogonal and electric field vectors are not exactly orthogonal to the boundaries. The surface impedance Z_m is a function of ω_n and should be evaluated for the complex ω. However, for many practical applications the imaginary part of ω is very small relative to the real part, as in the case of metals, so that the imaginary part of ω can be neglected in evaluating Z_m for perfectly fields for perfectly conducting boundary conditions and calculating the wall losses as perturbation.

---

[3]

$$e^{j\pi} + 1 = 0, \quad j^2 = -1, \quad z = a + jb \Leftrightarrow a = \mathfrak{Re}(z) \wedge b = \mathfrak{Im}(z), \quad a, b \in \mathbb{R}, z \in \mathbb{C} \qquad (2.27)$$

According to the conservation law of electromagnetic energy, the relation of stored energy U to power loss is related by

$$P_V = -\frac{dU}{dt} \qquad\qquad P_V = P_C + P_E \qquad (2.33)$$

with wall losses P_C and external coupling losses P_E. These parameters can be found using Maxwell's equations (2.1 and 2.3) multiplied with $\vec{H}$ and $\vec{E}$ respectively and subtracted. The relation for density of energy $u(\vec{x}, t)$ and Poynting vector $\vec{S}(\vec{x}, t)$ reads after manipulation with the vector operator identity $\nabla \cdot (\vec{A} \times \vec{B}) = \vec{B} \cdot \nabla \cdot \vec{A} - \vec{A} \cdot \nabla \times \vec{B}$

$$\nabla \cdot \vec{S} + \frac{\partial}{\partial t} u = -\vec{E} \cdot \vec{J} \qquad\qquad u = \frac{1}{2}(\vec{E}\vec{D} + \vec{H}\vec{B}) \qquad (2.34)$$

$$\vec{S} = \vec{E} \times \vec{H} \qquad (2.35)$$

Integrating over the volume leads to the total energy and surface losses after applying the Gaussian integration theorem

$$U = \frac{1}{2} \int_V \left(\varepsilon_0 |\vec{E}|^2 + \mu_0 |\vec{H}|^2 \right) dV \qquad\qquad P_V = \oint_{\partial V} \left(\vec{E} \times \vec{H} \right) d\vec{A} \qquad (2.36)$$

The power losses depend linearly with total energy and the loaded quality factor of the cavity can therefore be defined as

$$Q \equiv \omega_0 \frac{U}{P_V} \qquad (2.37)$$

If no excitation is present, the field energy in the cavity decays according to (2.33 and 2.34) combined with (2.37) as

$$P_V = U \frac{\omega}{Q} = -\frac{dU}{dt} \qquad\qquad \longrightarrow \qquad\qquad U = U_0 \cdot e^{-t/\tau_u} \qquad (2.38)$$

The field energy on the other hand depends quadratically on the field amplitudes and therefore the decay time gets

$$\tau_a = 2\tau_u = \frac{2Q}{\omega_0} \qquad (2.39)$$

Extending the differential equation (2.24) with a damping term r_n

$$\ddot{a}_n(t) = -\lambda_n a_n(t) - r_n \dot{a}_n(t) + F_n(t) \qquad (2.40)$$

and substituting the trial solution $A = A_0 e^{\omega t}$ into the homogeneous differential equation yields

$$\omega = -\frac{r_n}{2} \pm j\sqrt{\lambda_n - \left(\frac{r_n}{2}\right)^2} = -r_n \pm j\omega_L \qquad (2.41)$$

corresponding to a harmonic with exponential envelope if $\lambda_n > (r_n/2)^2$ with field evolution

$$A = A_0 e^{-\frac{r_n}{2} t} e^{j\omega_L t} \qquad (2.42)$$

Here ω_L corresponds to the shifted resonance frequency due to the additional damping term r_n. Finally, the parameter r_n can now be identified in (2.38 and 2.39) as

$$r_n = \frac{2}{\tau_a} = \frac{\omega_0}{Q} \qquad (2.43)$$

2.1   Solution in Frequency Domain

Consideration of the space-charge variation term $\partial \nabla \Phi / \partial t$ in (2.9) would lead to a self consistent description of the beam-cavity interaction and could be integrated by time stepping. However, it is desirable to calculate the field excitation in frequency domain and to neglect the bunch deformation in the excitation term (rigid bunch approximation). The beam excited cyclotron fields are calculated directly for steady state condition this way, corresponding to infinite operation time after switching-on the beam. The effect of the excited fields onto the particle distribution can then be simulated in a subsequent step. This approximation is valid as long as the shape of particle bunches is not significantly changed by the excited fields and no non-linear beam resonances are excited.

2.1.1   Fourier Decomposition of the Excitation

If the excitation signal (2.9) can be decomposed into a Fourier series the coefficients can be developed according to

$$F_n(t) = \frac{C_n}{2} + \sum_{m=1}^{\infty} \boldsymbol{K}_{nm} \cos(m\omega_0 t) + \sum_{m=1}^{\infty} \boldsymbol{L}_{nm} \sin(m\omega_0 t) \tag{2.44}$$

With the Fourier-Ansatz for the function $a_n(t)$

$$a_n(t) = \frac{c_n}{2} + \sum_{m=1}^{\infty} \boldsymbol{a}_{nm} \cos(m\omega_0 t) + \sum_{m=1}^{\infty} \boldsymbol{b}_{nm} \sin(m\omega_0 t) \tag{2.45}$$

$$\dot{a}_n(t) = -\sum_{m=1}^{\infty} m\omega_0 \boldsymbol{a}_{nm} \sin(m\omega_0 t) + \sum_{m=1}^{\infty} m\omega_0 \boldsymbol{b}_{nm} \cos(m\omega_0 t) \tag{2.46}$$

$$\ddot{a}_n(t) = -\sum_{m=1}^{\infty} m^2\omega_0^2 \boldsymbol{a}_{nm} \cos(m\omega_0 t) - \sum_{m=1}^{\infty} m^2\omega_0^2 \boldsymbol{b}_{nm} \sin(m\omega_0 t) \tag{2.47}$$

introduced into (2.24) yields the separated equations for c_n, $\boldsymbol{a}_{nm}$ and $\boldsymbol{b}_{nm}$.

$$\lambda_n c_n = C_n \tag{2.48}$$

$$-m^2\omega_0^2 \boldsymbol{a}_{nm} + r_n m\omega_0 \boldsymbol{b}_{nm} + \lambda_n \boldsymbol{a}_{nm} = \boldsymbol{K}_{nm} \tag{2.49}$$

$$-m^2\omega_0^2 \boldsymbol{b}_{nm} - r_n m\omega_0 \boldsymbol{a}_{nm} + \lambda_n \boldsymbol{b}_{nm} = \boldsymbol{L}_{nm} \tag{2.50}$$

with the solutions

$$c_n = \frac{C_n}{\lambda_n} \tag{2.51}$$

$$\boldsymbol{a}_{nm} = \frac{\boldsymbol{K}_{nm}(\lambda_n - m^2\omega_0^2) - \boldsymbol{L}_{nm} m\omega_0 r_n}{(\lambda_n - m^2\omega_0^2)^2 + m^2\omega_0^2 r_n^2} \tag{2.52}$$

$$\boldsymbol{b}_{nm} = \frac{\boldsymbol{L}_{nm}(\lambda_n - m^2\omega_0^2) + \boldsymbol{K}_{nm} m\omega_0 r_n}{(\lambda_n - m^2\omega_0^2)^2 + m^2\omega_0^2 r_n^2} \tag{2.53}$$

for the Fourier coefficients of the potential vector, weighted by the resonance curve of the mode. Where the C_n, $\boldsymbol{K}_{nm}$ and $\boldsymbol{L}_{nm}$ depend on the current distribution of the excitation and still have to be determined. It follows from (2.52 and 2.53) that only modes with a resonance frequency close to a harmonic can be excited significantly by this signal. The damping term r_n limits the amplitudes of the modes.

Fourier Decomposition of Flying Particle Bunches

One particle bunch flying with velocity $\vec{v}_i$ can be approximated as a one dimensional wave with transversal density function of a Dirac function $\delta_{Ti}(\vec{x})$. If for a simplified description of the beam profile, the density function is supposed to be a normalized Gaussian with periodicity Λ:

$$f(z) = \frac{1}{\sigma\sqrt{2\pi}}e^{-\frac{z^2}{2\sigma^2}} \qquad\qquad f(z+\Lambda) = f(z) \qquad\qquad (2.54)$$

The periodicity can also be constructed by convolution of one Gaussian $G(z)$ with a train of Dirac functions $D(z)$ with periodicity Λ

$$f(z) = G * D(z) \equiv \int\limits_{-\infty}^{\infty} G(z-\zeta)D(\zeta)d\zeta \qquad\qquad (2.55)$$

The particle bunch is propagating with velocity v and the argument z must be replaced by $z - vt$ and with the bunch crossing frequency $\omega_0 = 2\pi v/\Lambda$

$$
\begin{aligned}
f(t,z) &= \frac{\omega_0}{2\pi v} + \frac{\omega_0}{\pi v}\sum_{m=1}^{\infty} e^{-\frac{(m\omega_0\sigma)^2}{2v^2}} \cos\left(m\frac{\omega_0}{v}z - m\omega_0 t\right) \\
&= \frac{\omega_0}{2\pi v} + \frac{\omega_0}{\pi v}\sum_{m=1}^{\infty} e^{-\frac{(m\omega_0\sigma)^2}{2v^2}} \cos\left(m\frac{\omega_0}{v}z\right)\cos\left(m\omega_0 t\right) \\
&\quad + \frac{\omega_0}{\pi v}\sum_{m=1}^{\infty} e^{-\frac{(m\omega_0\sigma)^2}{2v^2}} \sin\left(m\frac{\omega_0}{v}z\right)\sin\left(m\omega_0 t\right)
\end{aligned}
\qquad (2.56)
$$

as illustrated in figure (2.1). Comparison with (2.44) yields, after neglecting the bunch deformation and with projection of the particle distributions onto the modes the coefficients

$$C_n = \sum_i \frac{\omega_0}{2\pi v_i}\int\limits_{V} \vec{\delta}_{Ti}(\vec{x})\vec{e}_n(\vec{x})dV \qquad\qquad (2.57)$$

$$\boldsymbol{K}_{nm} = \sum_i \frac{\omega_0}{\pi v_i}e^{-\frac{(m\omega_0\sigma_i)^2}{2v_i^2}}\int\limits_{V}\cos\left(m\frac{\omega_0}{v_i}z\right)\vec{\delta}_{Ti}(\vec{x})\vec{e}_n(\vec{x})dV \qquad (2.58)$$

$$\boldsymbol{L}_{nm} = \sum_i \frac{\omega_0}{\pi v_i}e^{-\frac{(m\omega_0\sigma_i)^2}{2v_i^2}}\int\limits_{V}\sin\left(m\frac{\omega_0}{v_i}z\right)\vec{\delta}_{Ti}(\vec{x})\vec{e}_n(\vec{x})dV \qquad (2.59)$$
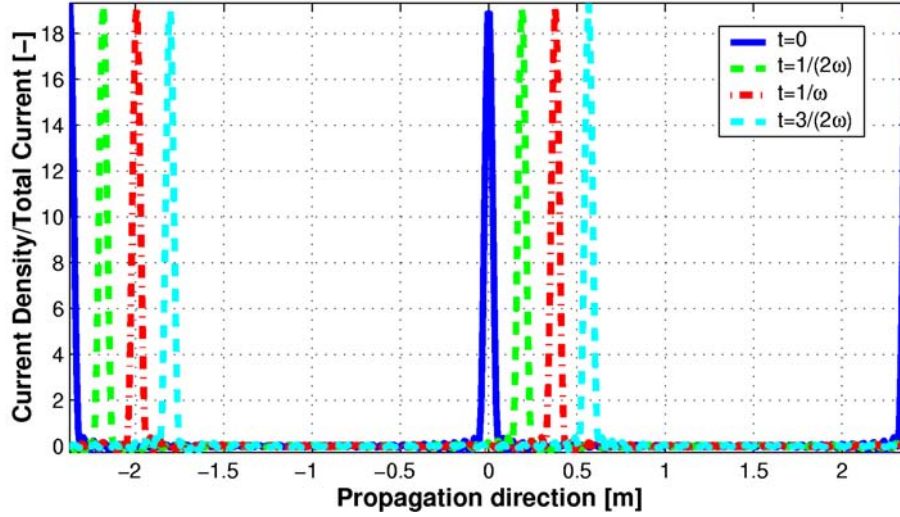
Figure 2.1: **Synthesis of the Bunches with 40 Fourier components.** Il-
lustration of equation (2.56) for different time steps. The parti-
cle bunches are propagating to the right.

The coefficients C_n lead to an asymmetry of positive to negative amplitude of the mode
corresponding to the static magnetic field induced by the DC component of the beam
current. The action of the beams to cyclotron fields is then the superposition of all the
excitation terms provided by trains of Gaussians at different velocities and positions.
For the determination of these parameters, a single particle trajectory is calculated
from injection to extraction. This yields, after scaling of the distribution function $f(t,z)$
to the DC-value of the beam current and projection of the particle distributions onto the
modes, the coefficients C_n, $\boldsymbol{K}_{nm}$ and $\boldsymbol{L}_{nm}$ in (2.57, 2.58 and 2.59). It results in that only
modes with electric field components in beam propagation direction can be excited by
the beam and that the amplitudes are proportional to the beam current. For a short
bunch with approximation $\sigma \to 0$, eq. (2.58 and 2.59) indicate that the mean value C_n
is half of the oscillating mode values $\boldsymbol{K}_{nm}, \boldsymbol{L}_{nm}$. This relationship is called the *short
bunch approximation* [16].

2.1.2   A Note on Mode Coupling and Orthogonality

Strictly speaking, the eigenmodes of a cavity with wall losses are, in general, no longer
orthogonal. This can be illustrated in a way analogous to *Slater* [68]. In order to
calculate

$$\int_V \vec{e}_a \vec{e}_b \, dV \tag{2.60}$$

the following vector identity provides interesting results.

$$\begin{aligned}
\nabla \cdot (\vec{e}_b \times [\nabla \times \vec{e}_a]) - \nabla \cdot (\vec{e}_a \times [\nabla \times \vec{e}_b]) &= (\nabla \times \vec{e}_a) \cdot (\nabla \times \vec{e}_b) \\
&\quad - \vec{e}_b \cdot (\nabla \times \nabla \times \vec{e}_a) - (\nabla \times \vec{e}_b) \cdot (\nabla \times \vec{e}_a) \\
&\quad + \vec{e}_a \cdot (\nabla \times \nabla \times \vec{e}_b)
\end{aligned} \tag{2.61}$$

Canceling terms and using (2.17), this equation can be rewritten as

$$\nabla \cdot (\vec{e}_b \times [\nabla \times \vec{e}_a]) - \nabla \cdot (\vec{e}_a \times [\nabla \times \vec{e}_b]) = (\lambda_a - \lambda_b)\vec{e}_a\vec{e}_b \tag{2.62}$$

By Gauss' integration theorem and Maxwell's equations (2.1 and 2.3), the volume integral can be transformed to

$$-j \oint_{\partial V} \hat{n} \left(\omega_a \vec{e}_b \times \vec{b}_a - \omega_a \vec{e}_a \times \vec{b}_b \right) dA = (\lambda_a - \lambda_b) \int_V \vec{e}_a \vec{e}_b dV \tag{2.63}$$

The expressions in the surface integrals can be rewritten in the form $b_a \cdot (\hat{n} \times \vec{e}_b)$ and $b_b \cdot (\hat{n} \times \vec{e}_a)$. But now, in the case with lossy cavity walls, the electric field vectors have a contribution parallel to the boundary and in general the left hand side of the integral no longer vanishes. However for practical applications, the approximation of the fields by eigenmodes with ideal boundary conditions is usually sufficient.

2.1.3 A Note on Coupling of the Modes to the Beam

If the effect of the excited modes onto the beam parameters has to be taken into account, additional variables for the Fourier components of the excitation can be introduced.

$$K = K_0 + \sum_i F_i \xi_i \qquad\qquad L = L_0 + \sum_i G_i \eta_i \tag{2.64}$$

with injection parameters $\xi_0 = \eta_0 = 0$. The variables $\boldsymbol{K}_{nm}$ and $\boldsymbol{L}_{nm}$ are abbreviated by K and L, and $\boldsymbol{a}_{nm}$ and $\boldsymbol{b}_{nm}$ to a and b in this section. K_0 and L_0 represent the unperturbed excitation parameters according to (2.58 and 2.59) and the unknowns ξ_i, η_i the perturbation due to the excited modes. Assuming that beam dynamics imply an effect of the amplitude components to the beam parameters described by the parameters M_i, N_i, P_i and S_i in a recursive form, then the equation for the deviation can be written as

$$\xi_{i+1} = \xi_i + M_i a + N_i b \qquad\qquad \eta_{i+1} = \eta_i + P_i a + S_i b. \tag{2.65}$$

Introducing these equations into (2.52 and 2.53), a system of N linear equations can be found for the ξ_i and η_i with $i = 1 \ldots N$. The solution of this system provides then the mode amplitudes of the coupled system of fields interacting with particles.

2.2 Solution in Time Domain

After correction for wall losses in (2.40), the time evolution of mode amplitudes can be formulated as the following differential equation problem

$$\ddot{a}_n(t) = -\lambda_n a_n(t) - r_n \dot{a}_n(t) + F_n(t) \tag{2.66}$$

with the initial conditions

$$a_n(0) = f_n \qquad\qquad \dot{a}_n(0) = g_n \tag{2.67}$$

This gives the general solution of the harmonic differential equation $\ddot{\alpha}_n(t) + r_n \dot{\alpha}_n(t) + \lambda_n \alpha_n(t) = 0$ for the case of weak damping $(r_n^2 < 4\lambda_n)$

$$\alpha_n(t) = e^{\frac{-r_n}{2}t} \left\{ C_n \cos\left(\sqrt{\lambda_n - \frac{r_n^2}{4}}t\right) + S_n \sin\left(\sqrt{\lambda_n - \frac{r_n^2}{4}}t\right) \right\} \qquad (2.68)$$

Then the particular solution β_n can be found by Green's method:

$$\beta_n = \int\limits_0^t \left\{ \frac{e^{\frac{-r_n}{2}[t-s]}}{\sqrt{\lambda_n - \frac{r_n^2}{4}}} \sin\left((t-s)\sqrt{\lambda_n - \frac{r_n^2}{4}}\right) F_n(s) \right\} ds \qquad (2.69)$$

This yields the solution of the differential equation as superposition of transient effect and steady state evolution.

$$\vec{A}(t, \vec{x}) = \sum_n e^{\frac{-r_n}{2}t} \left\{ f_n \cos\left(\sqrt{\lambda_n - \frac{r_n^2}{4}}t\right) + \frac{g_n}{\sqrt{\lambda_n - \frac{r_n^2}{4}}} \sin\left(\sqrt{\lambda_n - \frac{r_n^2}{4}}t\right) \right\} \vec{e}_n(\vec{x})$$

$$+ \sum_n \int\limits_0^t \left\{ \frac{e^{\frac{-r_n}{2}(t-s)}}{\sqrt{\lambda_n - \frac{r_n^2}{4}}} \sin\left([t-s]\sqrt{\lambda_n - \frac{r_n^2}{4}}\right) F_n(s)ds \right\} \vec{e}_n(\vec{x})$$

$$(2.70)$$

where the first transient part vanishes for $t \to \infty$ and there remains for long evolution time:

$$\vec{A}(t, \vec{x}) = \sum_n \int\limits_0^t \left\{ \frac{e^{\frac{-r_n}{2}(t-s)}}{\sqrt{\lambda_n - \frac{r_n^2}{4}}} \sin\left([t-s]\sqrt{\lambda_n - \frac{r_n^2}{4}}\right) F_n(s)ds \right\} \vec{e}_n(\vec{x}) \qquad (2.71)$$

which can be reduced by the convolution of the Laplace transformation $\mathfrak{L}$

$$\vec{A}(t, \vec{x}) = \sum_n (B_n *_L F_n)\vec{e}_n(\vec{x}) \qquad (2.72)$$

$$B_n(t) \equiv \frac{e^{\frac{-r_n}{2}t}}{\sqrt{\lambda_n - \frac{r_n^2}{4}}} \sin\left(t\sqrt{\lambda_n - \frac{r_n^2}{4}}\right) \qquad (2.73)$$

and due to the convolution theorem

$$\mathfrak{L}[B_n *_L F_n(t)](z) = \mathfrak{L}[B_n(t)](z) \cdot \mathfrak{L}[F_n(t)](z) \qquad (2.74)$$

This expression can be evaluated, if the excitation terms F_n are known preliminary for all times. Unfortunately, the excitation term also gets affected by the Lorentz forces of the excited fields and, strictly speaking, should be evaluated in time and integrated simultaneously with the field equations. This results in self consistent description of beam cavity interaction particularly interesting for the study of resonance phenomena at higher frequencies.

2.3   Particular Case of the Fundamental Mode

Assuming that the E-field distribution of the fundamental mode can be approximated by

$$\vec{E}_0(x) = \frac{G(x)}{a}\hat{e}_y \tag{2.75}$$

for the case of a cavity located on the x-axis, gap-voltage distribution $G(x)$ with upper bound $\hat{G}$, gap distance a and shunt impedance R, as defined in section 1.1.1. The expression for the magnetic field distribution follows immediately from Maxwell's equations (2.1)

$$\vec{B}(x) = j\frac{\dot{G}(x)}{\Omega a}\hat{e}_z \tag{2.76}$$

Lorentz forces induced by this rf-magnetic field induce an outward deflection for leading particles and inward deflection for trailing particles and therefore to compression of the bunches in the region where the gradient of the gap voltage is positive. Decompression occurs in the region where the gradient is negative. The normalization factor α for this mode can then be expressed by the unloaded quality factor Q_0 and resonance frequency Ω.

$$\alpha^2 \equiv \int E^2 dV = \frac{\hat{G}^2 Q_0}{\Omega R \varepsilon_0} \qquad\qquad Q_0 = \Omega\frac{\frac{\varepsilon_0}{2}\int E^2 dV}{\frac{\hat{G}^2}{2R}} \tag{2.77}$$

This defines the normalized mode $\vec{e}_0 = \frac{\vec{E}_0(\vec{x})}{\alpha}$ and the projection of the reduced excitation (2.9) introduced into (2.58) gives directly

$$\vec{F} = c^2\mu_0\vec{J} \qquad\qquad K_{10} = \sum_i 2c^2\mu_0 I_0 \left\{\frac{2v_i}{\Omega a}\sin\left(\frac{\Omega a}{2v_i}\right)\right\}\frac{G(x_i)}{\alpha}e^{-\frac{\Omega\sigma_i}{2v_i^2}} \tag{2.78}$$

with transit time correction represented in the curly brackets and bunch length correction in the exponent. The expression above leads directly to the amplitude coefficient $b_{01} \approx \frac{K_{10}}{\Omega r_0}$ in (2.53) in the case of a cavity tuned to $\lambda_0 = \Omega^2$. And therefore, in the limits of small transit times and short bunches gives

$$\vec{E} = \dot{a}_0(t)\vec{e}_0(\vec{x}) = -\frac{2c^2\mu_0 I_0}{r_0\alpha^2}\sum_i G(x_i)\vec{e}_0(\vec{x})\cos(\Omega t) \tag{2.79}$$

Corresponding to a beam induced gap voltage with upper bound after simplification with (2.77)

$$\hat{G}_B = 2I_0 R\sum_i \frac{G(r_i)}{\hat{G}} \tag{2.80}$$

2.3.1   Link to Equivalence Circuit

If the parameters in the partial differential equations of a parallel RCL-circuit (see fig. 2.2) excited by the current source I_B are compared with (2.40) of the damped mode

oscillation, the equivalent parameters can be identified immediately as

$$\lambda \equiv \Omega^2 = \frac{1}{LC} \qquad\qquad r \equiv \frac{\Omega}{Q_0} = \frac{1}{RC} \qquad\qquad F = \beta \frac{\dot{I}_B}{C} = \beta \frac{\Omega R \dot{I}_B}{Q_0} \qquad (2.81)$$

Where the scaling factor β for the condition that the cavity gap voltage equals the voltage of the lumped circuit is given by the definition

$$V_G(t) = V_R(t) = \dot{a}_0(t) \int \hat{e}_0(x) dx_B = \frac{\Omega}{\alpha} j a_0(t) \hat{G} = \frac{a_0(t)\hat{G}}{\beta} \qquad (2.82)$$

With the first oscillating Fourier coefficient of the reduced excitation according to (2.44) and (2.78) leading to the same result as (2.80)

$$F = K_{10} cos(\Omega t) = \sum_i 2c^2 \mu_0 I_0 \frac{G(r_i)}{\alpha} \cos(\Omega t) \qquad (2.83)$$

$$\hat{I}_B = 2I_0 \sum_i \frac{G(r_i)}{\hat{G}} \qquad (2.84)$$

2.3.2   Reduction of the Amplitude by Coupling to the Amplifier

The energy conservation law (2.33) illustrated already how the damping of a cavity increases by the external coupling by the coupling port. This is particularly interesting in the case of the fundamental mode, where good coupling to the amplifier is essential for the feeding of an accelerating cavity. Figure (2.2) illustrates the particular case of the fundamental mode with inductive coupling to the amplifier, cavity voltage and phase correction by the feedback loop and tuning for the resonance frequency adjustment. The rf-signal is fed from the oscillator and a pre-amplifier chain to the final-stage power tube amplifier (T). Afterwards, the amplified rf-signal passes through an output matching network of the amplifier consisting of a shorted $\lambda/4$ transmission line (TL_1 and TL_2). This is required for the impedance transformation from the high tetrode impedance to the low characteristic impedance of the transmission line TL_3 to the cavity. The power is coupled by loop L_1 to the fundamental mode of the cavity, represented as a lumped RCL-circuit. Loading of the system by the particle beam is considered by the current source I_B according to (2.84).

A useful parameter for the description of external loading of the cavity is the external quality factor Q_{ext}, defined by the ratio of total stored energy U in the cavity to the power P_{ext} transported out of the cavity [8] when the amplifier is switched off. According to (2.33).

$$\frac{1}{Q} = \frac{1}{Q_0} + \frac{1}{Q_{ext}} \qquad\qquad Q_{ext} = \frac{\omega U}{P_{ext}} \qquad (2.85)$$

The power transported out of the cavity into the coaxial line is given by surface integral of the Poynting vector (2.35) over the port cross section A with $\eta^2 = \mu_0/\varepsilon_0$, simplified for the case of a TEM-mode

$$P_{ext} = \int_A \langle S \rangle dA \qquad\qquad \langle S \rangle = \frac{|\vec{E}||\vec{H}|}{2} = \frac{1}{2\eta}|\vec{E}|^2 = \frac{\eta|\vec{H}|^2}{2} \qquad (2.86)$$
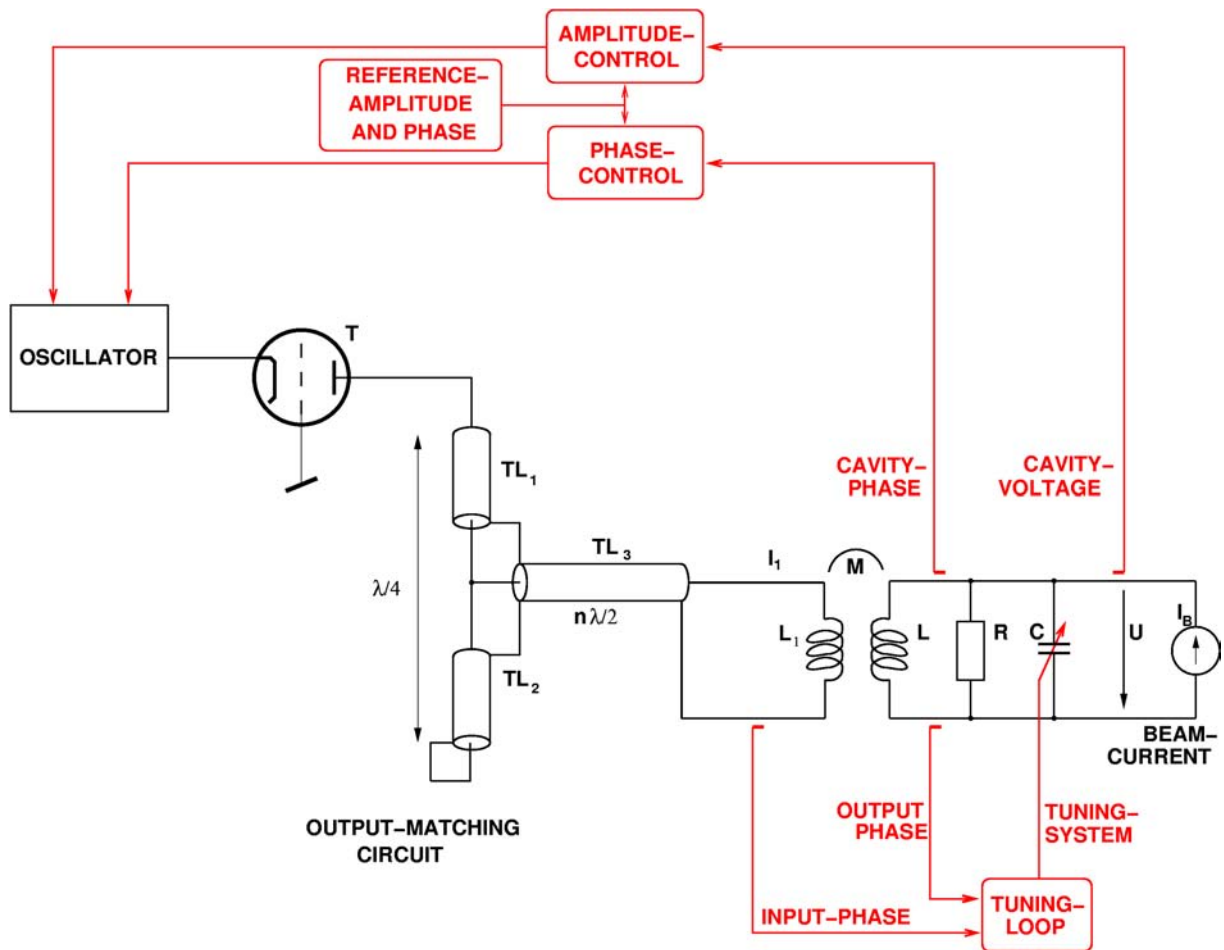
Figure 2.2: **Equivalence circuit of the fundamental mode with coupling to amplifier, amplitude- and phase-control system and tuning loop.** Control- and tuning systems are indicated in red. The amplifier is represented in grounded grid configuration.

With equation (2.85) the external quality factor can finally be rewritten as

$$Q_{ext} = \omega \eta \frac{\oint\limits_{\text{Cavity}} \varepsilon_0 |\vec{E}|^2 dV}{\int\limits_{A} |\vec{E}|^2 dA} = \frac{\omega \oint\limits_{\text{Cavity}} \mu_0 |\vec{H}|^2 dV}{\eta \int\limits_{A} |\vec{H}|^2 dA} \tag{2.87}$$

An additional complication occurs by the nonlinearity of the output impedance of the tube amplifier. Therefore Q_{ext} might depend on the output power of the amplifier.

2.3.3   Effects of Tuning, Amplitude- and Phase Control System

Deformation of the cavity shape shifts the resonance frequency of the cavity [68]. The mechanical tuning system compensates for deformations due to changes in atmospheric pressure and temperature gradients. This relatively slow system compares the phase of input wave with cavity phase and corrects the shape of the cavity until the right resonance frequency is found. As side effect, reactive beam loading is compensated by this method as well.

The amplitude- and phase feedback loops provide a fast correction for keeping the cavity voltage and phase constant. Beam quality requirements usually impose tight limits on these parameters. Amplitude- and phase feedback loops compensate beam loading effects and have to satisfy the stability criteria for all the required beam currents. The particular case of Robinson stability will be discussed in more detail in section 4.4.2.

2.4   Action of the Fields on the Particles

The action of the electromagnetic fields onto the particles is described by the Lorentz force equation (2.4) with electric and magnetic fields originating from the superposition of the following fields

Static magnetic field: provides the focusing of the particles onto their design orbit.

Cavity fundamental modes: are used for the acceleration of the particle bunches. Their magnetic rf-field yields a compression and decompression of the bunches. It is shown in *Adam* [1] that the accelerated reference trajectory keeps the same revolution time as the static reference trajectory. Gap crossing resonances might occur in particular cases [28].

Self field of particles: introduces nonlinear forces and reduce the focusing strength of the accelerator.

Electromagnetic fields excited by the beam: leads to additional energy spread and deteriorates the beam quality.

Space charge field of neighbor bunches: induces a coupling of the particle bunches if neighbors are close or overlap partially in the accelerator.

2.4.1 Decoupling of Horizontal and Vertical Motion

The equations of motion in the static magnetic field can be simplified considerably, if higher orders in the expansion of the magnetic field are negligible because of its particular configuration. Following the approach described in *Bruck* [17] for the case of a magnetic sector with constant gradient of the magnetic field $\vec{B}$ in cylindrical coordinates (r, θ, z)
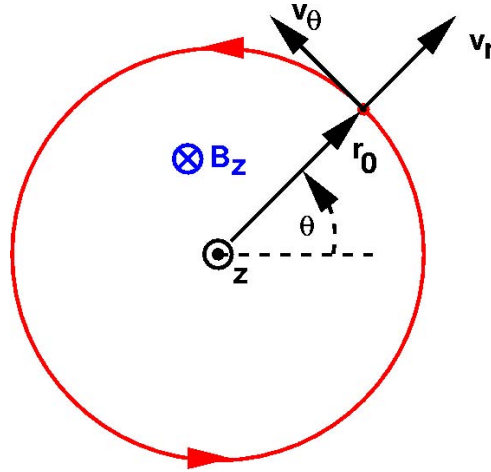
Figure 2.3: **Orientation of coordinate system, direction of particle propagation and static magnetic field (B_z).**

$$\vec{B}_\theta = 0 \qquad\qquad \frac{\partial}{\partial\theta}\vec{B} = 0 \qquad\qquad \vec{E} = 0 \qquad (2.88)$$

it can be shown that the equations of motion can be written for a particle with mass m and charge eq as

$$m\ddot{r} - mr\dot{\theta}^2 = qer \qquad\qquad mr^2\dot{\theta} + \frac{qe}{2\pi}\psi = \text{const.} \qquad (2.89)$$

$$m\ddot{z} = -qer\dot{\theta}B_r \qquad (2.90)$$

where the second equation corresponds to the *Busch's theorem* with enclosed magnetic flux ψ represented by the potential vector $\vec{A}$ by

$$\psi = 2\pi \int_r B_z r\, dr \qquad\qquad \frac{1}{2\pi r}\psi = |\vec{A}| \qquad (2.91)$$

Developing the magnetic field around the equilibrium orbit with radius r_0 leads to the series representation of the equations of motion with azimuthal velocity $v_\theta = r\dot{\theta}$ and

deviation $x = r - r_0$

$$n \equiv -\frac{r_0}{B_0} \frac{dB_z}{dz}\bigg|_{r=r_0} \tag{2.92}$$

$$m\ddot{r} = \frac{mv_\theta^2}{r} + qev_\theta B_0 \left(1 - n\frac{x}{r_0} + \dots\right) \tag{2.93}$$

$$mrv_\theta + qeB_\theta r_0 \left(\frac{x}{r_0} + \dots\right) = \text{const.} \tag{2.94}$$

$$m\ddot{z} = ev_\theta B_0 n\frac{z}{r_0}\left(1 + \dots\right) \tag{2.95}$$

The higher order terms in x/r_0 are symbolized by dots. A particular solution of this system of coupled differential equations is given by

$$x = r - r_0 = 0 \qquad z = 0 \qquad mv_\theta = \text{const.} = -qeB_0 r_0 \tag{2.96}$$

The evolution of $x(t)$ and $z(t)$ are now searched for trajectories close to the particular solution. With the approximations

$$v = v_\theta \sqrt{1 + \left(\frac{\dot{x}}{v_\theta}\right)^2 + \left(\frac{\dot{z}}{v_\theta}\right)^2} \approx v_\theta \qquad mv = p = p_0 + \Delta p \tag{2.97}$$

$$\frac{1}{mv} = \frac{1}{p_0}\left(1 - \frac{\Delta p}{p_0}\right) \qquad\qquad r = r_0 + x \tag{2.98}$$

$$\frac{1}{r} = \frac{1}{r_0}\left(1 - \frac{x}{r_0}\right) \qquad\qquad p_0 = -qeB_0 r_0 \tag{2.99}$$

The decoupled equations of motion are finally obtained as

$$x'' + \frac{1-n}{r_0^2}x = \frac{1}{r_0}\frac{\Delta p}{p} \qquad\qquad \Delta p = \text{const.} \tag{2.100}$$

$$z'' + \frac{n}{r_0^2}z = 0 \tag{2.101}$$

Here, the derivatives with respect to time are transformed into derivatives with respect to the length of the arc $s = vt$

$$x'' \equiv \frac{d^2 x}{ds^2} \qquad\qquad z'' \equiv \frac{d^2 z}{ds^2} \tag{2.102}$$

The solution of these simplified equations of motion (2.100 and 2.101) are harmonic oscillations called *betatron oscillations* of the form

$$x = \Delta x + a_1 \sin\left(\frac{s}{\lambda_x}\right) + a_2 \cos\left(\frac{s}{\lambda_x}\right) \qquad z = a_3 \sin\left(\frac{s}{\lambda_z}\right) + a_4 \cos\left(\frac{s}{\lambda_z}\right) \tag{2.103}$$

with

$$\Delta x = \frac{r_0}{(1-n)}\frac{\Delta p}{p} \qquad\qquad \lambda_x = \frac{r_0}{\sqrt{1-n}} \qquad\qquad \lambda_z = \frac{r_0}{\sqrt{n}} \tag{2.104}$$

leading to the focusing conditions $0 < n < 1$, betatron wavelengths $\lambda/(2\pi)$ and betatron wave numbers

$$\nu_x = \sqrt{1-n} \qquad\qquad \nu_z = \sqrt{n} \qquad (2.105)$$

In the more general case of a sector focusing cyclotron, the magnetic field can be approximated as [13]

$$B(r,\theta) = B_0(r)\left[1 + f(r)\cos\left(N\left\{\theta - \xi(r)\right\}\right)\right] \qquad (2.106)$$

The sector focusing concept is used to keep axial focusing in a relativistic cyclotron. Azimuthal variations of the static magnetic field produce a scalloping of the particle orbits, the instantaneous radius of the curvature increasing and decreasing as the particle moves from weak to strong field regions. The functions $B_0(r)$ and $f(r)$ are referred to as the average field and flutter, $\xi(r)$ is the spiral and N the sector number. The scalloped orbits have a radial component of velocity which oscillates with the same periodicity as the static magnetic field; the product $v_r B_\theta$ is therefore constant over the symmetry plane for example (since B_θ is also oscillatory with the periodicity of the field) and provides the axial focusing. Since the scalloping of the orbits and the strength of the B_θ field component are both directly proportional to f^2. If, in addition to the flutter, a spiral is introduced in the field, a further enhancement of the focusing results, due to introduction of alternating gradient focusing by the $v_\theta B_r$ term in the force.

Smooth approximation of the focusing effects with flutter and spiral leads to the corrected focusing frequencies ν_r and ν_z of the decoupled movements in vertical and horizontal direction:

$$\nu_z^2 = -k + \frac{-k}{2}f^2\left\{1 + 2\tan^2(\alpha)\right\} \qquad\qquad \nu_r^2 = 1 + k \qquad (2.107)$$

$$k(r) = \frac{r}{\bar{B}}\frac{\partial\bar{B}}{\partial r} \qquad\qquad \tan(\alpha) = r\frac{d\xi}{dr} \qquad (2.108)$$

with the relation to the radial oscillation frequency $\Omega_r = \Omega\nu_r$ and axial oscillation frequency $\Omega_z = \Omega\nu_z$ for angular velocity Ω of the particles [61].

More detailed theoretical investigations [65, 66] and comparison with simulation indicate that the particle motion in the horizontal plane can be split into a center motion and motion in small circles around it. The decoupling of vertical- and horizontal motion will be discussed further by numerical experiments in section 3.2.2. Numerical investigation of the decoupling can also be found in the design study for a cyclotron based driver for Accelerator Driven Systems (ADS) from *NSCL* [47].

2.4.2   Motion Equations in the Laboratory Frame

The center of charge (and mass) moves with velocity $\vec{u}$. An arbitrary particle of charge qe and rest mass m_0 in the bunch has some velocity $\vec{v}$. The energy equations can be used to eliminate the time derivatives of the γ factors from the momentum equations.

$$\frac{d\vec{p}}{dt} = \vec{F}_0^{\text{EX}} \qquad\qquad \vec{p} = m_0\gamma_u\vec{u} \qquad (2.109)$$

$$U_{\text{tot}} = m_0\gamma_u c^2 = U_{\text{kin}} + m_0 c^2 \qquad\qquad \frac{dU_{\text{kin}}}{dt} = \vec{u}\vec{F}_0^{\text{EX}} \qquad (2.110)$$

For the reference particle:

$$m_0 \gamma_u \frac{d\vec{u}}{dt} = \vec{F}_0^{\mathsf{EX}} - \frac{\vec{u}(\vec{u} \cdot \vec{F}_0^{\mathsf{EX}})}{c^2} \tag{2.111}$$

and the general particle:

$$m_0 \gamma_v \frac{d\vec{v}}{dt} = \vec{F}_2^{\mathsf{SC}} + \vec{F}_0^{\mathsf{EX}} - \frac{\vec{v}(\vec{v} \cdot \vec{F}_0^{\mathsf{EX}})}{c^2} \tag{2.112}$$

Where $\vec{F}_0^{\mathsf{EX}}$ is an externally applied force due to magnets and cavities and $\vec{F}_2^{\mathsf{SC}}$ is the correction for the space charge force with

$$\vec{F}_2^{\mathsf{SC}} = F^{\mathsf{SC}} - \frac{\vec{v}(\vec{v} \cdot \vec{F}^{\mathsf{SC}})}{c^2} \tag{2.113}$$

The space charge term can be expressed in terms of the Coulomb electric fields, due to the assembly of particles, as calculated in the frame co-moving with the center of mass of the group. Let the electric field be $\vec{E}_{\mathsf{SC}}'$ in a frame which is co-moving with $\vec{u}$. It is assumed that in this rest frame of the bunch there is an electric field $\vec{E}_{\mathsf{SC}}'$ but no magnetic field $\vec{B}_{\mathsf{SC}}'$. The electric field is resolved into components transverse and longitudinal to the reference motion.

$$\vec{E}' = \vec{E}_\perp' + \vec{E}_\parallel' \tag{2.114}$$

In the laboratory frame, the space charge force on a test particle is given by the Lorentz transformation [35]

$$\vec{F}^{\mathsf{SC}} = qe \left[\vec{E}_\parallel' + \gamma_u \vec{E}_\perp' + \frac{\gamma_u}{c^2} \vec{v} \times (\vec{u} \times \vec{E}_\perp') \right] \tag{2.115}$$

Substitution of $\vec{v} = \vec{v}_\parallel + \vec{v}_\perp = \vec{u} + \Delta\vec{v}$ leads to the exact expression

$$\frac{\vec{F}_2^{\mathsf{SC}}}{qe} = (\vec{E}_\parallel' + \gamma_u \vec{E}_\perp') \left(1 - \frac{uv_\parallel}{c^2} \right) - \frac{\Delta\vec{v}}{c^2} \left(v_\parallel E_\parallel' + v_\perp \gamma_u E_\perp' \right) \tag{2.116}$$

To the first order approximation of low energy spread we have $(1 - uv_\parallel/c^2) \approx 1/\gamma_u^2 \approx 1/\gamma_v^2$ and the final term in (2.116) in $\Delta\vec{v}/c^2$ is negligible. Therefore

$$\vec{F}_2^{\mathsf{SC}} = \frac{qe}{\gamma_u} \left[\vec{E}_\perp' + \frac{\vec{E}_\parallel'}{\gamma_u} \right] \tag{2.117}$$

If the charge to mass ratio qe/m_0 is now set to unity, the simplified acceleration can be written as

$$\frac{d}{dt} \gamma_u \vec{v} = \vec{F}_0^{\mathsf{EX}} + \frac{1}{\gamma_u} \left[\frac{\vec{E}_\parallel'}{\gamma_u} + \vec{E}_\perp' \right]^{\mathsf{SC}} \tag{2.118}$$

The forces acting on a particle can therefore be calculated in a simplified way by the superposition of external forces and Lorentz transformed space charge forces in a co-moving frame located at the center of charge.

2.5 Summary

The theoretical basis for the numerical study of beam-cavity interaction was developed in this chapter. For the first time, a general eigenmode expansion method with Fourier decomposition of the beam propagating is applied to the case of a cyclotron. Using the frequency domain approach, steady state conditions can be computed efficiently. If the beam-cavity interaction effects are small, the simplified frequency domain description provides the same results as the more self consistent time domain calculation, but avoids the very long time integration of the equations until steady state condition is reached. Application of the formulas, derived in the frequency domain, to the fundamental cavity modes, provides an expression for the beam loading effects with long bunch and transit time correction.

   Our analysis of the beam dynamics equations imply that decoupling of vertical and horizontal movement in the cyclotron leads to an accurate description of the particle motions if higher order terms are negligible. This will be required later for the space charge correction by the PICN method.

Chapter 3

NUMERICAL METHODS

This chapter presents a short overview of the numerical methods and is composed of two parts: eigenmode calculation and particle-tracking with space-charge correction.

Electromagnetic fields, used in the beam-cavity interaction simulation by mode-expansion technique, are no longer localized in discrete cavities, but spread around the entire cyclotron instead. Therefore field calculation methods are required being capable to compute efficiently eigenmodes of very large and complicated rf-structures. An additional complication is the tight clustering of eigenmodes at higher frequencies. This requires robust solvers with safe convergence to the desired eigenmodes.

The beam-excited mode-amplitudes and -phases depend on the positions and velocities of the particle bunches in the cyclotron. Trajectories of charged particles in the cyclotron are therefore calculated to determine these parameters. For the simulation of the effect of these beam-excited fields back onto the particle-distributions, a large number of macro-particles has to be propagated from cyclotron injection to extraction. Because of the space-charge dominated beam dynamics in the ring-cyclotron, a PICN (Particle In Cell Needle) solver is used for the calculation of these additional fields. For faster computation times, some critical routines are parallelized with OpenMP[6].

3.1 Short Description of the Eigenmode-Solvers

The solution of Maxwell's equations (2.1) and (2.3) in a cavity amounts, after separation of time/space variables and elimination of the magnetic field, to solving the eigenvalue problem

$$
\begin{aligned}
\nabla \times \nabla \times \vec{e}(\vec{x}) &= \lambda\, \vec{e}(\vec{x}), & \vec{x} \in \Omega, \\
\nabla \cdot \vec{e}(\vec{x}) &= 0, & \vec{x} \in \Omega, \\
\vec{n} \times \vec{e} &= 0, & \vec{x} \in \partial\Omega,
\end{aligned}
\tag{3.1}
$$

where $\lambda = \omega^2/c^2$ and $\vec{e}$ is the normalized electric field intensity. Using the weak formulation proposed by *Kikuchi* [26], it is equivalent to

Find $(\lambda, \vec{e}, p) \in \mathbb{R} \times H_0(\mathrm{curl}; \Omega) \times H_0^1(\Omega)$ *such that* $\vec{e} \neq \vec{0}$ *and*
(a) $(\nabla \times \vec{e}, \nabla \times \vec{\Psi}) + (\nabla p, \vec{\Psi}) = \lambda(\vec{e}, \vec{\Psi})$ $\forall \vec{\Psi} \in H_0(\mathrm{curl}; \Omega)$ (3.2)
(b) $(\vec{e}, \nabla q) = 0,$ $\forall q \in H_0^1(\Omega)$

where p is a Lagrange multiplier.

The field $\vec{e}$ in Eq. (3.2) can be discretized by tetrahedral edge elements proposed by Nédélec [26] and the Lagrange multiplier p by node elements. This yields a large sparse constrained matrix eigenvalue problem of the form

$$\boldsymbol{A}\mathbf{x} = \lambda \boldsymbol{M}\mathbf{x} \qquad \boldsymbol{C}^T\mathbf{x} = \mathbf{0}. \tag{3.3}$$

where A is symmetric positive semi-definite and M is symmetric positive definite. $\boldsymbol{A}$ is sometimes referred as *stiffness matrix* and $\boldsymbol{M}$ as *mass matrix*. The matrix $\boldsymbol{C}$ results from the discretization of the divergence equation and has full rank. The number of columns of $\boldsymbol{C}$, i.e. the number of constraints, is about one eighth of the order of $\boldsymbol{A}$ and $\boldsymbol{M}$. However, with this particular mixed finite element discretization the eigenvalues of Eq. (3.3) are equal [26] to the *positive* eigenvalues of

$$\boldsymbol{A}\mathbf{x} = \lambda \boldsymbol{M}\mathbf{x}. \tag{3.4}$$

Nédélec edge elements allow the normal components of the underlying numerical solution to be discontinuous across inter-element boundaries, and hence model the boundary conditions and material interfaces naturally. Additionally, electric fields $\vec{e}$ modeled by the Nédélec edge elements automatically satisfy the divergence-free equation in the weak sense [76]. The linear Nédélec element has 6 degrees of freedom (DOF), the quadratic Nédélec element has 20 DOF. The number of degrees of freedom is reduced if the element is located on the boundary. Finite element basis functions are local functions associated only with the finite element to which they are assigned. Thus, the resulting matrices are very sparse: there are only about 20 nonzero entries per row for linear elements and about 60 for quadratic elements. For the same finite element mesh, the solution for quadratic elements (with curved surfaces) converges closer to the analytical solution than linear elements. However, matrices from linear elements are smaller, sparser and more diagonally dominant and therefore have better computational properties.

The equation (3.4) can be solved by different algorithms [7]. Depending on the size of the problem and the location of the eigenvalues direct solvers or iterative solvers are preferably used. Preconditioners speed up the convergence of a solver. These methods are implemented in the programs *Omega3P* and *PyFemax*.

3.1.1   Omega3P

Omega3P has been developed in the Advanced Computations Department (ACD) of the Stanford Linear Accelerator Center (SLAC). It can use parallelized Inexact Shift-and-Invert Lanczos algorithm (ISIL) or Exact Shift-and-Invert Lanczos algorithm (ESIL) with the choices of iterative linear solvers or sparse direct solvers [43, 45]. Outer eigenvalues of large systems are preferably calculated with ISIL and iterative solvers, like preconditioned Conjugate Gradient (*CG*), because of memory-limitations. Tightly clustered inner eigenvalues, on the other hand, lead to convergence problems in iterative solvers and direct solvers are therefore used with the ESIL algorithm. Direct solvers require large computer memories and a Massively Parallel IBM-SP4 of the Swiss National Supercomputing Centre (CSCS) therefore was used for this type of computation.

The geometry of the rf-structure is generated and meshed in the CUBIT [21] program. This mesh and the input-file with all the solver parameters is then read by Omega3P. The output files containing the computed eigenmodes can finally be combined to one file for field-visualization in the MeshTV [49] program.

The collaboration with ACD resulted in adapting Omega3P for simulations of beam-cavity interaction in cyclotrons and to couple with beam dynamics routines [74]. Its wall-loss computation has recently been improved to allow different wall material in the same geometry. This is important for the simulation of separate-sector cyclotrons because the wall material of accelerating cavities are usually different from the wall material of the vacuum chamber.

For incorporating the rf-fields into beam-dynamics routines, it is necessary to export the electric- and magnetic field distribution in the region of the horizontal beam-plane, as well as the field energy and power loss. A small program has been developed to perform the linear interpolation of the rf-fields from the nodes of the elements to a structured cylindrical grid in the beam-plane and to write the data to a file in vtk-format (see section 3.2.1). The vtk format has the advantage that it can directly be visualized in MayaVi [58] for verification.

3.1.2 PyFemax

The Python Finite Element Maxwell solver was developed by R. Geus [26] at the Institute of Computational Science (ICoS) at ETH Zürich. It is currently extended to the parallel FemaXX-code in the frame of the SEP-CSE project *Large Scale Eigenvalue Problems in Opto-Electronic Semiconductor Laser and Accelerator Cavities* in a collaboration between ICoS and the Institute of Integrated Systems of ETH-Zurich, PSI and the Institute of Informatics of University Basel.

The eigenvalue problem (3.3) is solved numerically using an implementation of the Jacobi-Davidson (JD) algorithm, optimized for the symmetric eigenvalue problem [26]. To improve the speed of the eigensolver, a set of preconditioners was implemented: the *Jacobi* and *SSOR* preconditioners, the *ILUS incomplete factorization preconditioner*, a *two-level hierarchical basis preconditioner* based on an algebraic multigrid method.

The two-level hierarchical basis preconditioner exploits the hierarchical organization of the finite-element basis functions and is a 2×2-block Gauss-Seidel method for which the second order diagonal block is only solved approximately. For the first-order diagonal block an iterative method is used, accelerated by an algebraic multigrid preconditioner. For small problems, a direct method like SuperLU can be used instead. The advantage of the two-level hierarchical basis preconditioner is that the number of iterations is almost independent of the problem size and makes this method attractive for very large problems.

ANSYS, CUBIT or NetGen [52] can be used for the construction of the geometry and mesh. The calculated eigenmode-fields are exported in the vtk-format for visualization in MayaVi [58]. PyFemax does not yet include *curved* finite elements. This is a disadvantage for the simulation of curved rf-structures. Although the program was already successfully used for the simulation of tens of eigenmodes of large structures, it is also not yet possible to compute tightly coupled Higher Order Modes with PyFemax,

because of the poor convergence in this case. The program is currently extended for field-export to the *MAD9P* beam-dynamics program [4].

3.1.3   Example: Eigenmodes of the COMET-Cyclotron

Omega3P and PyFemax have been used [75, 27] for a cross-check of the eigenmode calculation of the COMET cyclotron rf-structure to be delivered by ACCEL GmbH for the PSI PROSCAN project for proton-therapy (see Fig. 3.1). This structure consists of two galvanically and two capacitively coupled double gap cavities (see Fig. 3.2). The coupling leads to push-pull and push-push modes with a resonant frequency separation of less than 1 MHz [1]. The insertion of the tube for the ion-source and the insertion of the "puller" on the Dee at injection affect the coupling of the cavities.

The unstructured mesh enables a good approximation of the complex geometry. An accurate simulation of the electromagnetic fields and the coupling of the Dees is a challenging aspect of this structure. About 1.2 million tetrahedrons are used leading to a problem size of about 10 million degrees of freedom. The simulation required 12 GBytes of memory and the sequential PyFemax-code used 31 hours of CPU-time on the HP Superdome at ETHZ for the calculation of the first five eigenmodes.

Meshing and Symmetrization of the Modes

The resonance-frequency of the COMET-cyclotron is tuned by adjusting the stem length of the Dees. However, a field-asymmetry occurs between voltages in different Dees if all the stems are adjusted to the same length. For the cyclotron operation, it is required that the protons get about the same "kick" in each gap. The length of the stems has therefore to be adjusted for each Dee to yield identical gap-voltage. This also had to be done in the simulation to provide realistic results.

It is difficult to generate a suitable mesh, because of the exorbitant amount of fine details in the geometry from the CAD-file received from ACCEL. One run of mesh-generation with CUBIT typically took about one night, although only the upper part of the structure is simulated taking a magnetic surface as symmetry condition. In order to reduce the computational effort, the mesh was generated just once and the stem length adjusted subsequently by small linear deformation in vertical direction of those nodes which are located in the stem. The stem length is then adjusted until the required field balance of the magnetic field in the stems is reached.

Eigenmode Calculation

The cyclotron will be operated at the eigenmode with the lowest resonance frequency in push-pull mode. In order to get an idea about the mode separation and power

---

[1]Previous simulations by *Stephani* [71, 72] of ACCEL and *Stingelin* [22], using a simplified model, showed a larger mode separation of 2 MHz. However, the more detailed simulation, as presented in the following sections, yields a separation of about 500kHz between the push-pull and push-push mode. This result is also confirmed by measurement (see table 3.1).
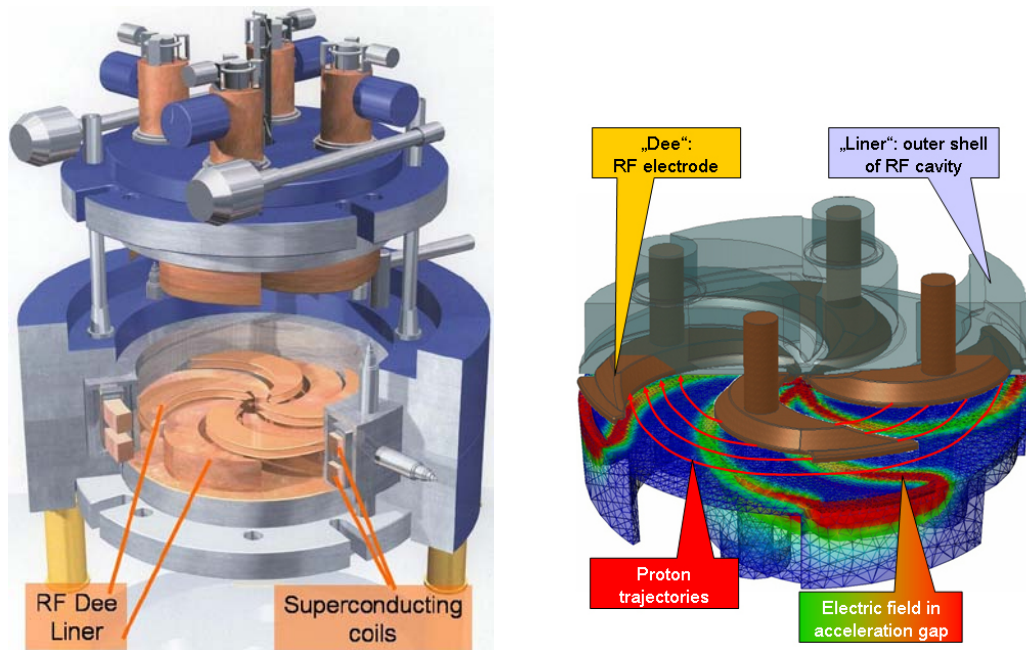
Figure 3.1: **Picture of the COMET-cyclotron (left) and electric-field distribution (right).** The diameter of the rf-structure is about 1.8m.
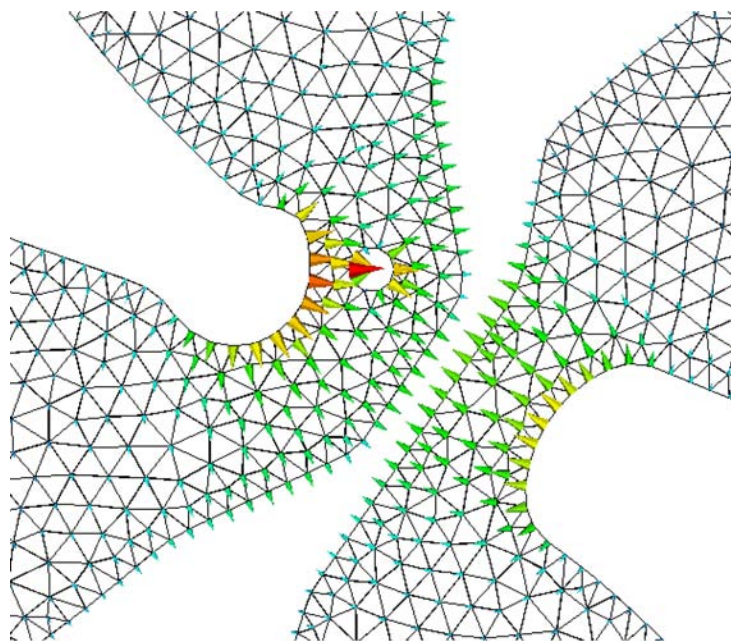
Figure 3.2: **Mesh and electric field of the fundamental mode in the beam plane in the central region of the COMET structure.** The "chimney" of the ion source (circle in the center) as well as the capacitive coupling and the galvanic coupling of the Dees are shown.
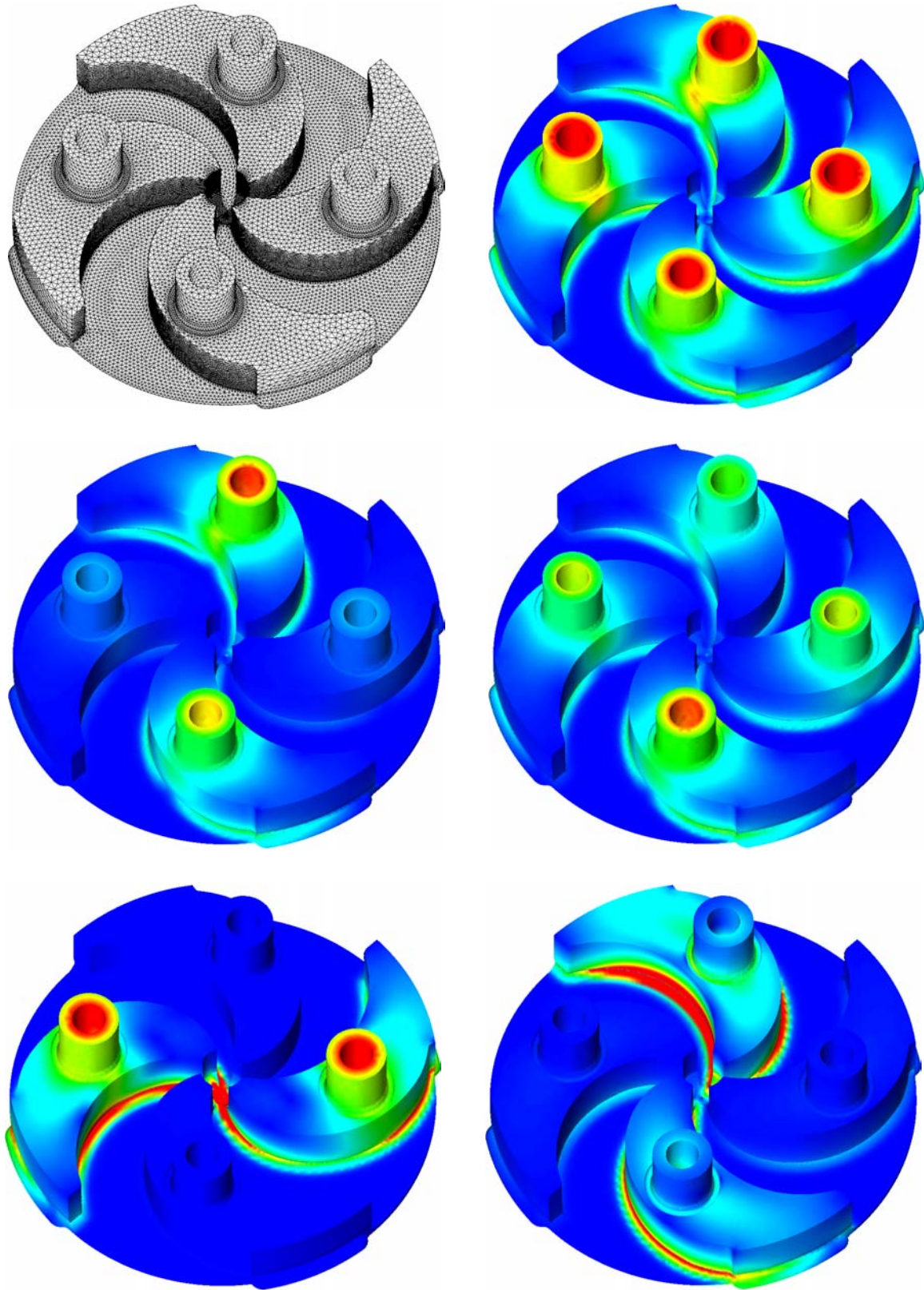
Figure 3.3: **Mesh (top-left) and magnetic field distribution for the 5 lowest modes.** The modes are ordered from left to right and top to bottom with increasing resonance frequency.

Figure 3.4: **Top view on vector plot of magnetic field distribution for the 4 lowest modes.** Push-pull and push-push modes can be identified on the top left and bottom left respectively. The modes are ordered from left to right and top to bottom with increasing resonance frequency.

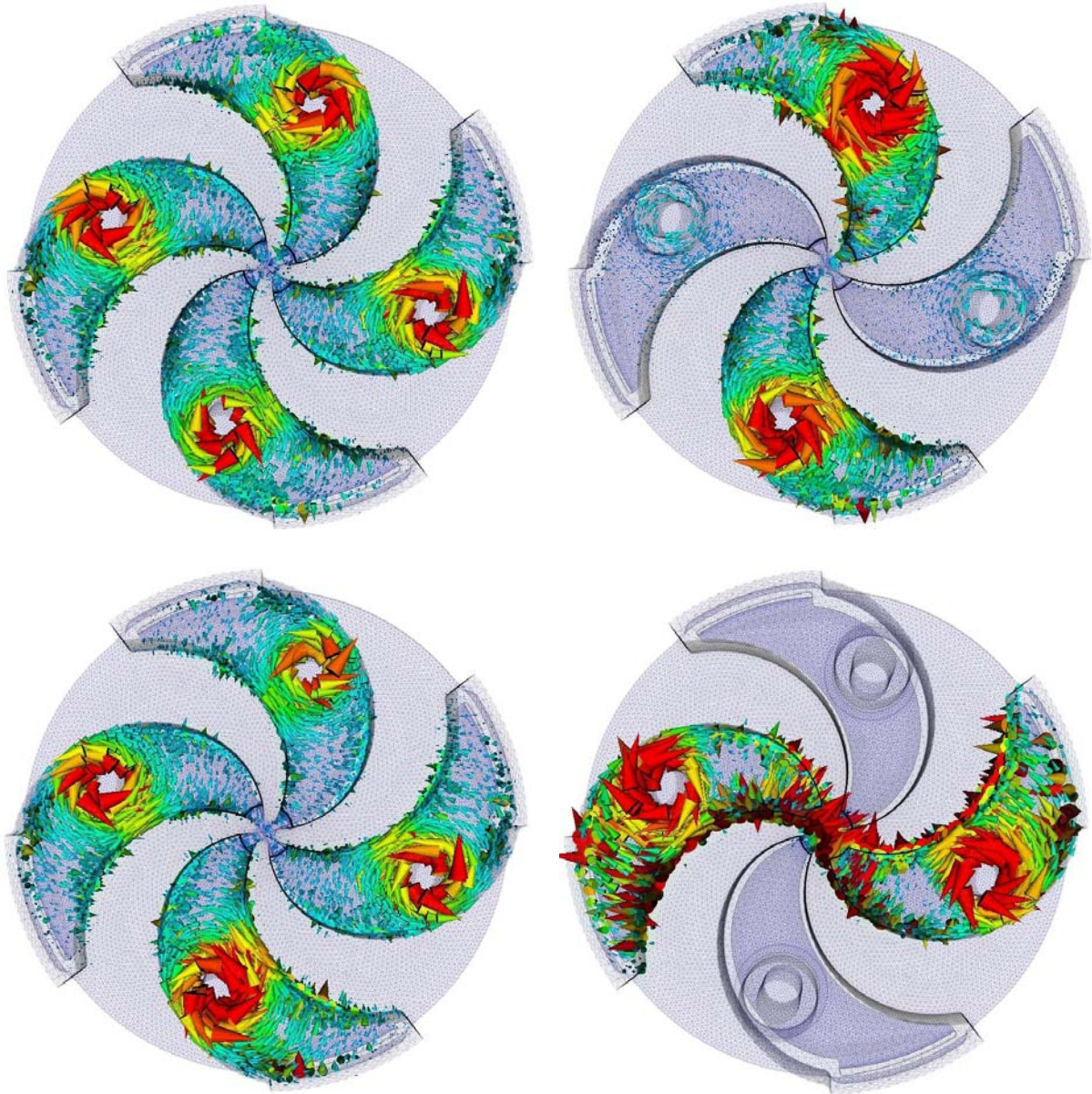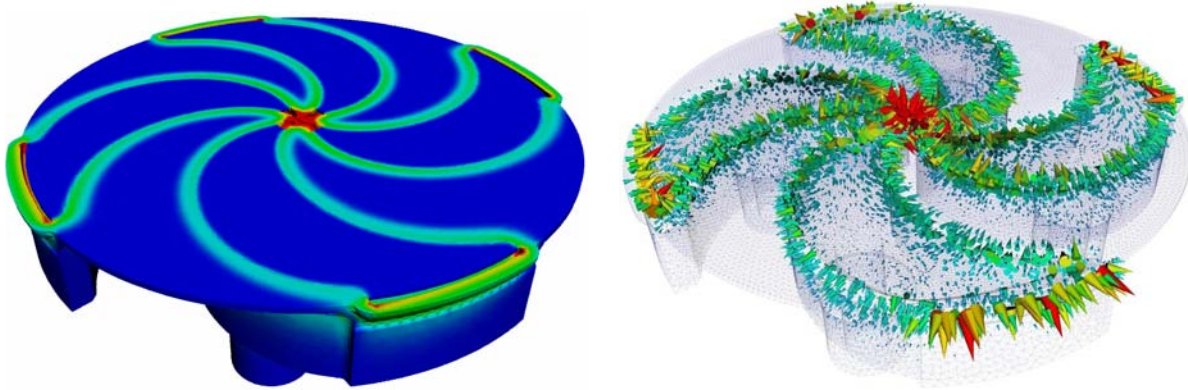Figure 3.5: **View on the beam plane of the COMET rf-structure.** The contour- and arrow-plot of the electric field is shown for the operating mode.

requirement, resonance frequencies and unloaded quality factors of the first five modes are calculated. They are indicated in table 3.1 and illustrated in figure 3.3 and 3.4.

Figure 3.5 shows the absolute value of the electric field in the cyclotron for the operating mode. The phase of the electric field shifts by an angle π during the time required for one proton-bunch to propagate from one gap to the next one. Maximum field values are found in the central region and at the outermost radii of the Dee. On the other hand, the gap-voltage is minimal close to the stem. Figure 3.2 illustrates the electric field distribution in the central region. The mesh represents the central region in a realistic manner.

The cyclotron operation requires an injection voltage of about 80kV from ion-source to the puller in the first Dee crossing. This yields the scaling-factor for the calculation of the power requirement.

3.1.4   Comparison with Measurement

The resonance frequencies and quality factors are measured with a network-analyzer by ACCEL. Transmission curves from coupling loop to the inductive pick-ups, located in each stem, are analyzed and the resonance peaks identified.

For comparison with measurement, the lowest mode is tuned to the simulated resonance frequency and the stem lengths are adjusted until a symmetrized field balance is reached. The good match of measured and calculated resonance frequencies of the higher modes shows that the coupling in the central region is modeled quite accurately by this simulation method. The difference between simulated and measured quality factors can be explained by the additional power loss occurring in rf-fingers and brazed/welded interfaces.

Mode Number	Mode Type	Calculated		Measured	
		Frequency [MHz]	Q_0	Frequency [MHz]	Q_0
1	↑↓↑↓	73.178	7500	73.183	5'953
2	↑↓↓↓	73.439	7600	73.413	NA
3	↑↑↑↑	73.691	7600	73.640	5'932
4	− ↑ − ↓	92.456	7100	92.710	NA
5	(↑ − ↓ −)	131.663	9800	132.837	NA

Table 3.1: **Measured and calculated resonance-frequencies with Omega3P and PyFemax.** The mode-type ↑ stands for *push*, ↓ for *pull* phase of the oscillation in the corresponding Dee, the - indicates that the field-values in the corresponding Dee are small. The last mode has a different oscillation mode in the Dee.

3.1.5 External Quality Factor from Eigenmode Calculation

In addition to wall-losses, eigenmodes can also be damped by coupling to rf-input or output ports, like transmission-lines or waveguides. This can be described by the external quality-factor Q_{ext}, as illustrated in section 2.3.2. The equations (2.87) developed there are derived from a traveling wave model. If the location of the port cross section A is chosen appropriately, these equations remain valid also for the standing wave model [8]. The standing wave field can be considered as a superposition of two traveling wave fields, where one has an inversed time. Therefore, one can apply formulas (2.87) with the resulting fields of eigenmode calculations with different boundary conditions at the port A.

The Q_{ext} can be calculated [9] as sum of Q_E and Q_M from eigenmode calculations with perfectly magnetic-, respectively electric conducting boundary condition at the port location.

$$Q_E = \frac{\omega \oint_{\text{Cavity}} \varepsilon_0 |\vec{E}_E|^2 dV}{c \int_A |\vec{E}_E|^2 dA} = \frac{|1 + e^{j\varphi}|^2}{4} Q_{ext} \tag{3.5}$$

$$Q_M = \frac{\omega \oint_{\text{Cavity}} \varepsilon_0 |\vec{H}_M|^2 dV}{c \int_A |\vec{H}_M|^2 dA} = \frac{|1 - e^{j\varphi}|^2}{4} Q_{ext} \tag{3.6}$$

Leading to the final equation with vanishing phase φ

$$Q_{ext} = Q_E + Q_M \tag{3.7}$$

This method has the advantage, that the external quality factor can be calculated in two consecutive eigenmode runs with the same mesh, but different boundary conditions at the port.

The loaded quality factor can be determined experimentally by bandwidth measurements or damping-time measurement of the mode. It can also be extracted from the closed loop measurements of the transfer function. The loaded quality factor can then be determined from the parameters of the low-pass function of the closed loop transfer function. This is an elegant way to measure loaded external quality factors even in operation at high-power levels, if the external loading depends on the output-power of an amplifier, for example.

3.2 Particle-Tracking

The algorithms used for the tracking of protons in the ring-cyclotron are based on routines of the *TFIX* and *PICN* Fortran77 programs, developed by the PSI beam-dynamics group [41]. They were adapted for the purpose of this work and rewritten in C, C++ [50]. In particular, the space charge correction method in PICN with smoothly approximated particle focusing is extended for particles moving in the measured magnetic fields. The method for the calculation of single-particle orbits corresponds basically to the method used in TFIX. It is extended for trim coil correction of the magnetic fields and additional rf-fields originating from beam-excited modes. rf specific features are implemented, like amplitude- and phase modulation of the gap-voltages and phase monitors. Time critical routines are parallelized with OpenMP [6] for shared memory computers. The rf-fields of precedent eigenmodes can be read from a file and used in the orbit-calculation. Amplitudes and phases of the beam-excited modes are then calculated directly from the simulated beam trajectories.

3.2.1 The Particle-Pusher

The particle-pusher is based on a Runge-Kutta integrator of the relativistic equation of motion in the Lorentz-force field. Different methods are used for the interpolation of the fields onto the particles:

- **Interpolation of the Static Magnetic Field:** For the accurate calculation of the proton trajectories, a higher order representation of the measured field is required. The vertical field component B_z in the beam-plane and its derivatives $\partial B_z/\partial\theta$, $\partial^2 B_z/\partial\theta^2$ and $\partial^3 B_z/\partial\theta^3$, in the cylindrical coordinate system (r, θ, z), are read from file and the other derivatives are constructed by a 5-point Lagrange differentiation in r and θ direction. If the components of the static static magnetic field are symmetric around the (r,θ)-plane, the vertical field components can be

developed [11] by

$$-B_r = z\frac{\partial B_z}{\partial r} - z^3 F_3 \tag{3.8}$$

$$-rB_\theta = z\frac{\partial B_z}{\partial \theta} - z^3 G_3 \tag{3.9}$$

$$F_3 = \frac{1}{6}\left(\frac{\partial^3 B_z}{\partial r^3} + \frac{\partial^2 B_z}{r\partial r^2} - \frac{\partial B_z}{r^2\partial r} + \frac{\partial^3 B_z}{r^2\partial r\partial\theta^2} - \frac{2\partial^2 B_z}{r^3\partial\theta^2}\right) \tag{3.10}$$

$$G_3 = \frac{1}{6}\left(\frac{\partial^3 B_z}{\partial r^2\partial\theta} + \frac{\partial^2 B_z}{r\partial r\partial\theta} + \frac{\partial^3 B_z}{r^2\theta^3}\right) \tag{3.11}$$

The values for B_z, B_r and B_θ are then interpolated from the 4 closest grid-points by a third-order Taylor expansion and transformed to the Cartesian coordinate system. For the case of the ring cyclotron, the magnetic fields have a periodicity of $\pi/4$ in azimuthal direction. The corresponding grid-size for one sector is then 141×136 in radial, and azimuthal direction respectively in the *s03av.nar* file.

- **Interpolation of the RF-Fields:** The electric- and magnetic field of each higher-order mode has to be interpolated to the particle position. Typically about 30 critical eigenmodes are considered for the mode-expansion technique. In order to reduce the computational effort, only a first-order Taylor-expansion is used for the interpolation of the rf-fields. This is not critical, as a relatively fine grid is chosen.

  A structured cylindrical grid, typically of size $250 \times 720 \times 3$ in radial, azimuthal and vertical direction respectively, is used for the representation of the rf-fields in the region of the beam plane. Previous to the particle simulation, the fields of a set of eigenmodes from the Omega3P calculation are linearly interpolated onto this grid and written to a vtk-file. This file contains all necessary mode parameters like power loss, resonance frequency and quality-factor, the grid information and the electric and magnetic field vectors in Cartesian coordinates.

- **Runge-Kutta Integration:** The particles are pushed in the 6-dimensional position-momentum space by a 4th order Runge Kutta algorithm for large arrays, using a minimum of workspace [33]. This algorithm has been modified by *S.Adam* as illustrated in table 3.2 for faster execution times.

Original	Modified
z0 = x(n)	z0 = x(n)
p0 = DT * fct(z0)	p0 = DT/2 * fct(z0) + 0.0*p0
z1 = z0 + p0/2	z1 = z0 + p0
q1 = p0	omit! exchange the roles of p and q
p1 = DT * fct(z1)	q1 = DT/2 * fct(z1) + 0.0*q0
z2 = z1 + p1/2 - q1/2	z2 = z1 + q1 - p0
q2 = q1/6	p2 = p0/3
p2 = DT * fct(z2) - p1/2	q2 = DT * fct(z2) - 1.0*q1
z3 = z2 + p2	z3 = z2 + q2
q3 = q2 - p2	p3 = p2 - q2
p3 = DT * fct(z3) + 2*p2	q3 = DT/2 * fct(z3) + 1.0*q2
x(n=1) = z4 = z3 + q3 + p3/6	x(n=1) = z4 = z3 + p3 + q3/3

Table 3.2: **Runge-Kutta algorithm for large arrays.** DT corresponds to the time-step and fct(z) to the function to be integrated to yield x(n).

As the maximum time step is also limited by the maximum frequency of the rf-fields, the time step is kept constant. A typical time step is about 0.1ns, whereas the simulated HOM with the highest resonance frequency has a period time of about 1.4ns. For a test of the integrator, a particle-trajectory was simulated from injection to extraction. The subsequent back-integration of this particle from extraction to injection with time-inversion showed errors smaller than $70\mu m$ and $200eV$ for small time-steps.

3.2.2   A Note on the Decoupling of Vertical- and Horizontal Motion

A numerical experiment was performed to check the validity of the hypothesis that the horizontal and vertical particle-motions are decoupled (see 2.4.1). A macro-particle $\mathfrak{a}$ was started at injection with an offset of $2.5mm$ from the macro-particle $\mathfrak{b}$ in the beam-plane. On its trajectory from injection to extraction, $\mathfrak{a}$ propagates with a standard deviation of $1.6mm$ in vertical and $0.1mm$ in horizontal direction around $\mathfrak{b}$. The ratio of horizontal to vertical standard-deviation decreases for smaller vertical offset values. This shows that the coupling of vertical to horizontal movement is relatively small, at least for this order of magnitude of vertical oscillation.

3.2.3   Space Charge Effects in the PICN-Model

For the space charge correction, it is assumed that the vertical and horizontal motions are decoupled, so that the internal space charge forces can be calculated by a particle in cell method applied to the median plane charge distribution. This is called the Particle In Cell Needle model (PICN).

The beam is represented by an ensemble of uniformly charged vertical rods [41] of the same height and the artificial force laws can then be derived from the potential functions of one rod:
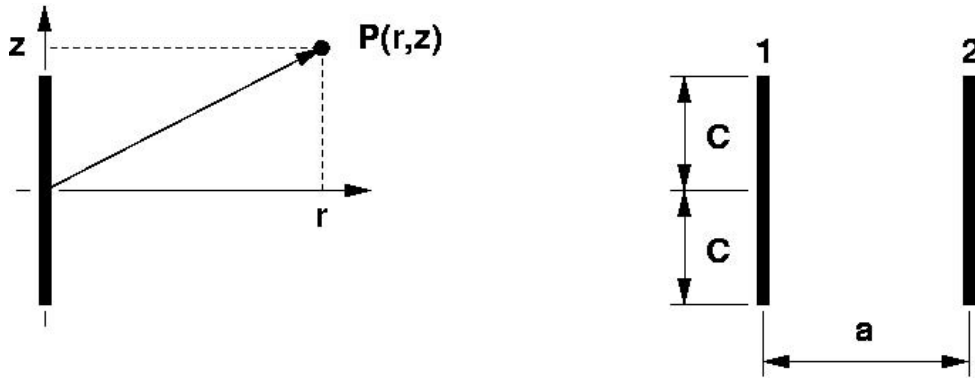

Figure 3.6: **Parameters of the vertical rods used for the PICN model.** Cylindrical coordinates are used for the integration of the potential function

The potential at a radial distance r and axial position z of rod 1 of length $2C$, uniformly charged with density $q_1/2C$ can be calculated by the integral

$$\Phi(r, z) = \frac{q_1}{8\pi\varepsilon_0 C} \int_{-C}^{C} \frac{dz'}{\sqrt{r^2 + (z - z')^2}} \tag{3.12}$$

leading to an expression with rotational elliptical equipotential surfaces with focus at $\pm C$ [30]

$$\Phi(r, z) = \frac{q_1}{8\pi\varepsilon_0 C} \ln\left(\frac{\sqrt{r^2 + (z - C)^2} - (z - C)}{\sqrt{r^2 + (z + C)^2} - (z + C)}\right) \tag{3.13}$$

The reduced two dimensional potential Φ_2 acting onto the rod centers in the beam plane can be calculated by exchanging the order of integration and derivation in the definition of the electrostatic force:

$$F_r = \frac{q_1 q_2}{2C} \int_{-C}^{C} E_r dz = -\frac{q_2}{2C} \int_{-C}^{C} \frac{\partial \Phi}{\partial r}(r = a, z')dz' = -q_2 q_2 \frac{\partial}{\partial r}\Phi_2(r) \tag{3.14}$$

with

$$\Phi_2(r) = \frac{1}{4\pi\varepsilon_0 (2C)^2} \int_{-C}^{C} \Phi(r = a, z')dz' \tag{3.15}$$

The solution of this integral is straight forward with splitting of the logarithm substitution of the $(z - C)$, $(z + C)$ and the remaining argument function of the logarithm. Finally

$$\Phi_2(a) = \frac{1}{2\pi\varepsilon_0 (2C)^2} \left\{ a - \sqrt{a^2 + (2C)^2} + 2C \ln\left(\frac{\sqrt{a^2 + (2C)^2} + 2C}{a}\right) \right\} \tag{3.16}$$

and the corresponding normalized electric field $\vec{E}_0(r)$ for a unit charge can be calculated by derivation of this reduced potential

$$\vec{E}_0(r) = -\frac{\partial}{\partial r}\Phi_2(r) = \frac{\sqrt{r^2 + (2C)^2} - r}{2\pi\varepsilon_0 r(2C)^2}\hat{e}_r \qquad (3.17)$$

The convolution with the charge distribution leads then to the total electric field distribution.

$$\vec{E}(\vec{x}_\alpha) = -\sum_\beta q(\vec{x}_\beta)\vec{E}_0(|\vec{x}_\beta - \vec{x}_\alpha|) = -(q * \vec{E}_0) \qquad (3.18)$$

The convolution theorem enables to rewrite the force calculation in a form better suited for numerical calculation [57].

$$\vec{F}^{SC}(\vec{x}_\alpha) = -q(\vec{x}_\alpha)\mathfrak{F}^{-1}\left(\mathfrak{F}(q)\mathfrak{F}(\vec{E}_0)\right) \qquad (3.19)$$

The charges of the rods are therefore interpolated linearly onto a structured, two dimensional grid, centered at the center of mass of the bunch and transported parallel to its trajectory. A two-dimensional, parallel FFT-algorithm [24] is then used for the calculation of this convolution. Typical sizes of the equidistant grid are about 128×128 and one space charge force computation is performed per ten tracking steps.

3.2.4   A Note on Mode Expansion and Lorentz Transformation

Equation (2.21) indicates that the electric field vector has to be corrected for the space charge field by $\nabla\Phi$. On the other hand, there is no additional term in the corresponding equation for the magnetic field vector.

As known from the relativistic transformation of the electric fields from charges in a moving frame, there usually appears a retarded potential [35] and an additional magnetic field term in the Lorentz transformation. This term reduces the space charge forces in the reference frame.

The missing correction term in the expression for the magnetic field in (2.21) can be explained by the magnetic field of the beam-excited modes. If the basis for the mode expansion is complete, this magnetic field should be represented identically [42]. However, in the case of the ring cyclotron, the mode expansion was limited to modes with a resonance frequency of less than $700MHz$. Therefore, space charge fields are still transformed in a relativistic way to compensate the missing high frequency terms. With this approach it is also easier to compare the particle evolution with consideration of space charge forces, with and without beam excited HOMs.

3.2.5   Relativistic Coordinate System Mappings

Since the Poisson-equation is solved in a co-moving frame, the space-charge fields are transformed to the fixed cyclotron frame onto the particles. The coordinate system located at the center of mass of the proton bunch is propagated along the trajectory of the bunch. The transformation operation, from one bunch position to the next one,

consists of translations in straight sections, rotations in the sector magnets and acceleration in the cavities (see figure 3.7). Therefore, a general Frenet-Serret coordinate system [38] or transport of a Fermi-Walker tetrad [51] would be required for an exact description of the relativistic mapping.

However, only a simplified mapping is chosen in the program. It is supposed that the trajectory consists of small translations from the previous particle position to the position after one time step. The electromagnetic field tensor is transformed relativistically by Lorentz transformation [35] for a moving coordinate system with velocity v according to (2.115).
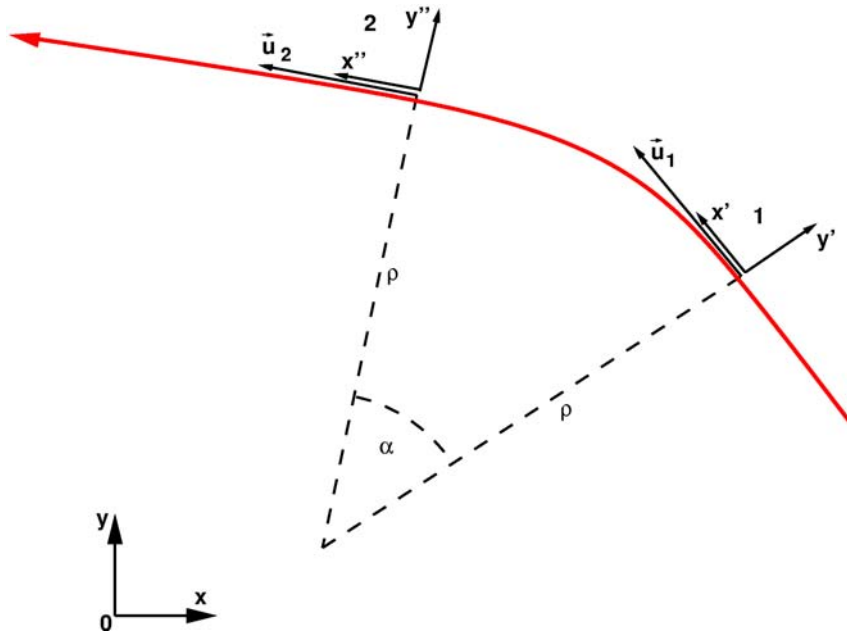

Figure 3.7: **Evolution of the reference coordinate system.** The transition from point 1 to point 2 is obtained by a translation with acceleration and rotation operation. Moving frames $x'y'$ and $x''y''$ are transformed relativistically to the lab frame xy.

3.2.6 Comparison with Analytical Space Charge Formula

An analytical estimation of the evolution of the transverse beam parameters under space charge influence can be found using the *Kapchinskij Vladimirskij* (KV) distribution [19]. The net forces F^{SC} on a particle of charge q at position (x, y) in a bunch of transverse radii a and b in the longitudinal particle density λ is equal to the electric force divided by γ^2:

$$\vec{F}^{SC}(x, y) = \frac{4q^2 e^2 \lambda}{\gamma^2} \left[\frac{x}{a(a+b)} \hat{x} + \frac{y}{b(a+b)} \hat{y} \right] \tag{3.20}$$

This yields the *envelope equations* for horizontal and vertical emittances ϵ_x and ϵ_y

$$a'' + K_x a - \frac{\epsilon_x^2}{a^3} = \frac{\xi}{a+b} \tag{3.21}$$

$$b'' + K_x b - \frac{\epsilon_y^2}{b^3} = \frac{\xi}{a+b} \tag{3.22}$$

where a prime means taking the derivative with respect to the path-length s, $K_{x,y}(s)$ specifies the external focusing and

$$\xi = \frac{4q^2 e^2 \lambda}{m\gamma^2} \tag{3.23}$$

is a dimensionless space charge parameter in function of proton mass m, charge qe and a maximum of uniform longitudinal particle density λ.
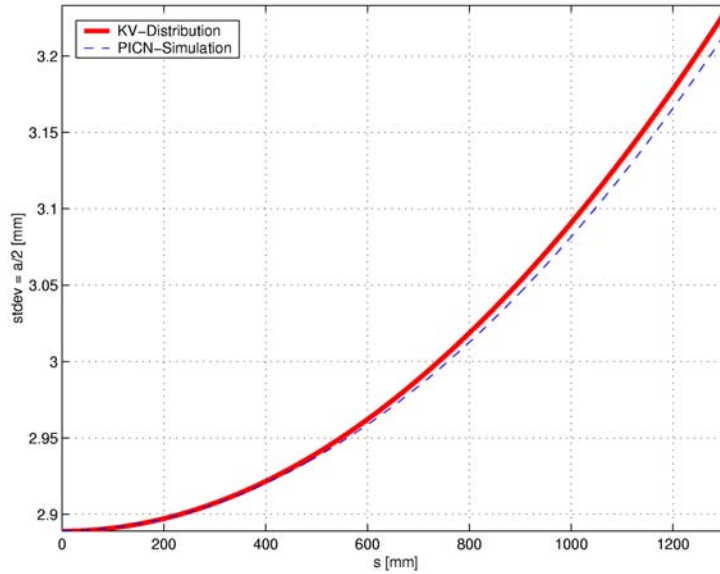

Figure 3.8: **Comparison of PICN-model with the analytical KV model.** Evolution of the transversal radius of a space charge dominated beam over 1.3m.

Figure 3.8 shows the evolution of the transversal radius of two beams with the same standard-deviations as initial conditions. There is a small difference in calculated transversal radii observed. From (3.17) of the PICN-model, it is obvious that the space charge field depends on the height C of the rods and that realistic values of C must be chosen therefore.

3.2.7   Particle Initialization and Stabilization

The initial conditions for the particles are chosen according to the stabilized starting-ensembles [41] from the radial focusing parameters for the first turn $\nu_1 \equiv \nu_r(1)$ because

of a lack of information on realistic space charge distributions at injection of the ring cyclotron.

The overall density of points is composed of a set of elementary disks. Each disk consists of concentric rings of short vertical rods. The disk centres are distributed homogeneously over a rectangular grid. Each macro-particle may carry a different charge.

It is shown in [41] that the equation of motion in an azimuthally varying field cyclotron can be written in the smooth-focusing approximation as

$$\rho'' - \rho(\theta')^2 + \nu_1\rho\theta' = F_\rho^{SC}, \qquad -2\rho'\theta' - \rho\theta'' + \nu_1\rho' = -F_\theta^{SC} \qquad (3.24)$$

in the local polar coordinate system (ρ, θ) attached to the center of mass. The superfix prime denotes the derivative with respect to turns and F^{SC} the space charge forces. The equilibrium circular solution is found by setting $\theta', \rho \equiv constants$. This leads directly to the equation for the angular velocity by

$$2\theta'(\rho) = \nu_1 + \sqrt{\nu_1^2 - 4\frac{F_\rho^{SC}}{\rho}}. \qquad (3.25)$$

The stabilized elementary disk is then found as follows

1. Generate a uniformly populated disk

2. Numerically solve for the space charge forces F_ρ^{SC} and F_θ^{SC}

3. Ring-by-ring evaluate $\theta'(\rho)$

4. Generate the correlated velocities according to $r' = \theta's$ and $s' = -\theta'r$ for $s = \rho\cos\theta$ and $r = \rho\sin\theta$.

These elementary disks are then copied to yield the overall charge distribution at injection location.

3.2.8 Parallel Performance

Some critical parts of the particle integrator, for the propagation of one bunch with space charge correction and in the beam excited rf-field, are parallelized using *OpenMP* pragmas [6] (compiler directives) for shared memory computers. These compiler directives are typically added before time critical loops so that the compiler can parallelize the loop accordingly. Fortunately there was already a parallelized Fourier-Transform available in the $FFTW$-package [24] and basically only the particle integrator routines had to be improved for parallel performance.

The best performance was reached by directly subdividing of the Runge-Kutta loop into several loops, so that each part runs on a separate processor, and to distribute the particles homogeneously this way. This minimizes the overhead required for the generation of the parallel-processes (*threads*).

n	#Threads Tracking	#Threads FFT	$T_n[s]$	T_1/nT_n
1	1	1	1203	1
16	16	8	81	0.93
32	32	4	84	0.45
32	32	8	52	0.73

Table 3.3: **Parallel Performance of OpenMP version of PICN for the first turn.** The execution time T_n for each run with n threads is shown and the parallel efficiency T_1/nT_n.

An example for the parallel-efficiency is shown in table 3.3 for the *Stardust* computer of ETHZ. The number of threads can be chosen separately for the tracking and FFT routines. As shown in the table, the shortest execution-time of $52s$ is reached with an efficiency of 73% when 32 threads are selected for the tracking routines and 8 threads for the FFT routines.

Faster execution times are currently achieved on the *Pegasus* computer of ETHZ. However, because of heavy loading it is difficult to get proper benchmarking results.

3.3   Summary

The numerical methods and the required approximations for the simulation of beam-cavity interactions are presented. An illustration of the eigensolver on the example of the COMET-cyclotron shows the first-ever eigenmode simulation of an entire cyclotron rf-structure. Good agreement between the PICN and analytical KV-model is shown for the horizontal beam plane, but requires the knowledge of the horizontal beam width and assumes a decoupling between horizontal and vertical motion. A numerical experiment is performed to test the validity of this hypothesis.

Chapter 4

RESULTS

Detailed measurements were carried out in beam development periods dedicated to beam-cavity interaction studies. The beam current was adjusted to a desired value and the corresponding mode amplitudes were measured by means of a cavity pickup.

During the shut down period of 2003, one of the main cavities had to be removed from the ring cyclotron. Therefore, it was possible to perform higher order mode measurements with open and closed beam slots. Large damping of the higher order modes due to radiation out of the beam slots and out of the pumping port suggested that the entire cyclotron structure has to be simulated for an accurate description of the electromagnetic fields in the cyclotron.

The commercial MAFIA-solver[1] [46] gave insight into the different methods for beam-cavity interaction simulations. It was found that simplified wake-field calculations (section 4.2.2) and investigations of the effects of beam excited fields onto the particles (section 4.2.1) are possible. On the other hand MAFIA's structured grid is a drawback for the accurate simulation of Higher Order Modes (HOMs). Particle in Cell (PIC) results for the cavity-crossing of a slow bunch (lower stiffness) with superposed HOMs indicate relatively small deformations of the bunch. Investigation of time-domain methods showed that their long solution times and noise problems are prohibitive for the direct solution of beam-cavity interactions in the entire cyclotron. This motivated the frequency domain approach with the mode-expansion technique.

Within the framework of the collaboration with the Advanced Computations Department (ACD) of the Stanford Linear Accelerator Center (SLAC), it was possible to take advantage of their eigenmode-solver *Omega3P* [43]. This code uses an unstructured tetrahedral grid for the representation of the rf-structure and achieves very short solution times by efficient parallel computing. The good convergence of Omega3P's ESIL solver enables one to find even the tightly clustered modes of the whole cyclotron. An exact mapping of the calculated HOMs onto measured spectra is difficult, because they partially overlap and because their resonance frequency depends on the operating condition.

Given the positions and the velocities of a bunch on a centered orbit, the amplitudes

---

[1]MAFIA is an acronym for "solution of **MA**xwells equations using a **F**inite **I**ntegration **A**lgorithm"

of the excited HOMs can be calculated. The interaction strength with an individual HOM can be described by a generalized "gap"-voltage. By tracking a bunch trough the cyclotron, the influence of the beam generated HOMs can now be determined.

4.1   Measurement of the Beam-Excited Modes

4.1.1   Excitation of the 11th Harmonic by the Beam

A spectrum analyzer was connected to the inductive pick up loops *1* and *d* of the main cavities of the ring cyclotron. It was then possible to record the dependence of the mode amplitudes in function of the chosen DC-value of the beam current as summarized in tab. 4.1. The most pronounced peak of the pick up signal is found in cavity 2 at a frequency of about 557MHz, corresponding to eleven times the particle crossing frequency of 50.6MHz and denoted as *11th harmonic frequency* in the following sections.
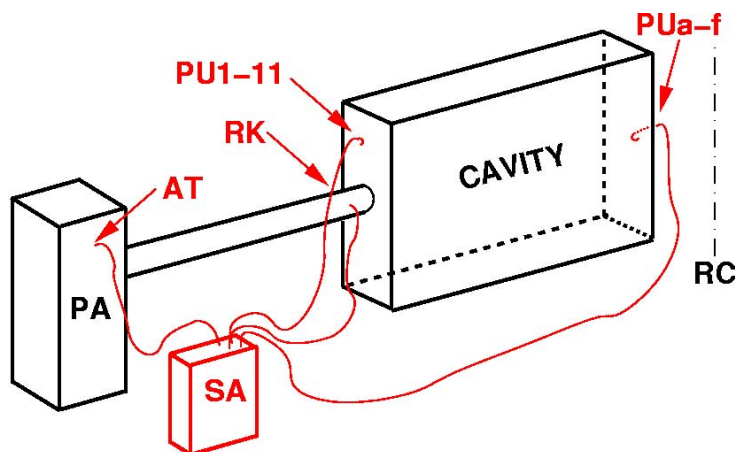

Figure 4.3: **Illustration of measurement setup.** The power-amplifier (PA) with anode-tank pick up (AT) is connected to the cavity. In the transmission line there is a directional coupler (RK) for the measurement of forward, and reflected power. The two inductive pick up loops (PU1) and (PUd) are mounted on the small side of the cavity. RC symbolizes the center axis of the ring cyclotron and SA the spectrum analyzer.

Figure 4.1 shows the dependence of the mode amplitude of this HOM with increasing beam current. The linear dependence suggests that no beam resonance, or beam instability is excited, at least at this current levels.

However, the measured pick up signal could also be related to a higher order mode oscillation at the same frequency in the anode-tank of the final-stage amplifier. Therefore, the spectrum-analyzer was connected to the pick up of the anode-tank for verification. A very small amplitude of an oscillation-signal with the same frequency is found, also increasing with beam-current as illustrated in figure 4.2.
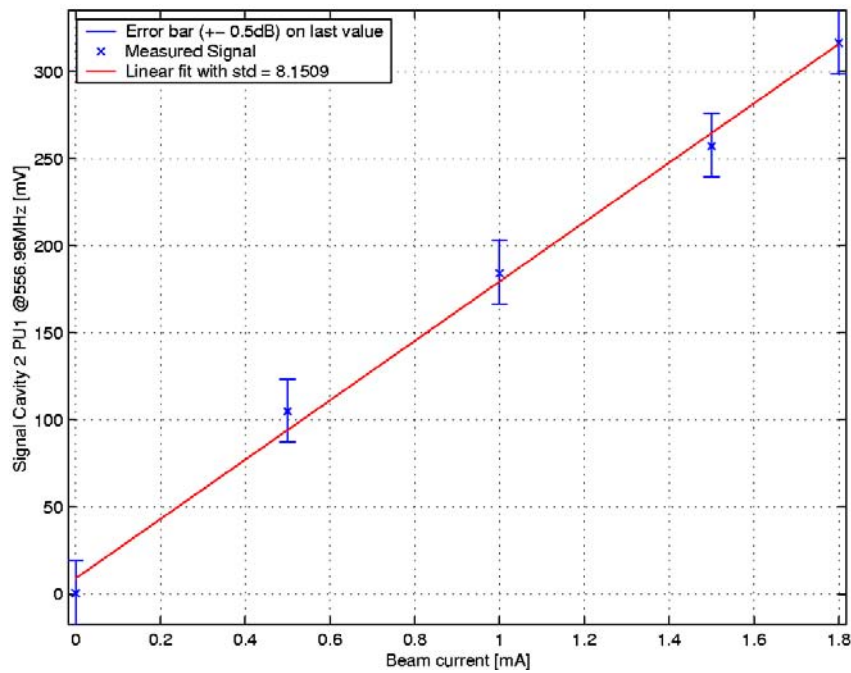
Figure 4.1: **Pick-up signal in function of the cyclotron proton beam.** The cavity pick-up signal increases almost linearly with beam current. Pick-ups on other cavities show the same dependence, but with different slope.
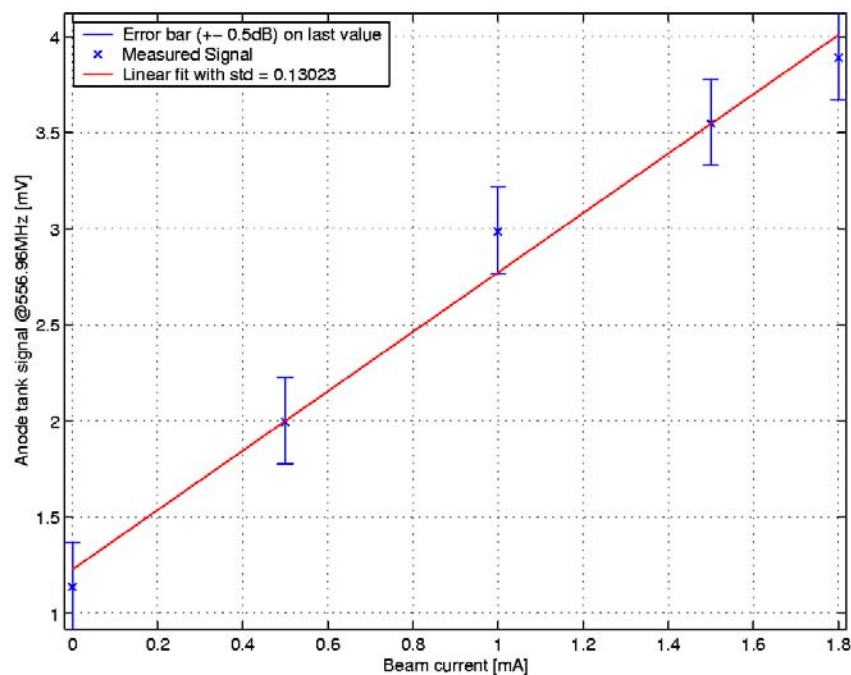

Figure 4.2: **Anode tank signal of the 800kW tube amplifier, feeding cavity 2.** The signal also increases almost linearly with beam current, but with an offset of 1.2mV at 0mA beam current.

Measurements with Spectrum Analyzer					
Cavity	Beam Current [mA]	Frequency [MHz]	Signal		
			PU 1 [dBm]	PU d [dBm]	RK 2 HL [dBm]
1	0	50.6328	30.8	29	23.2
2			31.0	28.7	21.3
3			31.2	28.7	21.3
4			31.7	28.8	22.3
1	0	556.961	-63.8	-87.2	
2			-61	-85.2	
3			-71	-85.8	
4			-71	-77.5	
1	0.5	556.961	-45.2	-58.2	
2			-9.6	-23.0	
3			-34.8	-62.5	
4			-48.0	-52.2	
1	1.0	556.961	-19.9	-33.0	
2			-4.7	-18.0	
3			-30.0	-57.8	
4			-42.6	-47.5	
1	1.5	556.961	-17.6	-30.3	
2			-1.8	-15.2	
3			-27.7	-54.5	
4			-39.6	-45.0	
1	1.95	556.961	-16.0	-29.2	-47
2			0.0	-13.3	-26.9
3			-26.3	-53.3	-31.8
4			-38.6	-43.8	-40.6

Table 4.1: **Effect of beam current on cavity mode excitation for all main cavities.** PU=Cavity Pick up, RK=Directional coupler on the transmission line, HL=Forward direction. PU 1 and PU d are inductive cavity pick ups, each located on one of opposite small sides of the cavity. Signals on directional coupler are measured only at maximum and zero beam current.

The cavity voltage is kept constant by the amplitude control system and the input power for the fundamental mode therefore depends linearly on the beam current. Compared with the cavity pick up signal at the same frequency, the amplifier signal has an offset at zero beam current. Even without beam current, there is a harmonic mode in the anode tank. It is created by the C-class operation mode of the amplifier and is supposed to increase nonlinearly with the power drive. In the cavity, on the other hand, the pick up signal is very small at zero beam current. The measured, almost linear dependence suggests, that the additional signal originated from the higher order mode in the cavity, is excited by the beam. This HOM couples to the coaxial line and therefore also to the anode tank of the amplifier.

4.1.2 Mode-Spectrum around the 11th Harmonic

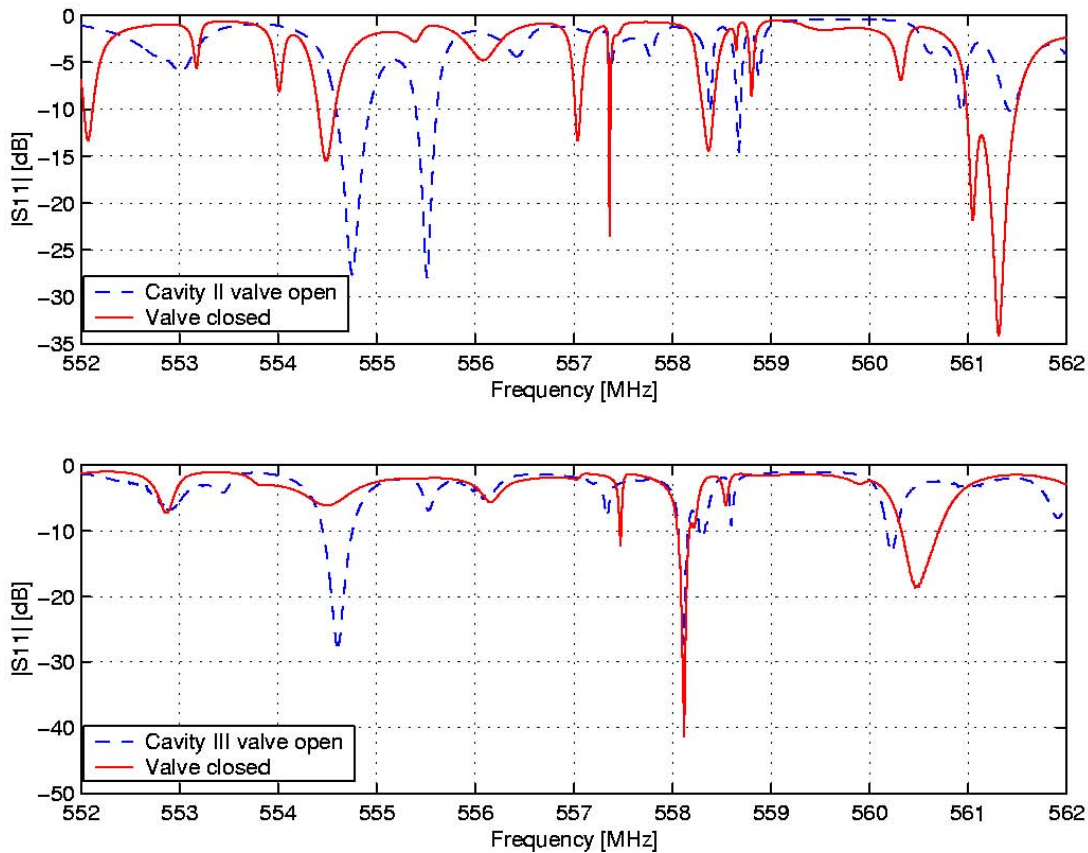Figure 4.4: **Mode spectrum of cavity 2 and 3 in the ring cyclotron.** The spectrum of higher order modes changes when the valve to the cryogenic vacuum pump is closed.

Figure 4.4 shows the measured mode spectra of two ring cyclotron main cavities, measured with a network analyzer across the cone adapter, connected to the coupling loop. The fundamental modes of the cavities were tuned by the hydraulic system to

be close to the operating frequency of 50.6328MHz and the ring cyclotron vacuum pressure was about 10^{-6}mbar.

It was observed that spectra of the higher order modes change significantly when the valve to the cryogenic vacuum pump is closed. The spectra are also different for each cavity. Estimate of the unloaded quality factors Q_0 with the *QZERO*-Program [39] indicated that the 557.036MHz mode in cavity 2 with closed valve had an unloaded quality factor of about Q_0=6'600 compared to the 557.392MHz mode of cavity 3 with Q_0=10'800.

The important rf radiation to the vacuum pump and through the beam slots into the cyclotron complicates the field simulation.

Measurement on one Main Cavity, removed from the Cyclotron

Cavity 3 was then taken out of the cyclotron and analyzed in the test bunker. Its beam slots were closed by triangular copper strips and the vacuum port was closed by an aluminum disk. A 20W amplifier was added between the output of the network analyzer and pick up *11* for improvement of the gain to get well measurable signals on pick up *d*. The vented cavity with closed beam slots and vacuum pump port shows twenty resonances in the range from 553MHz to 562MHz, as illustrated in table 4.2.

553.2	553.8	553.9	555.1	555.5	555.8	555.9	556.3	556.5	556.8
557.0	557.9	558.1	558.5	558.7	559.1	560.3	560.9	560.9	561.8

Table 4.2: **Measured modes in the range from 553 to 562 MHz.** Frequencies are indicated in MHz.

The coupling to the coaxial line of the modes with a resonance frequency close to 556.952MHz (11th harmonic) was investigated by quality factor measurements for the cases of open-, short- and 50Ω terminations at the adaptation cone, connected to the coupling loop (Tab. 4.3).

Resonance frequency [MHz]	Quality factor[-] coupling loop termination:		
	Short	50Ω	Open
556.43	23'991	15'318	26'003
556.93	18'077	13'483	22'029
557.85	51'781	6'838	60'301

Table 4.3: **Coupling of higher order modes to the coaxial line**

The output port of the network analyzer was connected to pick-up *1* of the cavity and the transmission was then measured to pick-up *a*. Quality factors are calculated from bandwidth measurements and decrease significantly with a resistive load on the coupling loop, indicating a strong coupling to the coaxial line according to equation (2.85).

4.2 Preliminary Simulations with MAFIA

4.2.1 Bunch Deformation by a HOM

A refinement of the analytical model (see appendix A) can be achieved by simulations with the program MAFIA. For a simulation of the effect of a similar mode to the measured one, onto the beam quality, a first analysis was performed in a combined eigenmode- Particle In Cell (PIC) simulation.

Eigenmodes in a closed cavity can be calculated with the MAFIA E3 eigenmode solver [46, 73]. The beam slots and the opening for the vacuum pump were neglected and represented as perfectly conducting boundaries. No coupling loop was modeled in this simulation. The E3 *Select-Solver* finds a mode at 554MHz with magnetic boundary as symmetry condition in the beam plane. This mode amplitude of the electric field was then rescaled to 10% of the fundamental mode and imported into the MAFIA TS3 Particle In Cell (PIC) solver. A slow bunch (with low stiffness) of 20pC, with velocity of a tenth of speed of light and negligible energy spread was then propagated selfconsistently across the cavity. The effect of the higher order mode onto the phase space of the particle bunch is summarized in figure 4.6. A visible oscillation can be observed in the momentum coordinates of the bunch.

Unfortunately, this model does not provide much information about what might happen in the cyclotron because of the missing focusing forces from the static magnetic field.

4.2.2 Wake Field Simulation

This time domain analysis was performed with MAFIA's three-dimensional Cartesian time domain solvers. The import of the particle positions and velocities from the beam dynamics calculations[2], interpolated onto the grid of MAFIA's solver, gives a realistic excitation model. Each of the 221 bunches acts in the T3 module as a one-dimensional, rigid current distribution which excites an electromagnetic field in the cavity. It is required that the z-axis of the simulation grid is oriented in direction of the particle velocity vector. The simulation in the T3 module has the advantage of being much faster than a fully self-consistent PIC calculation and uses much less memory.

A first idea about the effect of wake fields was gained by calculations of the field excited by the $i = 1 \ldots 221$ driving bunches with charge $q_i = q = 60pC$ crossing the cavity at the calculated positions, and integrating the Lorentz forces seen by a test particle with small charge e_i at distance s_i from the driving bunch q_i. The wake potential for *one* bunch q_i is then found by:

$$\vec{W}_i(s) = \frac{1}{q_i} \int\limits_{-\infty}^{\infty} \vec{E}(t = \frac{z+s}{v_i}) + \vec{v}_i \times \vec{B}(t = \frac{z+s}{v_i}) dz \qquad (4.1)$$

The longitudinal component of the wake potential describes the total voltage at the test particle divided by the charge of the wake field generating charge q. The transversal

---

[2]See section 3.2 for a description of the method.

Figure 4.5: **Phase space before cavity crossing.** For the momentum in longitudinal direction is only the relative value indicated. The empty space under the curve in the $\gamma\beta_y - z$ space appears as numerical artifact due to the magnetic boundary condition in the beam plane.
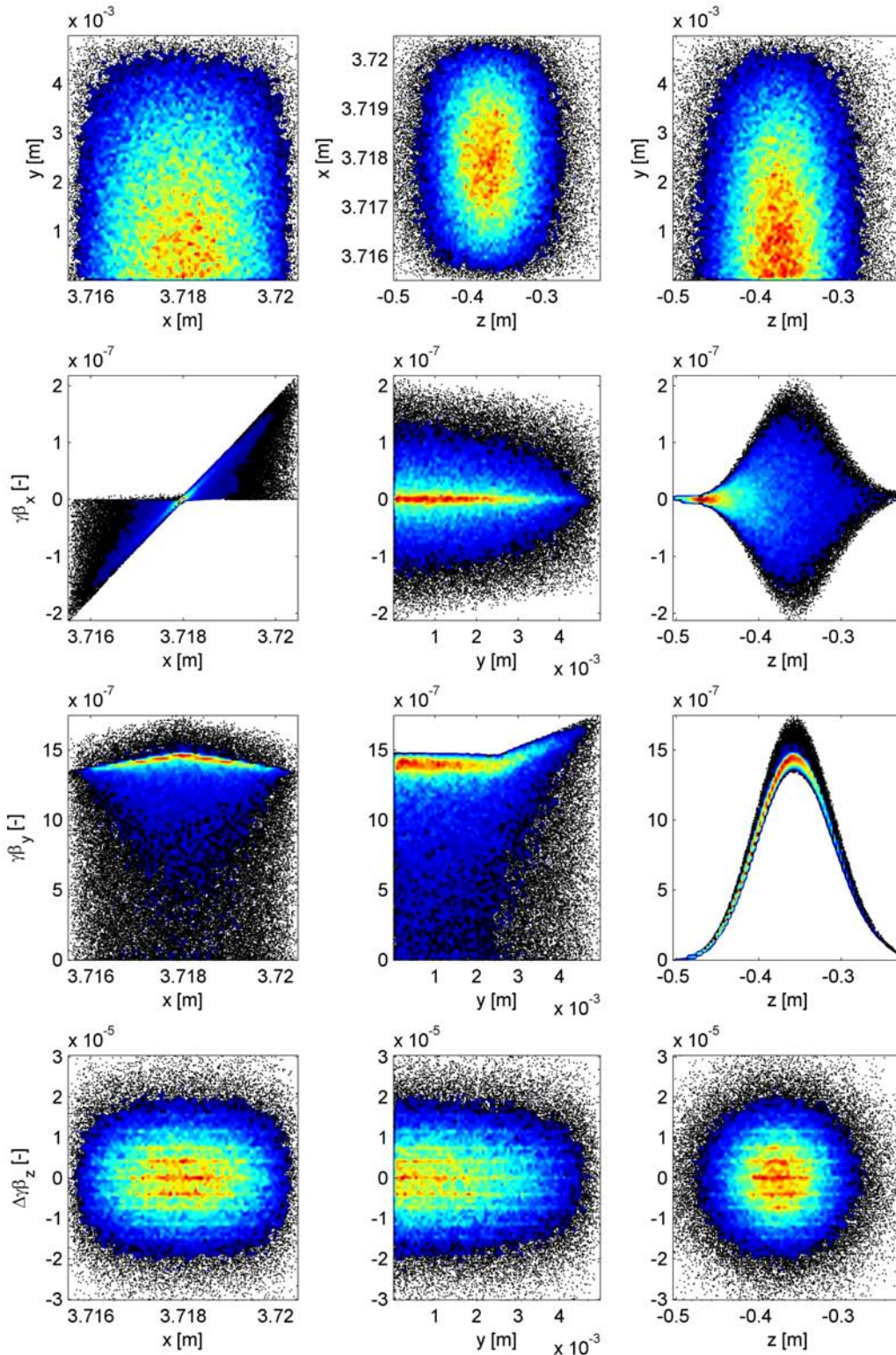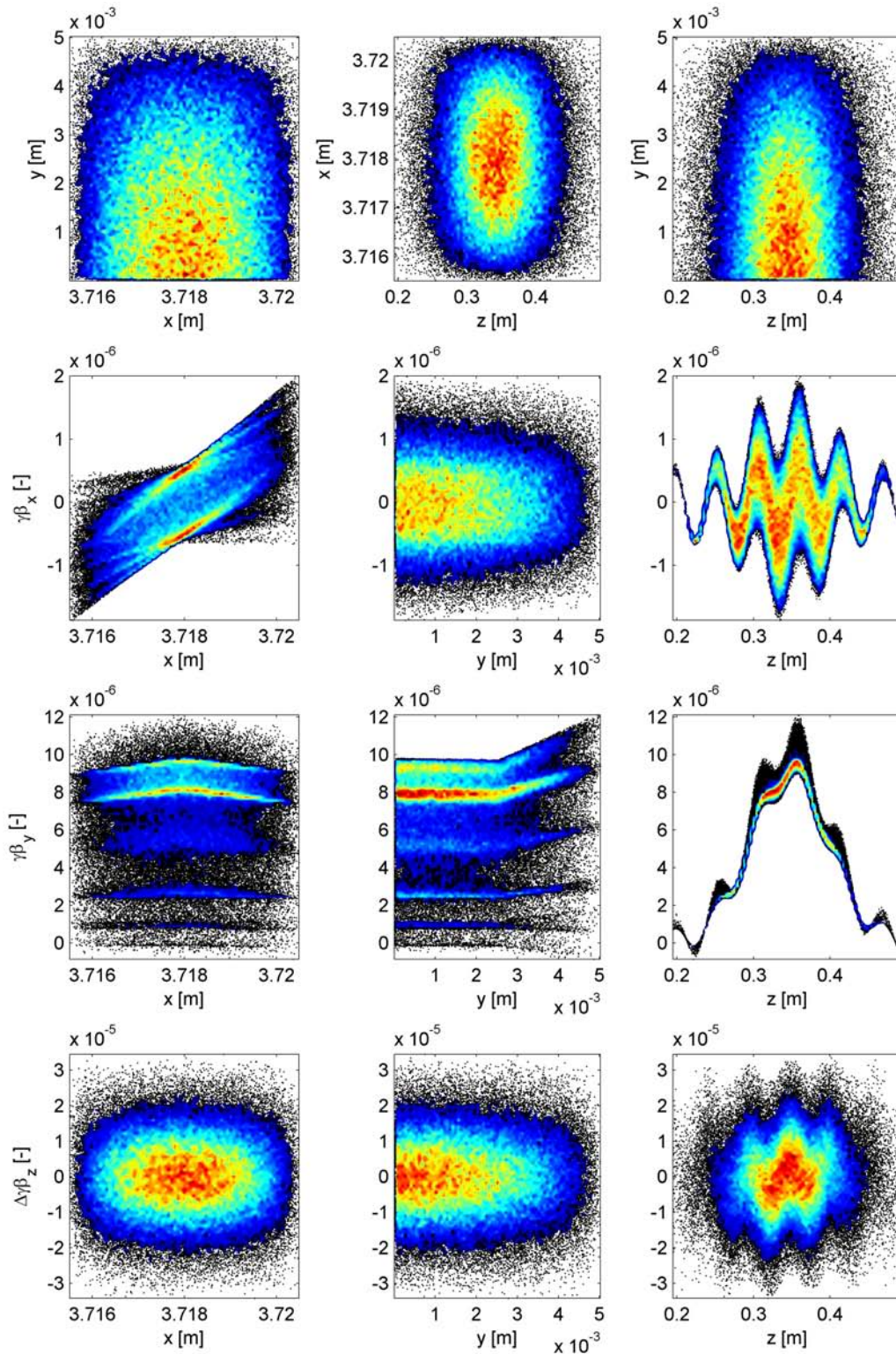
Figure 4.6: **Phase space after cavity crossing.** For the momentum in longitudinal direction is only the relative value indicated. The empty space under the curve in the $\gamma\beta_y - z$ space appears as numerical artifact due to the magnetic boundary condition in the beam plane.
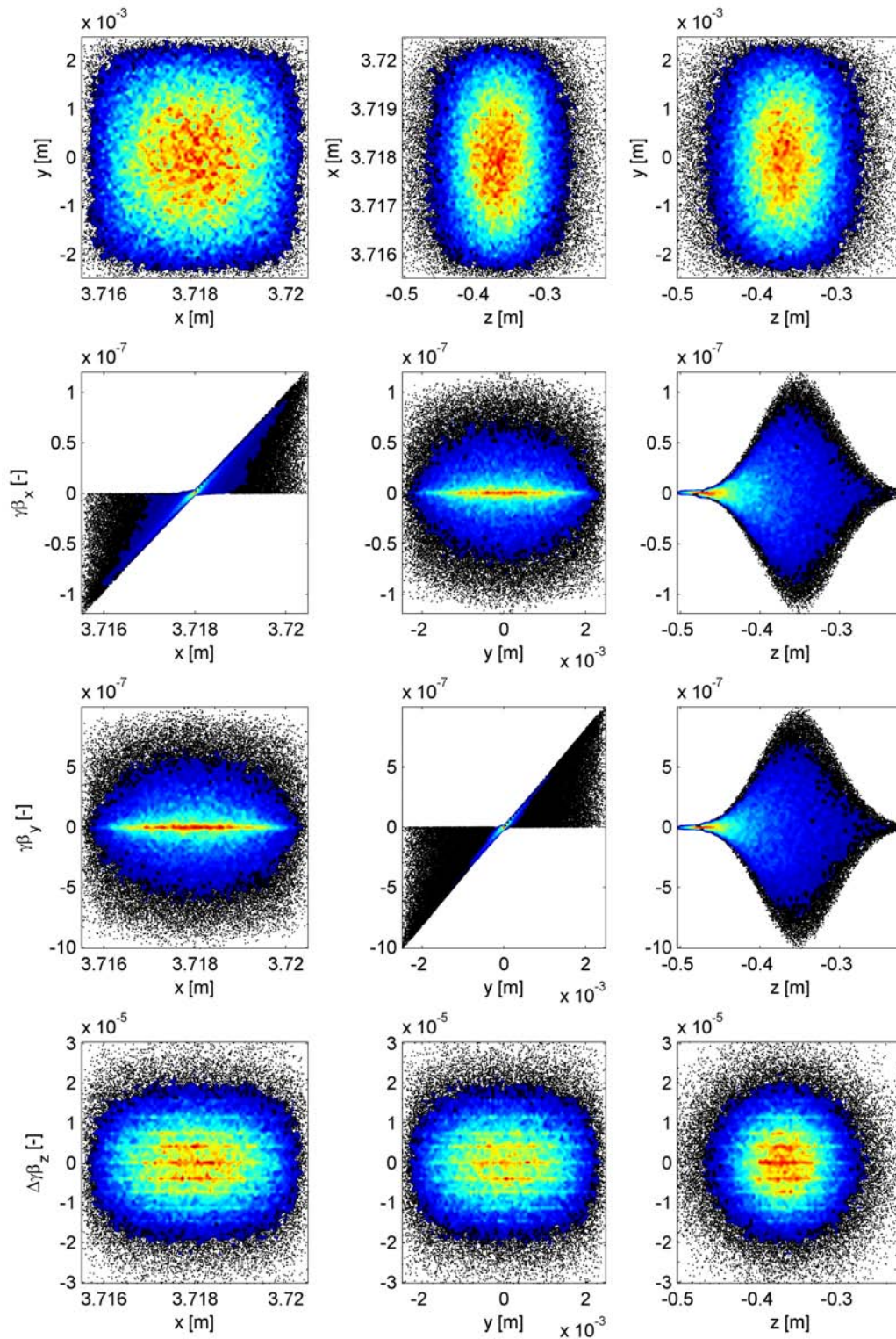
Figure 4.7: **Phase space before cavity crossing.** For the momentum in longitudinal direction is only the relative value indicated.
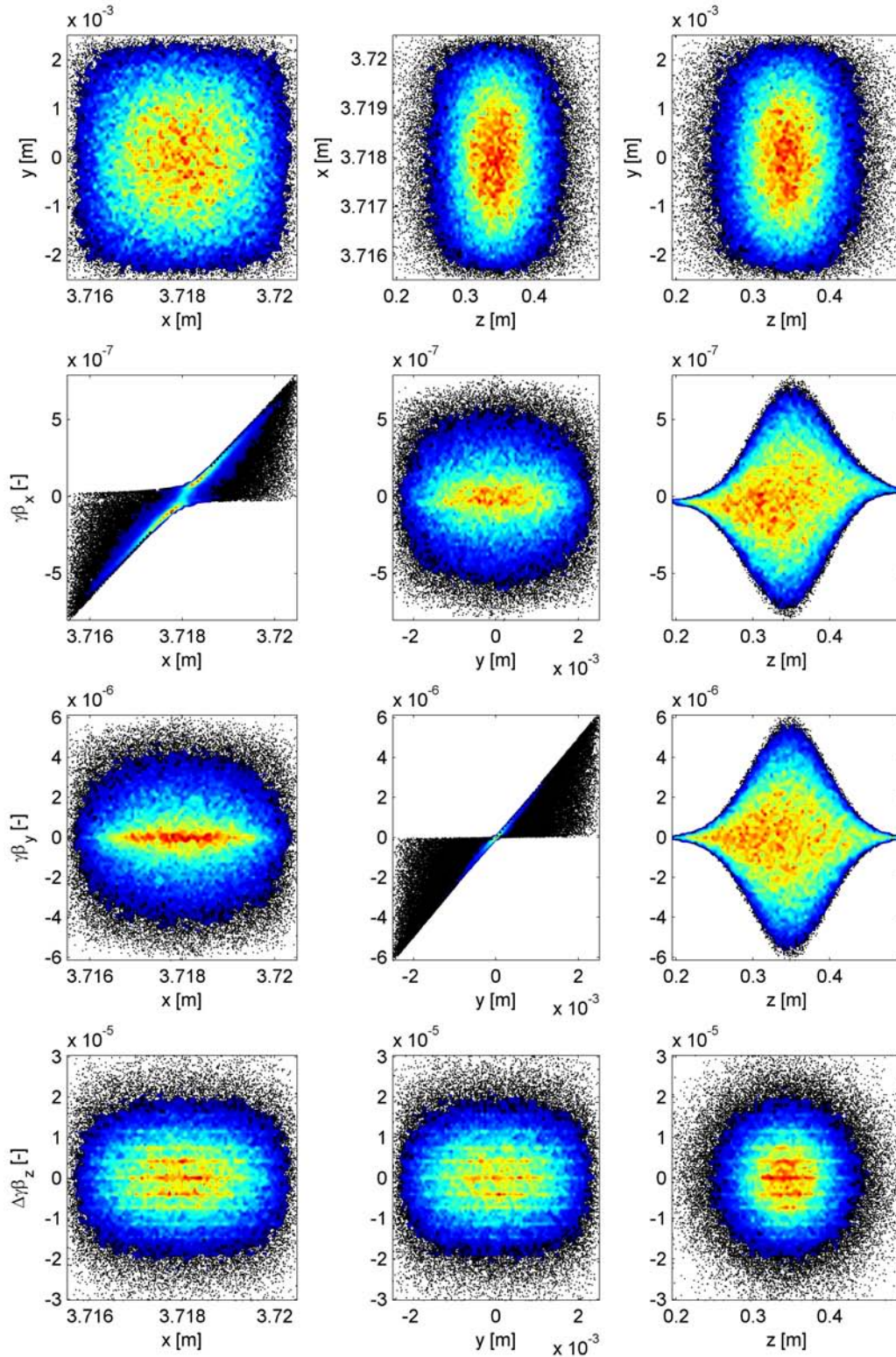
Figure 4.8: **Phase space after cavity crossing** For the momentum in longitudinal direction is only the relative value indicated.

components of the wake potential give the change in the transversal test particle voltage divided by q. The Fourier transform of the wake potential of a 590 MeV beam is shown in Fig. 4.9. Its value depends only on the transversal coordinates and the
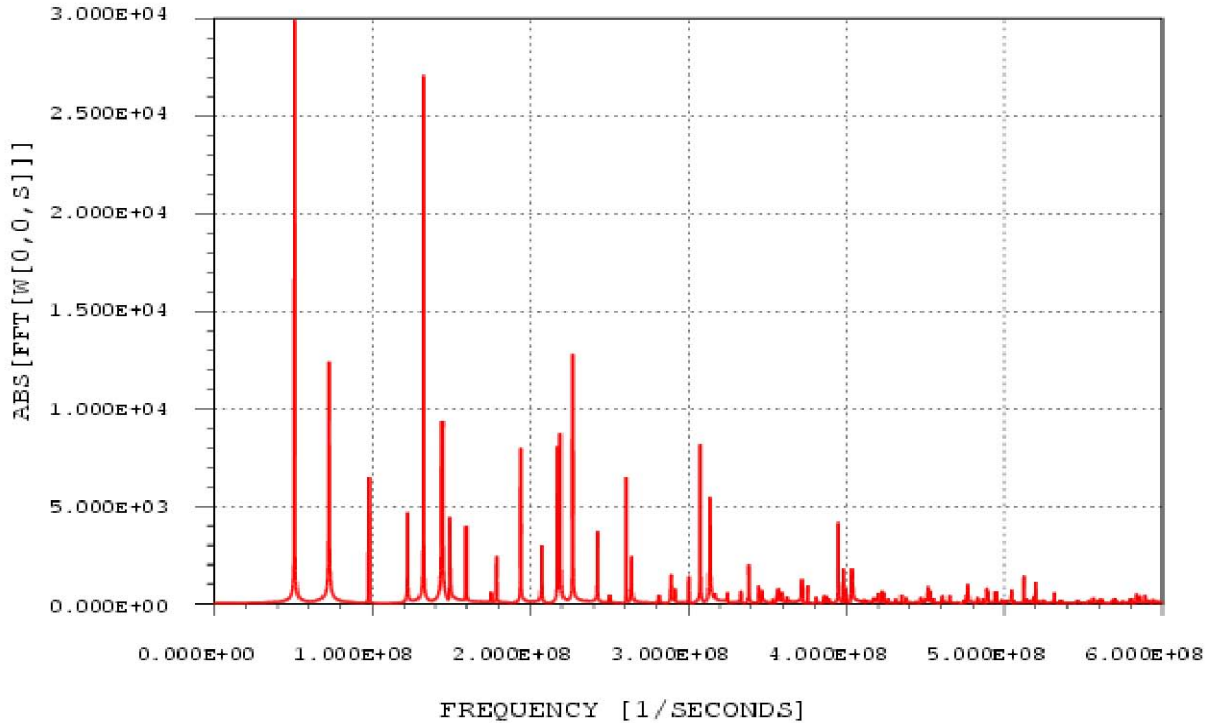

Figure 4.9: **Fourier transform of a wake integral with an integration length of 1000 m.**

frequency, and is a measure for the interaction between the particle beam and the accelerator structure. The spectral resolution in the rigid bunch model of MAFIA's T3 solver is achieved by choosing a very long wake integration length of 1000 m. This allows modes at frequencies higher than 100 MHz to be distinguished, but results in computation times of about one month on a DEC-alpha Tru64 machine.

4.2.3   Bunch Deformation in the Wake Field

The short-range effects of bunches with its own wake field and the wake field of its neighbors in radial direction are then analyzed in a combined rigid bunch T3 and PIC simulation. Increased beam currents of 3mA are chosen in order to investigate eventually limiting effects.

   In order to get an estimate of the short range effect on the phase space as well, the fields found in the T3 calculation are imported as initial field values into the self-consistent PIC solver (MAFIA's TS3 module). Bunches with a charge of 60pC and low velocity of 0.1c are propagated through the cavity. The particle monitors are set to register the phase space before and after cavity crossing for comparison. Space
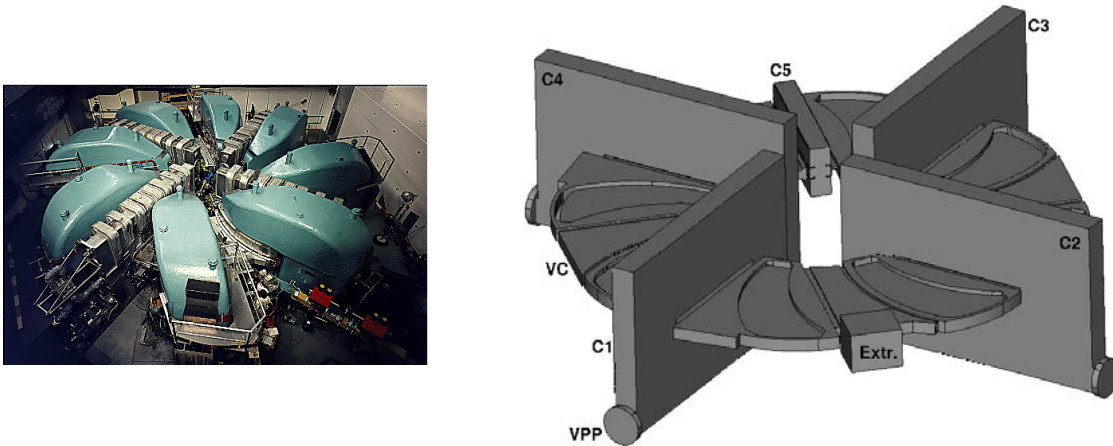
Figure 4.10: **Top-view on ring cyclotron (left) and RF-model (right).**
The ports for the vacuum pump (VPP), extraction (Extr.), angle between main cavities (C1-C4) and flattop-cavity (C5) break the symmetry. The vacuum-chamber (VC) interconnects the cavities.

charge effects and field deformation due to the close vacuum chamber wall can be observed (see fig. 4.7 and 4.8). The effects of the short range wake fields on the neighboring bunches are relatively low. More accurate simulations in MAFIA's time domain modules are impossible because of the poor approximation of the geometry by MAFIA's structured grid, the long computation times and memory limitations.

4.3 Eigenmode Calculation for the Ring Cyclotron

An even more detailed description of the field distribution inside the cyclotron can be found with a mode expansion technique, as described in section 2.1. For the calculation of the basis-function $\vec{e}_n$ in (2.17) it is required to calculate a set of eigenmodes. Equations (2.52 and 2.53) indicate that only eigenmodes with their resonance frequency close to a harmonic frequency can contribute significantly to the beam-excited field. On the other hand, the cyclotron structure has no exact symmetry in azimuthal- or vertical direction. The lower cut-off frequency of 56.4MHz for the beam slot opening in the main cavities leads to the consequence that eigenmodes can spread around the entire cyclotron structure and that the eigenmodes have therefore to be solved for the entire cyclotron structure.

It is intricate to find the eigenmodes in such a complex structure, where the modes are tightly clustered. The parallel Exact Shift Invert Lanczos (ESIL)-solver in Omega3P [43] was chosen for this purpose because it guarantees safe numerical convergence to the desired eigenmodes. Omega3P uses unstructured tetrahedral elements for the discretization of the simulation volume. This mesh can be generated with the CUBIT [21] program. The cyclotron geometry (see figure 4.10) has to be simplified in order
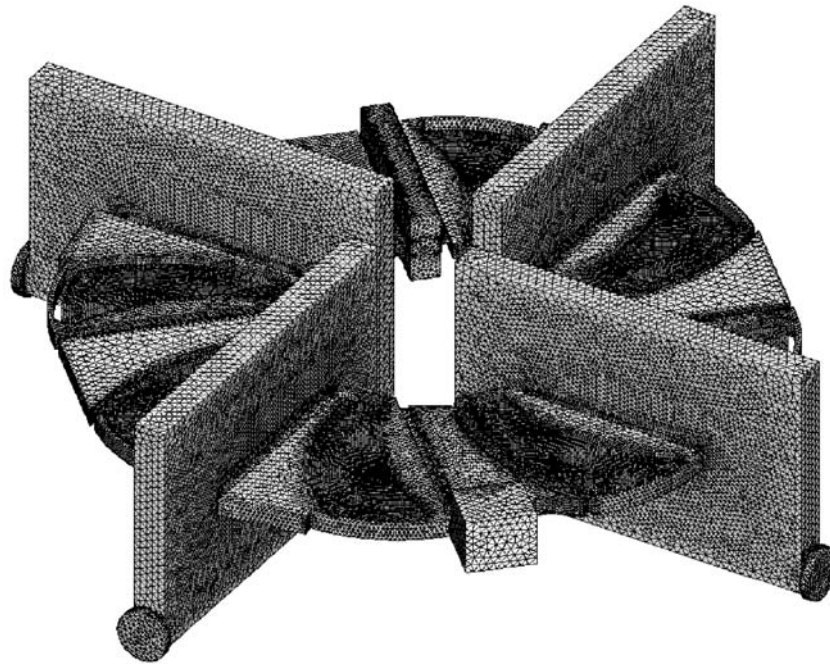
Figure 4.11: **Mesh of ring cyclotron.** CUBIT was used to generate a
mesh with about 1.2 million elements, leading to a problem
size of 6.9 million degrees of freedom if second-order ele-
ments are used.

to get a reasonable problem size. The dimensions are entered into CUBIT according
to the construction drawings of the cyclotron. However, it is known from measure-
ments that the shape of the biggest surfaces get slightly deformed when the cyclotron
is evacuated. Another simplification is the truncation at the vacuum ports without mod-
eling the absorbing vacuum pump structure. Insertion devices like radial beam position
measurement probes, electrostatic deflection septa and extraction magnets are omit-
ted as well. Wall losses are calculated with a perturbation technique. The surfaces with
ferromagnetic material are approximated by the same formulation as perfectly conduct-
ing boundaries for the field calculation and loss calculation by perturbation technique.
The inductive coupling loops for the excitation of the fundamental cavity modes and
connection to the final amplifier are neglected too.

4.3.1   The Mesh

CUBIT's filter function is used to classify the surface areas of the model according to
their size. The surface classes are then triangulated with increasing edge lengths. This
way, it is possible to generate a mesh with 1.2 million elements and 246 thousand
nodes only. Using curved second order elements, the average edge length of 6.4cm
leads to an upper frequency limit of 700MHz at least, if about six nodes are required
for the accurate representation of one wave-length.

4.3.2   Omega3P Calculations

SLAC's Omega3P [43] was run on a IBM-SP4 to find 280 eigenmodes with a resonance frequency close to a harmonic as illustrated in tab. 4.4.

50-136.5MHz	70 Modes	404.0-406.2MHz	20 Modes
143.6-157.5MHz	20 Modes	454.5-456.9MHz	20 Modes
195.4-207.8MHz	20 Modes	505.4-507.2MHz	20 Modes
245.7-260.4MHz	20 Modes	555.4-558.5MHz	30 Modes
299.3-308.2MHz	20 Modes	606.5-608.6MHz	20 Modes
353.8-355.6MHz	20 Modes		

Table 4.4: **List of the frequency intervals for the calculated modes.**

The typical solution time for 20 modes was about 45 minutes using 32 CPUs and required a total memory of about 120GB. Omega3P calculated the wall losses in a post processing-step. Because only one boundary wall material could be selected in this version of Omega3P[3], all the walls are supposed to be aluminum. This leads to an additional error in the loss calculation as some parts of the vacuum chamber are made of stainless steel.

4.3.3   Classification of the Calculated Modes

The modes in a cyclotron structure can be classified into three major groups. *Cavity modes* have their field energy localized in one of the cavities C1-C5. These modes could also be calculated in a rf model of the corresponding cavity only. *Vacuum chamber modes* have most of the field energy in the vacuum chamber and almost no field energy in the cavities. All other modes are *mixed modes* where energy is located in the vacuum chamber *and* in the cavities. A list with the parameters of the calculated modes can be found in appendix B.

Cavity Modes

A total of 44 modes are found for this class, among these obviously also the fundamental modes at 51.04MHz for the four main cavities and at 150.52MHz for the flattopping cavity. However, the operating frequency of these modes are at 50.633 and 151.8MHz respectively. This error between simulated and measured frequency comes from the difference between simulated and real geometry. For the main cavity, this is mainly due to geometry deformation by the air pressure and by the tuning system. In the case of the flattop cavity the electrodes had to be reprocessed and deviate from the length indicated on the drawings, leading to an additional error. The relatively low cavity beam slot cut-off frequency of 56.4MHz for waves with electric field in vertical direction leads

---

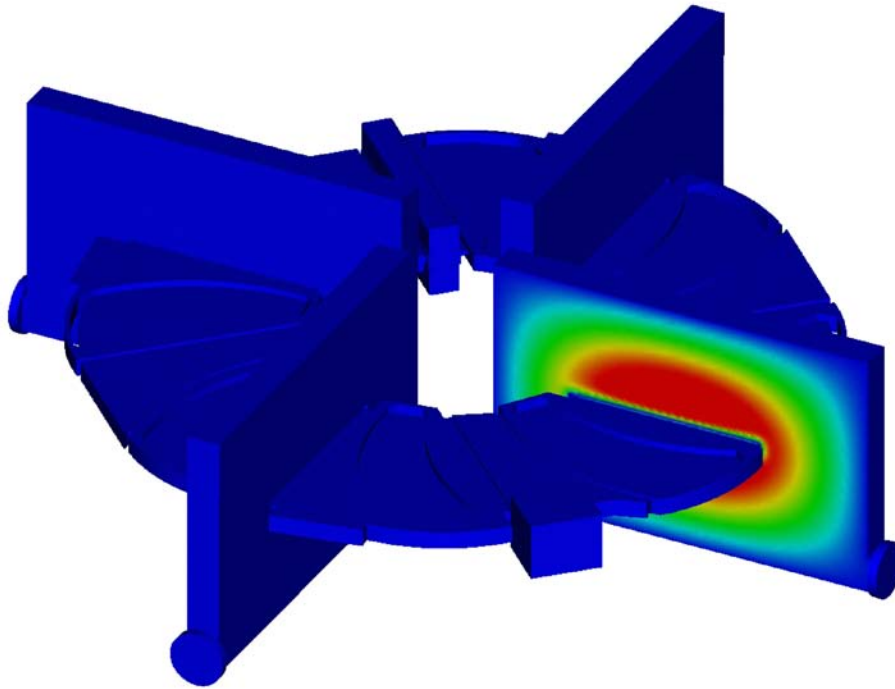[3]The wall loss calculation has now been improved for in the new version of Omega3P.

Figure 4.12: **Example of a fundamental cavity mode in cavity 2.**
Contour-plot of the electric field. The direction of the field
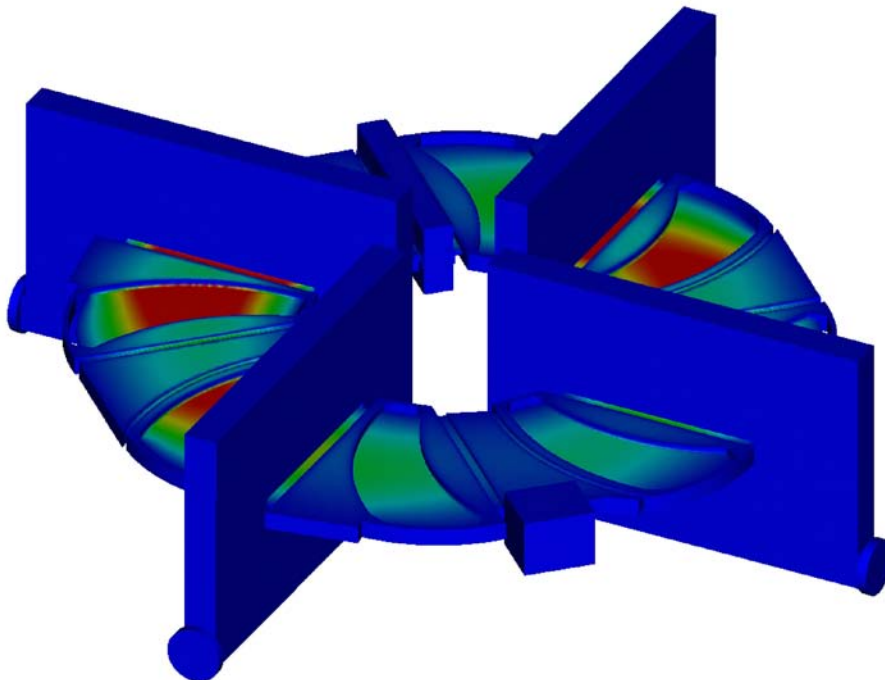vector is in particle-propagation direction.

Figure 4.13: **Example of a vacuum chamber mode.** Contour-plot of the
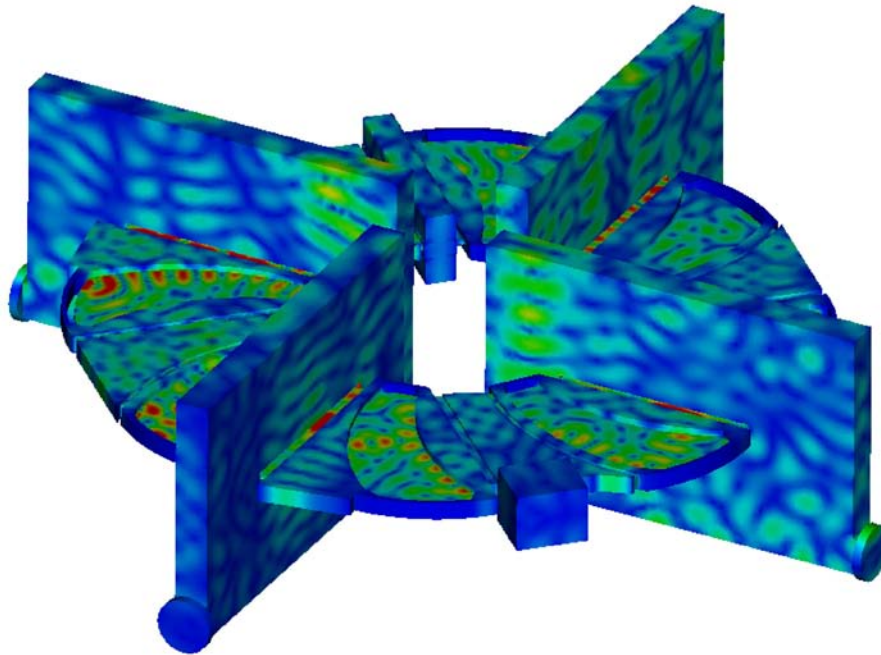vertical component of the electric field for the 54.685MHz
mode.

Figure 4.14: **Example of a mixed mode.** Contour-plot of the absolute value of the magnetic field for the 505.391MHz mode.

to very slight coupling of the modes at 100MHz and higher. At higher frequencies, these modes are no longer localized in one cavity and become mixed modes.

Vacuum Chamber Modes

The vacuum chamber modes have a vertical electric field distribution, a relatively low quality factor and appear at relatively low frequencies only. A total of 18 modes is calculated for this class. Their vertical electric field distribution suggests that their interaction with the beam must be relatively small.

Measurements of the lowest two vacuum chamber modes confirmed the simulation results. The coupling of these modes to the fundamental mode could also be interesting for the understanding of the rf leakage of the fundamental modes into the cyclotron structure. Measurements showed that the coupling could be reduced by a proper top-to-bottom symmetrization of the cavities. It is currently not clear up to which level these vacuum chamber modes contribute to multipactoring in the vacuum chamber and discharges in the electrostatic elements. During machine operation, it was also observed, that the sparking rate of the electrostatic elements depends on the position of some beam probes. This indicates that some part of the fundamental mode couples to the vacuum chamber.

Mixed Modes

The mixed modes are the most numerous ones with a total of 218 modes. They appear at higher frequencies and are tightly clustered. Because of the smaller wave length, their field pattern gets very dense. Therefore the beam interaction averages out and becomes less important. These modes probably couple to the vacuum port and therefore get slightly detuned when the vacuum shutter is opened.

4.3.4   Comparison with Measurement

The Omega3P simulations of the entire cyclotron structure found parasitic vacuum chamber modes, for example at 54.7MHz and at 57.5MHz. Measurements with a network analyzer confirm the simulation results. Because of the low transmission from the coupling loop to the capacitive pickup in the intermediate sector, an additional amplifier was added to the output of the network analyzer. The measured resonance frequencies at $54.7MHz$ and $57.5MHz$ correspond to the vacuum chamber modes. Cavity modes, on the other-hand, appear as sharp peaks at $51MHz$ and $72.2MHz$.

At higher frequencies, the modes get tightly clustered and the measured spectra therefore show overlapping of resonance curves. The curves also depend on the choice of pick-up positions for the transmission measurement, on the tuning and the temperature of the cyclotron (see also fig.4.17).

4.3.5   Dependence of the Eigenmodes on Air-Pressure and Temperature

The field distribution inside the cavity can be calculated more accurately in the Omega3P eigensolver[4] [43] than in MAFIA. This parallel eigenmode solver has the advantage of using an unstructured grid for a better representation of the rf geometry. CUBIT [21] was used for the generation of the cavity geometry and meshing of the structure. The cavity shape and part of the vacuum chamber was then represented by about 257'000 tetrahedral elements of second order. This yields a problem size of about 1.56M degrees of freedom. The nodes were then deformed linearly according to the deformation data, simulated with ANSYS [15]. Omega3P's ESIL solver found a set of about 30 eigenmodes in 18 minutes, using 16 CPUs of an IBM SP4 of the *Swiss National Supercomputing Centre*.

The resonance frequency of the fundamental mode shifted from 51.1 to 50.6MHz when the cavity shape is changed from non-evacuated state to evacuated and tuned operation. Figure 4.16 shows the change in resonance frequency of some modes with resonance frequencies close to the 11th harmonic frequency. The field distribution and coupling to the vacuum chamber changes slightly when the cavity gets deformed, and explains the non-linear dependence of the resonance frequencies of the HOMs.
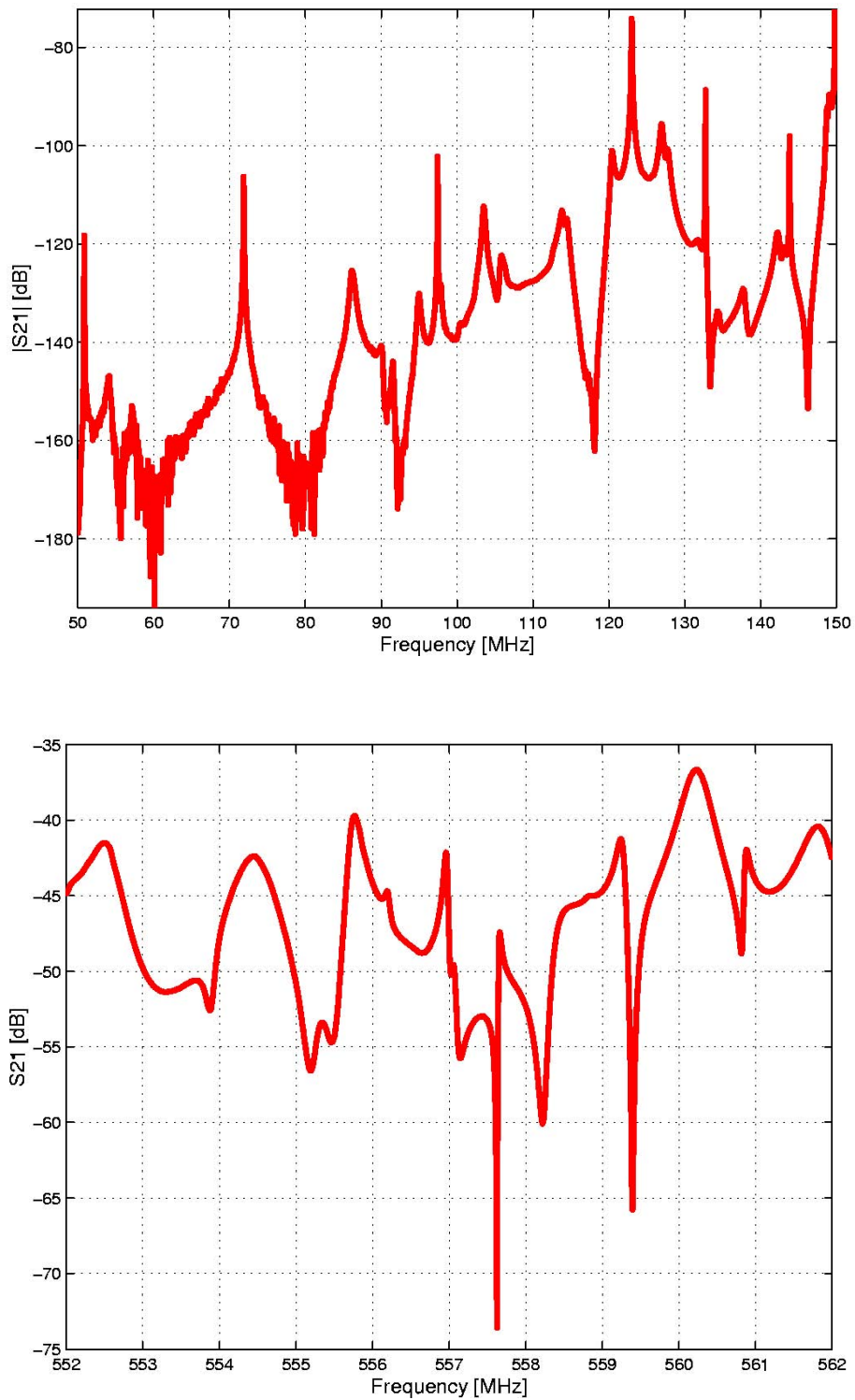
---

[4]see section 3.1

Figure 4.15: **Measured spectra of the ring cyclotron.** Transmission signal from coupling loop of cavity 2 to a capacitive pickup probe in the intermediate sector next to cavity 2.
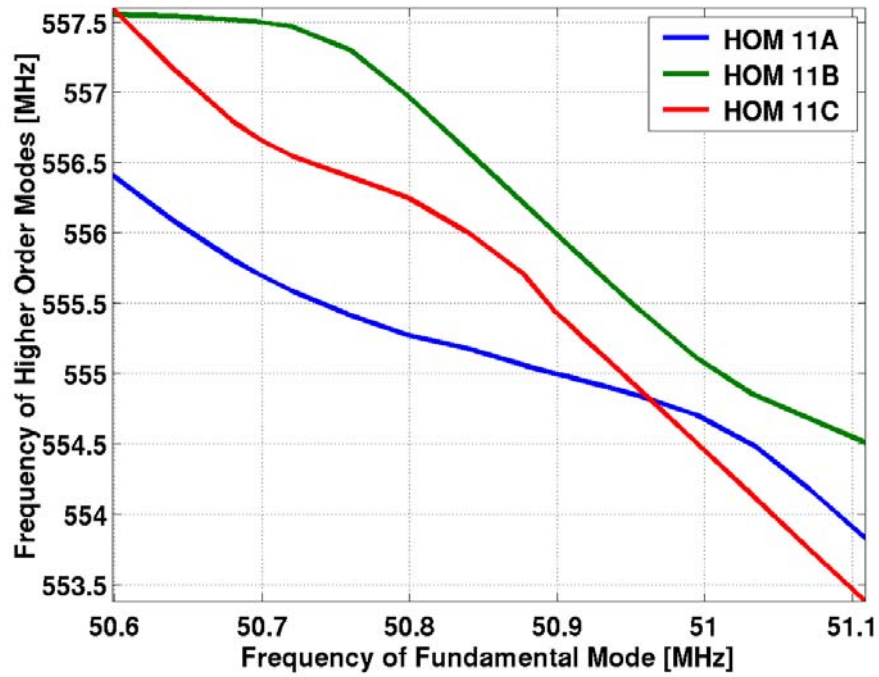
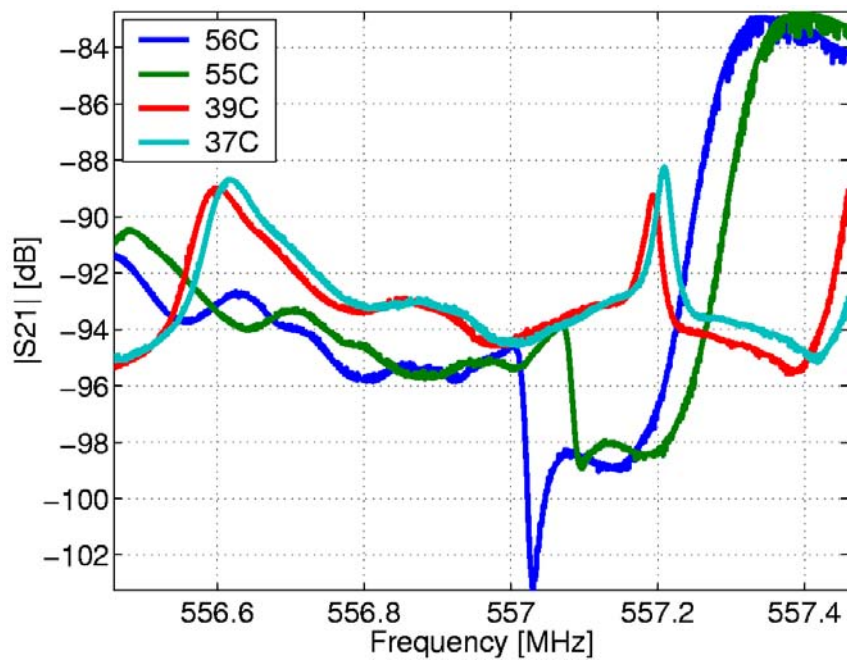Figure 4.16: **Calculated effect of cavity deformation on resonance frequencies.**

Figure 4.17: **Resonance spectra of cavity 2 at different temperatures.**

4.3.6 Measurement of the HOMs at Different Temperatures

An effort was made to get some measurement data about the shift in resonance frequency with temperature. Directly after full-power operation of the cavity, the network analyzer was connected from pick-ups *11* to *10* for transmission measurements. It was possible to record some transmission curves during the cool down period of the cavity of a few minutes.

Figure 4.17 indicates the shift in resonance frequency of some modes in function of the cavity temperature. The fundamental mode was tuned to stay at the operation frequency. It was not possible to keep the cavity tuned in the temperature interval from 40C to 54C and to measure additional curves in this interval. The change in transmission curves can be explained by the distortion of the cavity when it is cooled down. This effect shifts the resonance frequencies of HOMs with respect to the fundamental mode.

4.4 Beam Dynamics Simulations

4.4.1 Finding a Centered Orbit in the Cyclotron

In order to determine the particle trajectories in the cyclotron, a time domain particle path integration algorithm is used (section 3.2.1). The measured data of one sector magnet with 940A coil current and after shimming correction is provided by the *s03av.nar*-file. Assuming that all the sector magnets are identical, an azimuthal periodicity is used for the interpolation of these fields. The static magnetic field is rescaled by a factor of 0.999661 in order to get isochronous conditions at the propagating frequency of 50.63281MHz in the main cavities, and third harmonic in the flattop cavity. A linear correction function $f = 1 - 1.5 \cdot 10^{-4}(r - 1.5m)$, corresponding to the effect of the trim coils, is used for the reduction of the remaining phase error.

For better reproducibility, the effect of the fundamental modes on the cavities are reduced to momentum kicks on the particles when they cross the vertical mid-plane of a cavity. These kicks depend on the radial position and are corrected for transit-times and rf-phases, including the rf-magnetic field.

During normal high intensity production, the cyclotron parameters are adjusted for minimal extraction losses. This requires a large turn separation at extraction. If the injection parameters are chosen appropriately, a betatron precession of the beam can be excited, leading to well separated turns at extraction. However, the resulting precession in the cyclotron yields overlapping of the trajectories on other locations of the machine. For beam dynamics studies, it is desirable to adjust the beam parameters to get a well centered trajectory with separated turns everywhere in the cyclotron. This allows to count the number of turns, for example. For comparison with simulation, an algorithm was developed for the centering of the calculated trajectories: Five particle trajectories were determined and the noise on the phase error function calculated. This noise is a measure for the precession of the trajectory. A centered beam leads to a smooth phase error function with minimal noise, as illustrated in figure 4.19. The initial conditions of the particle *two* and *three* is chosen to deviate slightly in radial position
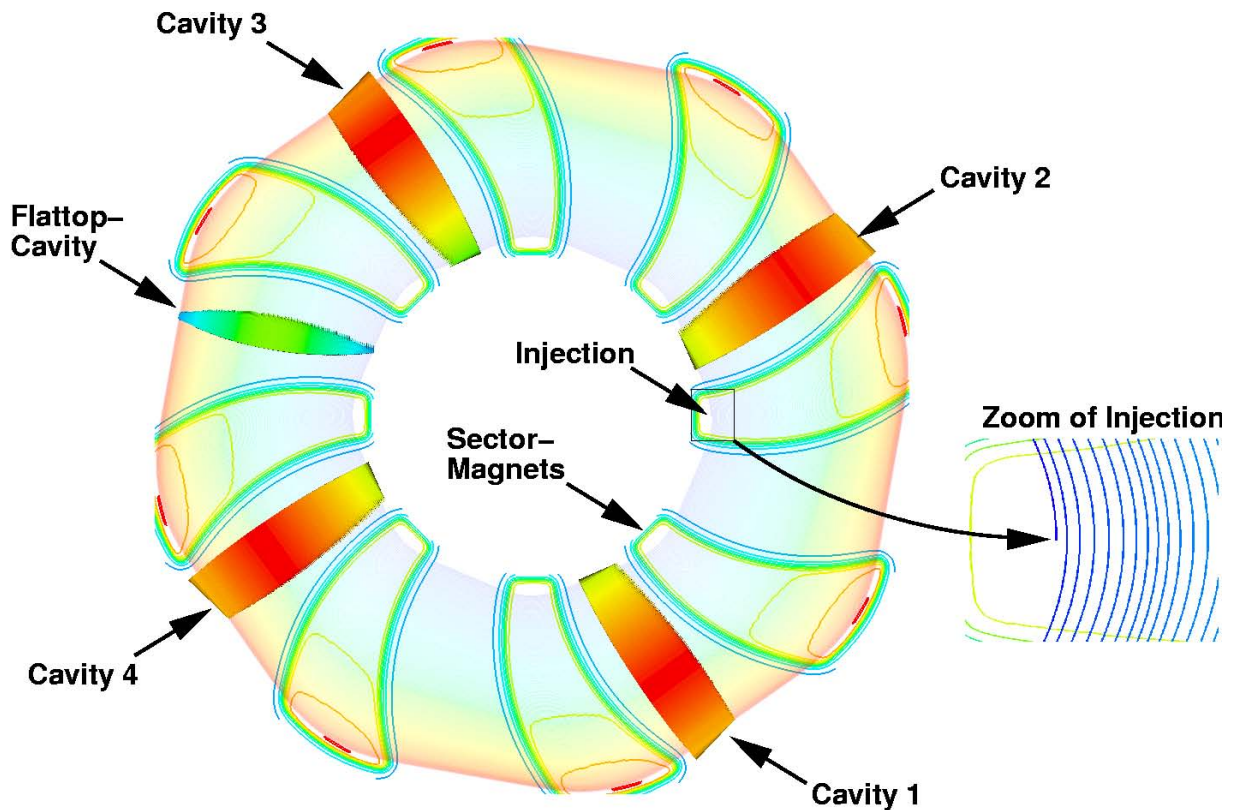
Figure 4.18: **Orbit calculation in the ring cyclotron.** The fine line, spiral-ing out from injection to extraction counter-clockwise, shows the particle path, with coloring according to the particle mo-mentum. The vertical component of the static magnetic field from the eight sector magnets is indicated by contour lines. Cones represent the gap voltage at the cavity-crossings of the particles.

and particles *four* and *five* in radial momentum with respect to particle number *one*. Comparing the noise level in the phase error function, the gradient for the improved initial conditions can be determined leading to a lower noise of the error function, and improved centering in the subsequent run.

4.4.2   Transfer Function for Robinson Instability Analysis

The particle tracking algorithm can also be used for a Robinson-Instability analysis. This beam loading model for storage rings was originally developed by K.W. Robin-son [62]. For the case presented there, all the particle bunches cross the cavity at the same location and the same energy, whereas in the case of the cyclotron they traverse the cavity at different radial positions and different energies. The knowledge of the cyclotron cavity-beam transfer function is the key to Robinson stability analysis.
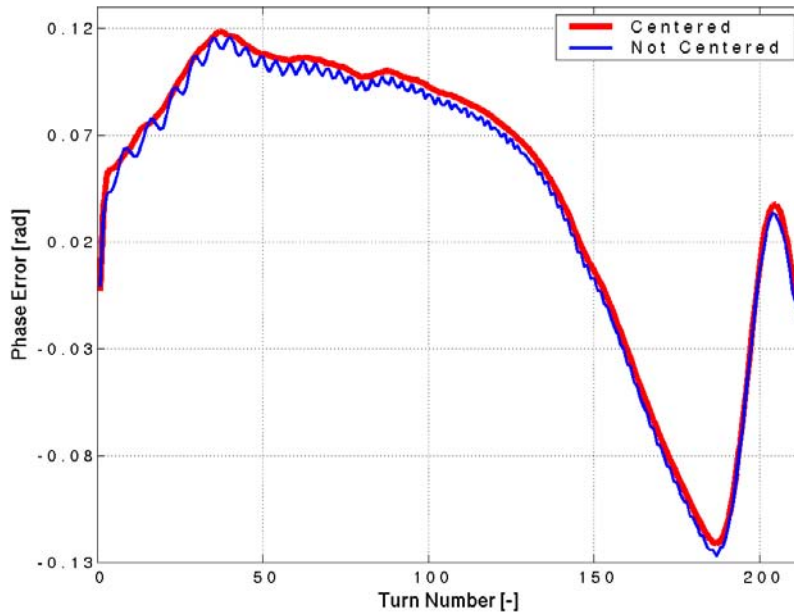
Figure 4.19: **Phase error of the centered trajectory.**

The action of the particles on the cavity modes can be calculated by Maxwell's equations using a mode expansion method for the electric field and Fourier decomposition of the flying particle bunches. The resulting differential equation of e.g. the fundamental mode is the same as for a lumped resonance circuit excited by the current source I_B, as shown in Fig. 4.20. The contribution to the amplitude of the fundamental mode at the steady-state condition can be approximated, according to the theory developed in section 2.3, by the sum over all turns at cyclotron radii r_t with velocity v_t and bunch length σ_t

$$\Delta V_C = Z_C I_B = -Z_C \frac{2I_0}{\hat{V}} \sum_t V(r_t) T(v_t) L(\frac{\sigma_t}{v_t}) \tag{4.2}$$

for a cavity with gap voltage distribution $V(r_t)$ and upper bound $\hat{V}$, shunt impedance Z_C, transit time correction $T(v_t)$ and long bunch correction $L(\sigma_t/v_t)$ for an excitation with mean proton current I_0.

Cavity-Beam Transfer Function   The cavity-beam transfer function $B(s)$ describes the effect of a small phase or amplitude modulation of the cavity voltage V_C on the beam-excited cavity voltage ΔV_C. The particle-tracking algorithm was used to calculate the variation in particle position and phase at the cavity when the cavity voltage was modulated.

The particle trajectory was integrated by a fourth order Runge-Kutta algorithm based on a third order Taylor expansion of the static magnetic fields, as described in section 3.2.
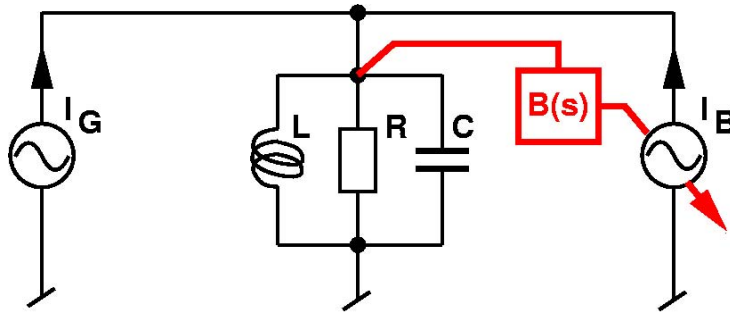
Figure 4.20: **RCL equivalence circuit of cavity fundamental mode with beam-excitation I_B and generator I_G.** The cavity-beam transfer function is highlighted in red.
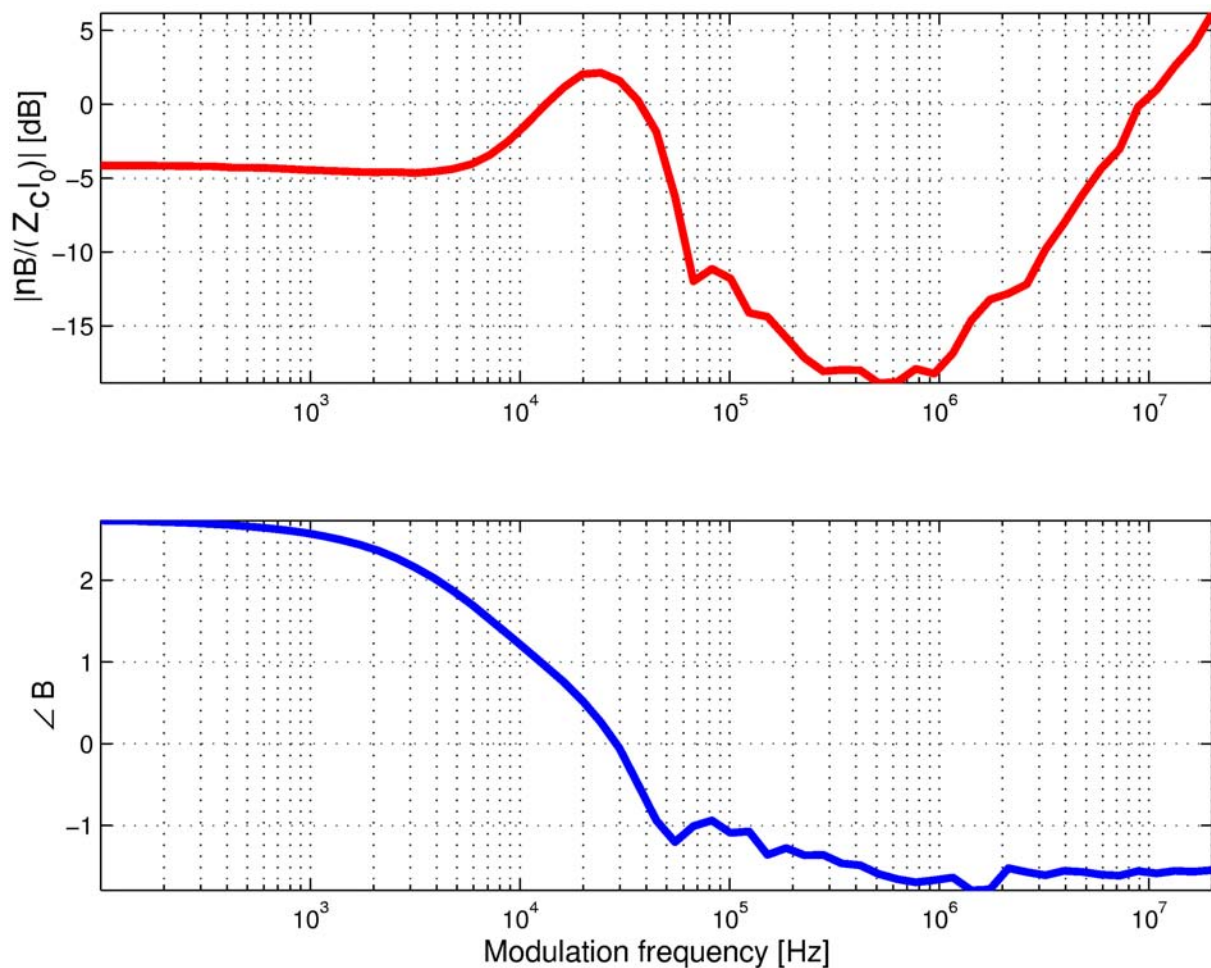

Figure 4.21: **Transfer function for phase modulation.** The upper plot indicates the amplitude- and the lower plot the phase of the cavity-beam transfer function. The transfer function is scaled by $Z_C I_0/n$.

The initial cavity voltages were adjusted to be in phase with $-I_B$, and to provide a particle end energy of 590MeV after 220 turns.
Single particle trajectories were calculated for different initial phases of the modulation signal, cavity crossings detected and the variation in each interaction contribution (VTL_t in equation 4.2) stored. The complex Fourier coefficients were then evaluated for each interaction and superimposed after being phase shifted by the delay of the corresponding turn number. Fig. 4.21 shows the resulting transfer function of cavity voltage to beam excited voltage V_C in cavity 3. The first bump corresponds to the transit time of the beam in the cyclotron. The upward trend above 1MHz is related to the revolution frequency at the sixth harmonic (8.4MHz).

The system would be unstable at beam currents higher than about $156\mu A$. But the additional feedback loop for amplitude and phase increases the maximum current considerably in the case of the fundamental mode. This method could also be extended to the interaction of the beam with higher order modes and the stability analysis of this system.

Although closed-loop measurements of the system confirmed that no instability appears up to proton beam currents of 1.9mA average intensity, the cavity-beam transfer function could be the key for future theoretical stability analysis of amplitude and phase control systems [54]. The method also allows calculation of the rf power requirements for the cyclotron.

4.4.3 Simulations with Space-Charge Correction

The tracking of one proton bunch with space-charge correction was performed from cyclotron injection to extraction. Because of the much stronger focusing of the cyclotron in vertical direction, the emphasis was made for the analysis of the beam evolution in horizontal phase space. About 130'000 macro particles were initialized close to the injection location as stabilized distribution, according to section 3.2.7. The PICN-model[5] provided the fast space-charge correction in horizontal direction.

Calculation of the particle evolution in the PSI Injector 2 cyclotron (without HOMs), for verification purposes, confirmed the "galaxy-like" shape deformation of the proton bunches, as predicted by *Adam* [1] and *Adelmann* [3]. Simulations of the bunch propagation in the ring cyclotron showed similar behavior for very short bunches.

Typical beam parameters used in the simulation of one bunch with space charge correction in the ring cyclotron are indicated in table 4.5

---

[5]see section 3.2.3

Transversal Radius	=	2.9mm	(standard deviation)
Beam Height	=	4.8mm	(height of needles)
Beam Length	=	52mm	(standard deviation)
Beam Current	=	1.8mA	(DC-value)
Energy	=	73.7 MeV	(second turn)

Table 4.5: **Typical Beam Parameters for the Initial Beam Conditions.**

A typical time step for the 4th order Runge-Kutta algorithm is 0.1ns with 1 space charge force calculation on 128×128 grid lines per 10 Runge-Kutta steps. This leads to calculation times of about 1 minute per turn, using 8 CPUs on the *Pegasus* computer at ETHZ.

The difference in rf-phase leads to a smaller energy gain for particles in the head and tail of the bunch than particles in the center of the bunch. This effect yields a banana-shaped deformation of the bunch with tips pointing to the center of the cyclotron. The flattop voltage can be adjusted to compensate this bending.

Space charge forces push particles away from the bunch center. Particles in the head get additional kinetic energy and particles in the tail get a reduction. This yields a S-shape deformation of the bunch, because the radii of equilibrium orbits increase with energy. The phase of the flattopping voltage can be adjusted to compensate the linear part of space charge effects. On the other hand, the rf magnetic field induces additional compression and decompression at the inner and outer radii of the flattopping cavity.

4.4.4 Gap Voltages of the HOMs

In order to get an estimate of the beam-cavity interaction in the ring cyclotron, the longitudinal and transverse "gap"-voltages are calculated. The relevant gap for the particles in this case means the trajectory from injection to extraction. Using the method developed in section 2, the beam-excited electromagnetic fields inside the cyclotron can be calculated for steady-state condition, corresponding to infinite operation time after switching on the beam with all the 1320 particle bunches in the cyclotron. The gap voltage of the electric- and magnetic fields E and B of a mode, can then be calculated easily from its definition:

$$V_l \equiv \frac{1}{q} \left| \int_{t=0}^{T_E} e^{j\omega_n t} \vec{E}(\vec{x}, t) \cdot d\vec{x} \right| \tag{4.3}$$

$$\frac{\partial V_r}{\partial r} \equiv \lim_{\Delta r \to 0} \frac{1}{q\Delta r^2} \left| \int_{t=0}^{T_E} e^{j\omega_n t} \Delta\vec{r} \cdot \left\{ d\vec{E}(\vec{x}, \Delta\vec{r}, t) + \vec{v} \times d\vec{B}(\vec{x}, \Delta\vec{r}, t) \right\} dx \right| \tag{4.4}$$

$$\frac{\partial V_z}{\partial z} \equiv \lim_{\Delta z \to 0} \frac{1}{q\Delta z^2} \left| \int_{t=0}^{T_E} e^{j\omega_n t} \Delta\vec{z} \cdot \left\{ d\vec{E}(\vec{x}, \Delta\vec{z}, t) + \vec{v} \times d\vec{B}(\vec{x}, \Delta\vec{z}, t) \right\} dx \right| \tag{4.5}$$

$$d\vec{E}(\vec{x}, \vec{\eta}, t) \equiv \vec{E}(\vec{x} + \eta, t) - \vec{E}(\vec{x}, t) \qquad d\vec{B}(\vec{x}, \vec{\eta}, t) \equiv \vec{B}(\vec{x} + \vec{\eta}, t) - \vec{B}(\vec{x}, t) \tag{4.6}$$

with the longitudinal, differential radial and axial gap voltages V_l, $\partial V_r/\partial r$ and $\partial V_z/\partial z$ respectively. The transverse differential gap voltages are an indication for transverse emittance growths. The trajectory $\vec{x}$, its vertical perpendicular perturbation vector $\vec{dr}$ and velocity v are functions of the time t between injection- and extraction time T_E. The charge of one bunch is chosen as normalization charge q. The angular frequency ω_n corresponds to the closest harmonic frequency.
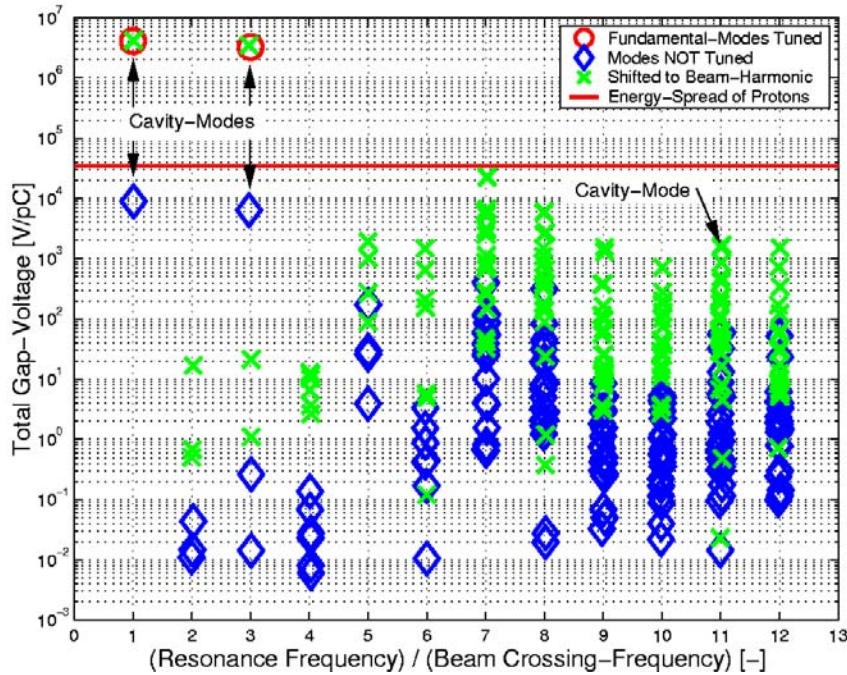

Figure 4.22: **Interaction in longitudinal direction.** The energy spread line corresponds to the value at 2mA operation. Fundamental modes of the main- and flattop cavities are highlighted by ∘. The cavity modes are indicated, all the other modes are mixed modes.

Only modes with a difference in resonance frequency to harmonic of less than 1.5MHz are considered, because other modes are negligible according to (2.52 and 2.53). Fig. 4.22 shows the spectrum of the beam excited modes. The blue diamond symbols indicate the results found for the modes with resonance frequencies calculated with Omega3P. As explained in the previous section, there is an important uncertainty in the simulated to the real resonance frequency. Therefore the upper bound of the mode excitation is indicated with a green cross symbol, obtained by shifting the resonance frequencies exactly to the corresponding harmonic.

The beam loading of the fundamental cavity modes is known from rf power measurements on the directional couplers of the cavities with and without beam. A small difference between measured and simulated gap-voltage in the fundamental modes can be explained by the uncertainty of the coupling factor to the final-stage amplifier.

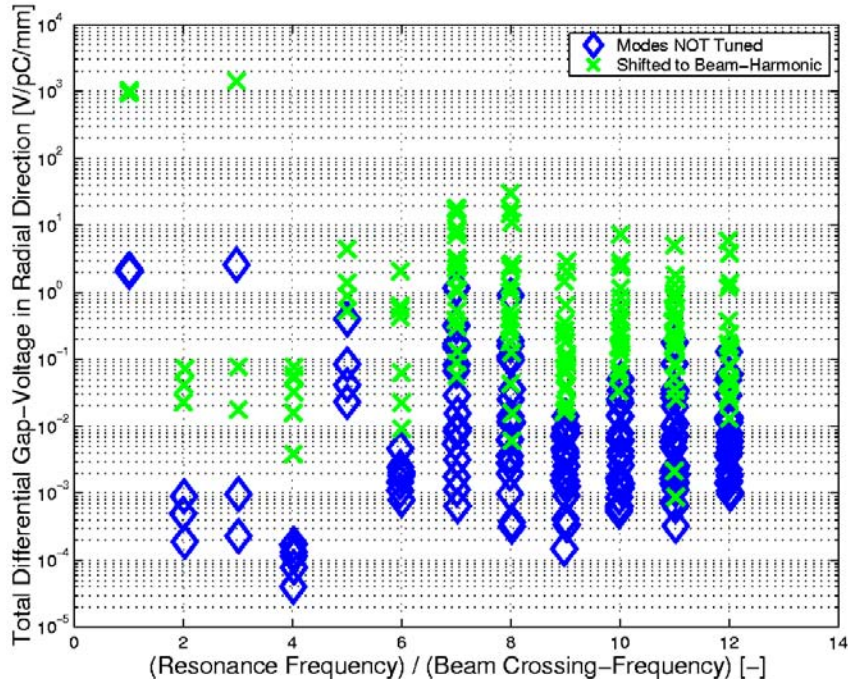Comparing the mode amplitudes with the measured energy spread of the particles

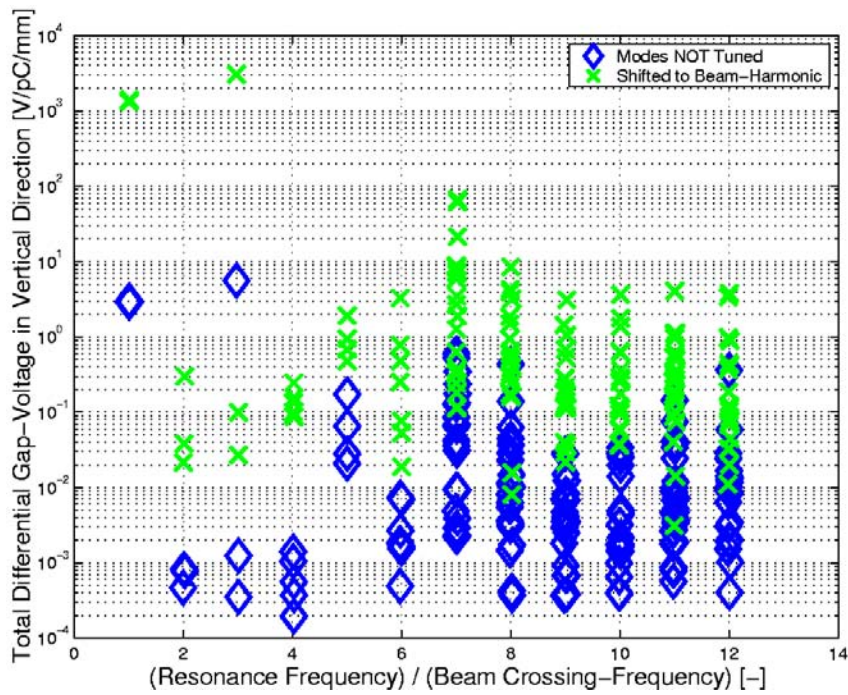Figure 4.23: **Interaction in radial direction**

Figure 4.24: **Interaction in vertical direction**

in the cyclotron, it can be seen that no mode can be excited strongly enough to lead to a relatively large additional energy spread. On the other hand, Fig. 4.22 indicates that the total energy gain per turn gets reduced by the beam excited modes.

For completeness figures 4.23 and 4.24 show the results for the radial- and axial direction respectively. The simulations confirm that the beam-cavity interactions have no big influence on the operation of the machine. This result is expected from the machine performance and from the HOM measurements where a linear dependence of HOM signal with beam current is observed. On the other hand, this results also validate the perturbation approach chosen for the calculation of the excitation and the effect on the particle distribution.

Improvements of the model can be made by adding more details to the geometry, taking the effect of the air pressure on the surface curvature into account and simulating the wall materials more accurately.

4.4.5 Effect of HOMs onto the Beam Quality

Using the previously calculated eigenmodes of the entire cyclotron for the representation of the beam excited fields, it is possible to add the corresponding Lorentz forces to the tracking code with space charge correction. As already illustrated in section 4.4.4, there is a part of the particle energy transferred to the HOMs. Ohmic losses limit the amplitudes of the beam-excited modes, and the amplitudes of the fundamental modes are to be increased accordingly to compensate the energy loss in the beam.
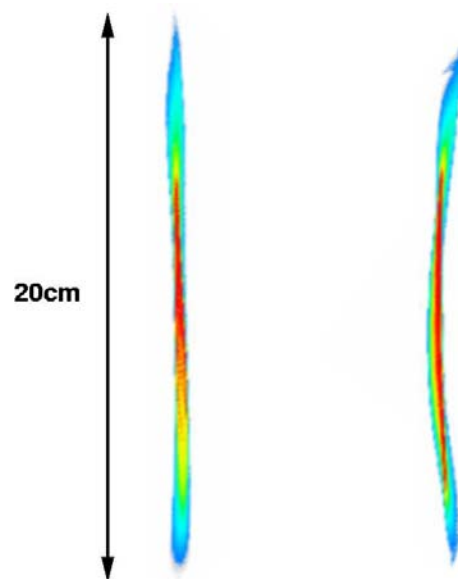

Figure 4.25: **Horizontal Charge distribution at extraction location (214 turns) without (left) and with beam-excited HOMs (right).** Propagation direction is upward, the center of the cyclotron is to the left. The beam current is 1.8mA.

The amplitudes and phases of the beam excited modes are calculated in the frequency domain, as described in chapter 2. It follows from this theory that the amplitudes depend on the difference from the resonance frequency of the mode to the nearest beam harmonic frequency. Evidently, the amplitude and phase also depend on the field distribution of the mode in the beam plane, according to (2.58 and 2.59). In the simplified description used here for the simulation, it is supposed that the bunch deformation is small and that the mode-amplitudes depend linearly on the beam current.

Figure 4.25 illustrates the effect of HOMs onto the charge distribution. The coloring corresponds to the charge density (linear scaling). There are 30 particularly critical beam-excited modes selected and the resonance frequencies are shifted to exactly the nearest beam harmonic. This bunch deformation therefore presents a "worst-case" situation. The mode damping will be more important in the real cyclotron, and the resonance frequencies do not necessarily fall exactly on a beam harmonic. There is no significant deformation visible if the modes are not shifted exactly to the beam harmonic.

4.5   Summary

For the first time ever, it was possible to calculate eigenmodes of the entire ring cyclotron. Omega3P's ESIL-solver finds the HOMs required for the representation of the beam-excited cyclotron fields. The investigation of the bunch deformation by these fields was performed by calculating the propagation of macro-particles from injection to extraction. For the first time ever, a numerical particle-in-cell simulation was done for the ring cyclotron. This permitted the simulation of beam-cavity interactions in the entire ring cyclotron.

However, quantitative predictions of limitations for the cyclotron operation by beam excited HOMs are very difficult. This is mainly due to the high sensitivity of the result on the calculated resonance frequency and wall losses. Both parameters are affected by the simplifications of the cyclotron geometry.

Chapter 5

CONCLUSIONS

In this thesis, simulation tools were developed which analyze the influence of beam generated rf-fields on the beam dynamics of sector focused cyclotrons. Effects of HOMs, phase-slip and space-charge onto the beam stability and quality can be simulated.

Additionally, the simulation of not only one cavity, but the entire cyclotron structure enables us to find eigenmodes of parasitic cyclotron modes.

The application of these tools to the PSI ring cyclotron shows that only a small degradation of the beam quality occurs by beam-excited HOMs at proton beam intensity levels of about 2mA.

The linear dependence of the measured beam-excited HOM confirms that no instability or resonance occurs at these power levels.

However, the comparison of calculated quality factors with measurement shows that the accuracy for quantitative predictions is still limited. The measured HOMs are much stronger damped than in the simulation. Simplifications made in the geometry of the simulated rf-structure also lead to a deviation of the simulated resonance frequency. These effects finally lead to a non-quantifiable error in the simulated amplitudes of beam-excited modes.

The computer account used for the calculation of the corresponding rf-structure at the *Swiss National Supercomputing Centre* is currently restricted to a memory usage of about 120 GB; just about the size to allow a simulation. Refined simulations would therefore require larger computing resources.

5.1   Suggestions for Future Efforts

As soon as the phase space at injection and extraction, as well as the effects of neighboring turns are known from 6d beam-dynamics simulations, it can be decided if the

PICN model has to be improved or not. One small modification would be, for example, the introduction of a varying rod length according to the vertical beam size. Other fast space-charge correction methods [56, 48] might also be interesting to investigate further for the case of the ring cyclotron.

Refined simulations with this method are interesting for intensity upgrade studies of the ring cyclotron and the design of future high power cyclotrons for Accelerator Driven Systems [70]. Strong deformation of the bunches appearing at higher intensities might require to go beyond the limits of the rigid bunch model. The easiest approach is to just rerun the calculation of the mode amplitudes and phases with the previously calculated beam parameters of the bunch in the beam excited HOMs. This can be repeated until the required convergence is reached. The perturbation approach, described in section 2.1.3 on the other hand, would lead to much faster execution times. A self consistent calculation could be performed by a time-domain integration of the bunches with a mode-expanded representation of the electromagnetic fields by evaluation of equation (2.40) at each time step.

The accuracy of the eigenmode calculation could be improved in several ways. As soon as increased computing resources or improved numerical methods become available, more details should be added to the rf-structure of the ring cyclotron and effects of absorbing boundaries (like vacuum pump port, magnets and windows) should be included. Unfortunately, simulations with absorbing boundaries lead to eigenmodes which are no longer orthogonal, and couple mutually.

Appendix A

The Analytical Model

An analytical model is used for a first estimate of the effects and comparison with measurements. It consists of a rectangular box cavity and simplified static magnetic cyclotron field. About 2302 modes with resonance frequencies in the range of 50MHz to 1GHz are found. A correction for the electrodes and deformation due to the air pressure is introduced to the resonance frequency calculation by the Slater method.

A.1   Field Distribution in a Box Shaped Cavity

The cavity geometry in figure A.1 is an approximation of the aluminum main cavity of the PSI ring cyclotron. The proton beam is accelerated in z-direction by the fundamental cavity mode and is located in the mid-plane at $y = a/2$.
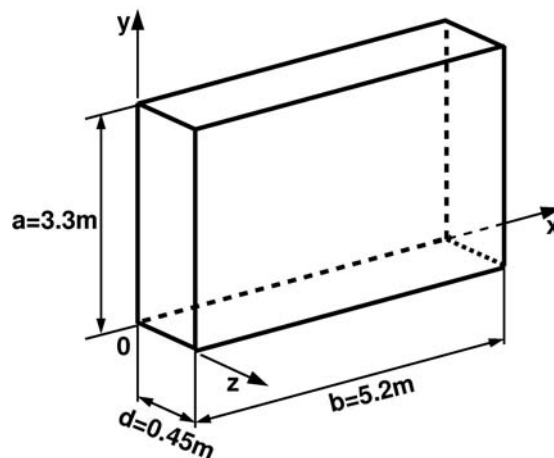

Figure A.1: **Geometry of the rectangular box shaped cavity.** Electrodes are neglected.

With the objective to find an analytical field solution for an ideal, perfectly conducting

cavity, the boundary condition problem (2.17) can be written as

$$\begin{cases} \Delta\vec{e} + \frac{\lambda_n}{c^2}\vec{e} = 0 \\ \nabla \cdot \vec{e} = 0 \qquad \{x,y,z|(x \in]0,b[) \wedge (y \in]0,a[) \wedge (z \in]0,d[)\} \\ \hat{n} \times \vec{e} = 0 \qquad \{x,y,z|x = 0 \vee x = b \vee y = 0 \vee y = a \vee z = 0 \vee z = d\} \end{cases} \tag{A.1}$$

The eigenmodes in a box-cavity can be calculated according to *Poeschl* [55]. Its field-solution is then a superposition of H-type and E-type fields

$$\vec{E} = \begin{pmatrix} \frac{\partial^2 u}{\partial z \partial x} - j\omega\mu_0 \frac{\partial u^\times}{\partial y} \\ \frac{\partial^2 u}{\partial z \partial y} + j\omega\mu_0 \frac{\partial u^\times}{\partial x} \\ \frac{\partial^2 u}{\partial z^2} + k^2 u \end{pmatrix} \qquad\qquad \vec{H} = \begin{pmatrix} j\omega\varepsilon_0 \frac{\partial u}{\partial y} + \frac{\partial^2 u^\times}{\partial z \partial x} \\ -j\omega\varepsilon_0 \frac{\partial u}{\partial x} + \frac{\partial^2 u^\times}{\partial z \partial y} \\ \frac{\partial^2 u^\times}{\partial z^2} + k^2 u^\times \end{pmatrix} \tag{A.2}$$

The scalar potential for the H-type field is denoted as $u^\times$ and the one for the E-type field as u.

$$u^\times \equiv A^\times \cos(k_x x)\cos(k_y y)\sin(k_z z) \qquad\qquad u \equiv A\sin(k_x x)\sin(k_y y)\cos(k_z z) \tag{A.3}$$

with wave-vector

$$k_x = \frac{\pi l}{b} \qquad\qquad k_y = \frac{\pi m}{a} \qquad\qquad k_z = \frac{\pi n}{d} \tag{A.4}$$

for the boundary condition and frequency

$$k^2 \equiv \frac{\omega^2}{c^2} = k_x^2 + k_y^2 + k_z^2 \qquad l, m, n, \in \mathbb{Z}. \tag{A.5}$$

H_z is proportional to $u^\times$. In the oscillation state H_{lmn}, the indices l, m, n describe the number of node-surfaces perpendicular to x-, y- and z-axis. For $b > a$ is ω_{101} the lowest eigenfrequency of H-type and for H_{0mn} are only the components E_x, H_y, H_z non-zero. If $k_z = 0$ or both $k_x = 0$ *and* $k_y = 0$, it follows that $H_z \equiv 0$ and modes of type H_{lm0} or H_{00n} therefore do not exist.

For E-waves the oscillation types E_{0mn}, E_{l0n} and E_{00n} vanish. The resonance frequencies ω_{lmn} are the same as for the H-type and the eigenvalues $k_{lmn} = c\omega_{lmn}$ are degenerated, except k_{0mn} and k_{l0n}. It is straight-forward to show that the field solutions satisfy (A.1) and the orthogonality condition (2.20). It follows from the property of degenerated modes [20], that the linear combination of degenerated H_{lmn} and E_{lmn} modes is a new eigensolution with the same resonance frequency, and that the quality factors are therefore not uniquely defined. The field distribution of the set of eigenmodes also depends on the orientation of the coordinate system. It is straight-forward to show that the corresponding fields can be reconstructed by linear combination of the degenerated H_{lmn} - and E_{lmn} modes.

The total energy of the electromagnetic field can be expressed from the energy stored in the electric field (2.34).
If $l = 0$ and $m, n > 0$:

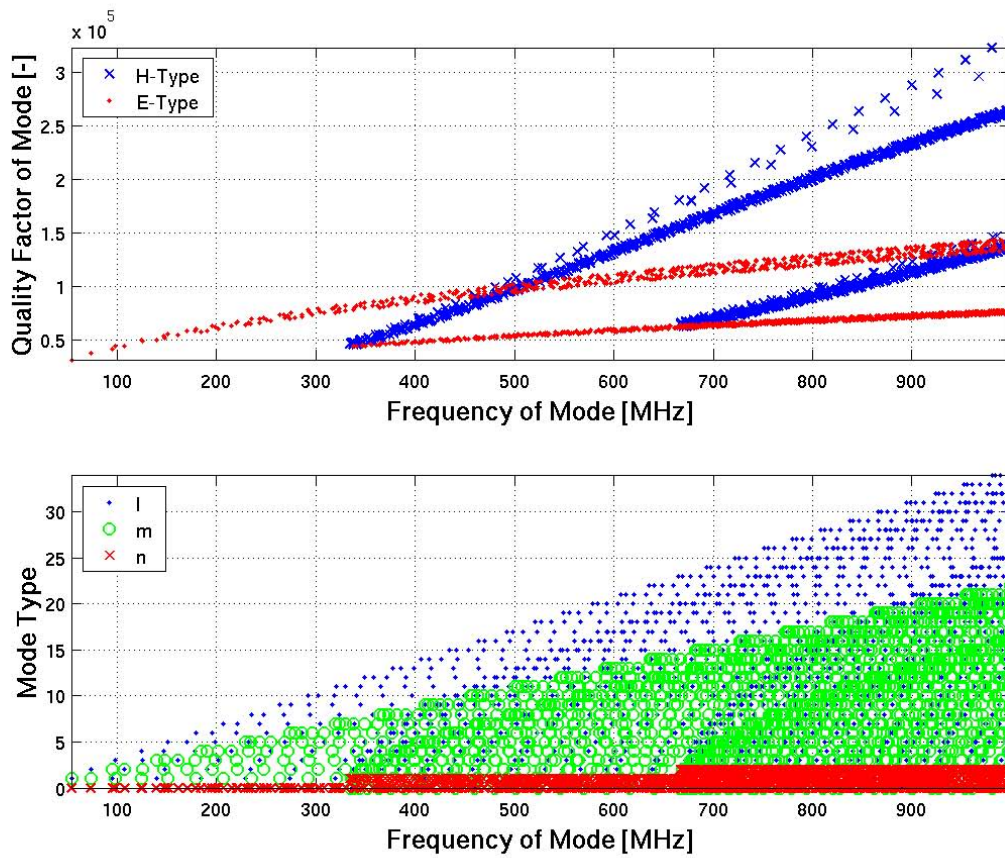$$U^\times(0, m, n) = (\mu_0\omega A^\times)^2 \frac{\varepsilon_0 \pi^2 m^2 b d}{8a} \tag{A.6}$$

Figure A.2: **Mode parameters of a box shape cavity:** 2302 modes are found in the interval from 50MHz to 1GHz! Mode-type indicates the numbers for the corresponding H_{lmn} and E_{lmn} modes.

If $m = 0$ and $l, n > 0$:

$$U^\times(l, 0, n) = (\mu_0\omega A^\times)^2\frac{\varepsilon_0\pi^2 l^2 ad}{8b} \tag{A.7}$$

If $n = 0$ and $l, m > 0$:

$$U(l, m, 0) = A^2\pi^4\varepsilon_0 d\frac{l^4a^4 + 2l^2m^2b^2a^2 + b^4m^4}{8b^3a^3} \tag{A.8}$$

If $l, m, n > 0$:

$$U^\times(l, m, n) = (\mu_0\omega A^\times)^2\pi^2\varepsilon_0 d\frac{m^2b^2 + l^2a^2}{16ab} \tag{A.9}$$

$$U(l, m, n) = A^2\pi^4\varepsilon_0\frac{2\,d^2l^2b^2m^2a^2 + d^2b^4m^4 + n^2l^2b^2a^4 + d^2l^4a^4 + n^2m^2b^4a^2}{16d\,a^3b^3} \tag{A.10}$$

The losses in the cavity walls with skin-depth $\delta = \sqrt{2/(\mu\sigma\omega)}$, according to (2.29), and wall conductivity σ are given by the cavity currents, being proportional to the tangential magnetic field value, as described in section 2.0.2. For the cavity walls built from aluminum it results that $\mu = \mu_0$ and $\sigma = 3.3 \cdot 10^7/m/\Omega$.

$$P_C = \frac{1}{2\sigma\delta}\left[\int_0^b\int_0^a |H_t|^2_{z=0} + |H_t|^2_{z=d} \, dxdy + \int_0^a\int_0^d |H_t|^2_{x=0} + |H_t|^2_{x=b} \, dydz\right.$$
$$\left. + \int_0^b\int_0^d |H_t|^2_{y=0} + |H_t|^2_{y=a} \, dxdz\right] \tag{A.11}$$

The unloaded quality-factor Q_0 can now be determined by its definition (2.37) neglecting external-loading (2.85).

If $l = 0$ and $m, n > 0$:

$$Q_0^\times(0, m, n) = \frac{c\pi\mu_0\sigma\delta}{2}\frac{b(m^2d^2 + n^2a^2)^{3/2}}{2n^2a^3b + d^3am^2 + da^3n^2 + 2m^2d^3b} \tag{A.12}$$

If $m = 0$ and $l, n > 0$:

$$Q_0^\times(l, 0, n) = \frac{c\pi\mu_0\sigma\delta}{2}\frac{a(l^2d^2 + n^2b^2)^{3/2}}{2n^2b^3a + d^3bl^2 + db^3n^2 + 2l^2d^3a} \tag{A.13}$$

If $n = 0$ and $l, m > 0$:

$$Q_0(l, m, 0) = \frac{c\pi\mu_0\sigma\delta}{2}\frac{d(l^2a^2 + m^2b^2)^{3/2}}{m^2b^3a + 2m^2db^3 + a^3l^2b + 2l^2da^3} \tag{A.14}$$

If $l, m, n > 0$:

$$Q_0^\times(l, m, n) = \frac{c\pi\mu_0\sigma\delta}{4}\left(l^2d^2a^2 + m^2b^2d^2 + n^2b^2a^2\right)^{3/2}\left(m^2b^2 + l^2a^2\right)\bigg/\bigg\{a^3n^2b^5m^2$$
$$+ a^5n^2b^3l^2 + d^3a^5l^4 + da^3n^2m^2b^4 + d^3am^4b^4 + 2d^3a^3m^2l^2b^2 \tag{A.15}$$
$$+ 2d^3b^3m^2l^2a^2 + db^3l^2n^2a^4 + d^3b^5m^4 + d^3bl^4a^4\bigg\}$$

$$Q_0(l, m, n) = \frac{c\pi\mu_0\sigma\delta}{4}\frac{(m^2b^2 + l^2a^2)\sqrt{l^2a^2d^2 + m^2b^2d^2 + n^2b^2a^2}}{b^3m^2a + b^3m^2d + l^2a^3b + l^2da^3} \tag{A.16}$$
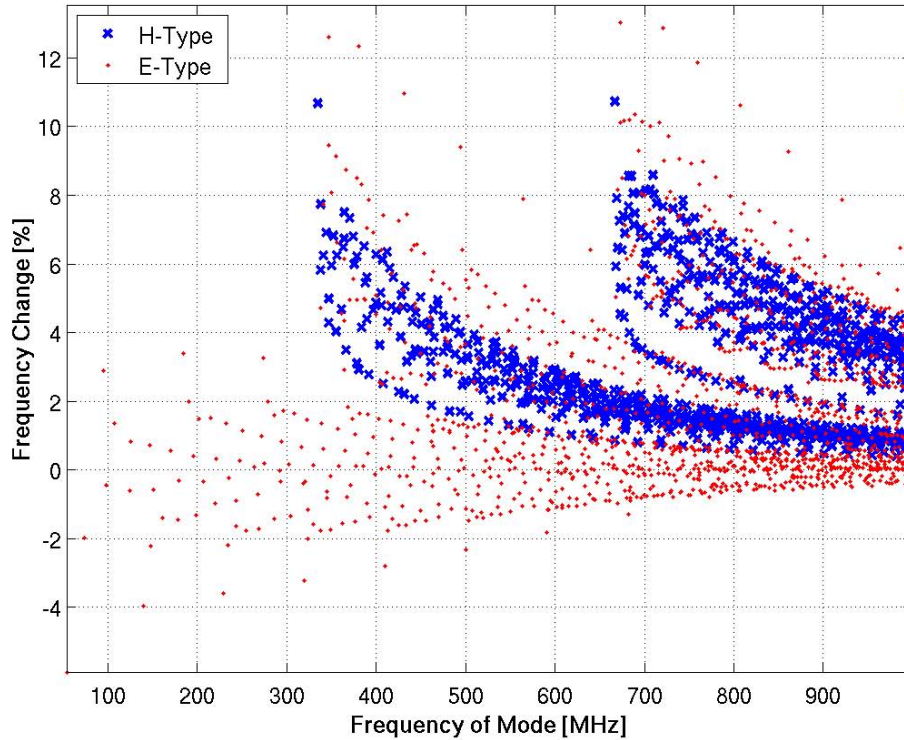
Figure A.3: **Frequency change due to cavity shape deformation**

A.2 Resonance Frequency Correction by Slater's Formula

The perturbation calculation according to *Slater* [68] gives the relation of boundary deformation to the resonance frequency change of a cavity.

$$\omega^2 = \omega_n^2 \left[1 + \int_{\Delta V} \left(|\vec{h}_n|^2 - |\vec{e}_n|^2 \right) dx^3 \right] \tag{A.17}$$

with the volume difference ΔV of undeformed to deformed volume. Fig. A.3 shows the correction factor of the resonance frequency for a small modification in cavity shape. The cavity electrodes are approximated by small brick shaped objects. Effects of the air pressure to the large surface of the cavity are represented as sinusoidal deformation of this boundary with $\Delta z(x,y) = 1.4325cm \cdot \sin(\pi x/b)\sin(\pi y/a)$. The surface integral of the field energy on the boundary times $\Delta z(x,y)$ is evaluated by *Maple* [18] for the calculation of the displaced volume integral (A.17).
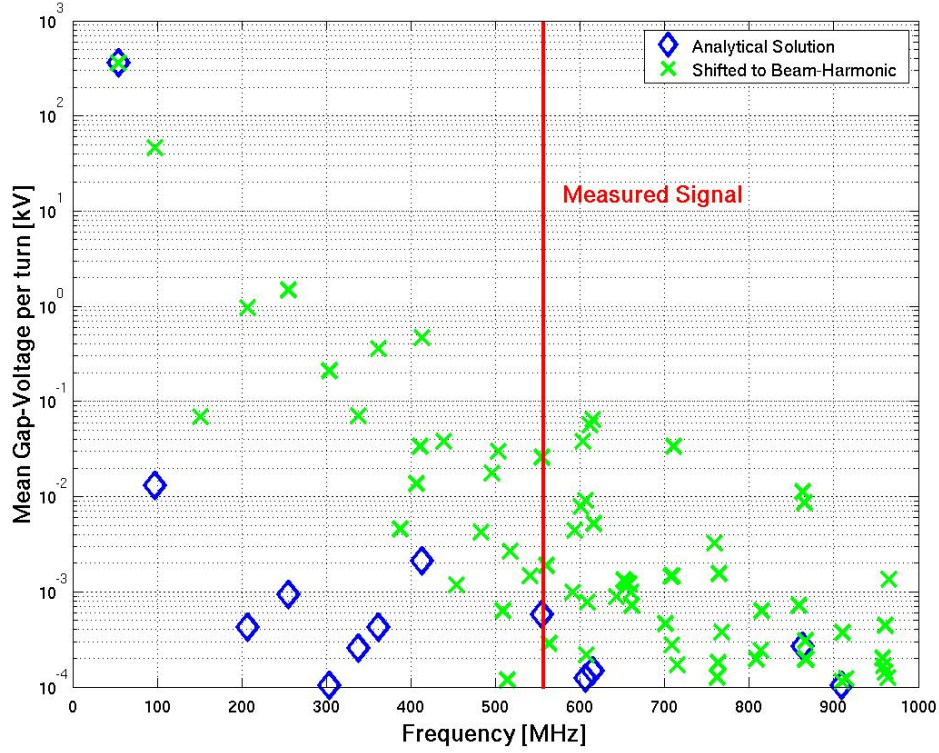
Figure A.4: **Gap voltages of beam excited modes.** The beam current is 1mA.

A.2.1   The Cavity Mode Model

The parameters C, K and L in equations (2.57) to (2.59) can now be calculated by inserting the electric field distribution (A.2) of E-type modes for the case of an excitation by a Gaussian beam distribution. With particle motion along the cavity z-axis

$$C^{(l,m,n)} = \begin{cases} d\alpha_{l,m,n} I_0 \sum_i \sin\left(\frac{\pi l x_i}{b}\right) \sin\left(\frac{\pi m}{2}\right) & \text{if } n = 0 \\ 0 & \text{if } n > 0 \end{cases} \tag{A.18}$$

for a normalization factor $\alpha \equiv c^2 \mu_0 A(k^2 - k_z^2)\sqrt{\varepsilon_0/(2U)}$ and DC beam current I_0

$$\boldsymbol{K}_{m'}^{(l,m,n)} = (-1)^n \beta \sum_i v_i \sin\left(\frac{\pi l x_i}{b}\right) \frac{\sin\left(\frac{m'\omega_0 d}{v_i}\right)}{(m'\omega_0 d)^2 - (\pi n v_i)^2} \cdot e^{-\frac{(m'\omega_0 \sigma_i)^2}{2v_i^2}} \tag{A.19}$$

$$\boldsymbol{L}_{m'}^{(l,m,n)} = \beta \sum_i v_i \sin\left(\frac{\pi l x_i}{b}\right) \frac{1N(-1)^n \cos\left(\frac{m'\omega_0 d}{v_i}\right)}{(m'\omega_0 d)^2 - (\pi n v_i)^2} \cdot e^{-\frac{(m'\omega_0 \sigma_i)^2}{2v_i^2}} \tag{A.20}$$

$$\beta \equiv 2I_0 \alpha_{l,m,n} m' \omega_0 d^2 \sin\left(\frac{\pi m}{2}\right) \tag{A.21}$$

where the superscripts (l, m, n) indicate the corresponding mode and m' the Fourier component.

The simplified model of a cyclotron with relativistic particle motion and linearly increasing vertical static magnetic field $\mathfrak{B}_i$ in function of the radius r_i gives a recursive expression for the positions x_i, velocities v_i and relativistic correction γ_i of the particle bunches with charge q and mass m_0. The Lorentz equation leads to the expression for the trajectories in the static magnetic field. Parameters are determined by the injection and extraction energies, minimum and maximum radii and total number of turns.

$$r_i = \frac{\gamma_i m_0 v_i}{q \mathfrak{B}_i} \qquad\qquad r_i = x_i + r_C \qquad\qquad \Delta U_i = N_C q \hat{V}_G \sin(k_z z_i) \qquad \text{(A.22)}$$

with energy gain ΔU_i on turn i in a cyclotron with N_C box shaped cavities, each having a gap voltage $\hat{V}_G$. The new total energy W_{i+1} and the velocity can now be calculated by

$$W_{i+i} = W_i + \Delta U_i \qquad\qquad\qquad \frac{v_{i+1}}{c} = \sqrt{1 - \left(\frac{m_0 c^2}{W}\right)^2} \qquad \text{(A.23)}$$

Introducing into equation (A.22) gives the new positions r_{i+1}. The positions of the particles and the velocities can now be used to calculate the interaction sums in (A.21) and (A.20). The remaining modes, which could be excited significantly by the beam are summarized in figure A.4. Only modes with a difference in (Slater-corrected) resonance frequencies to the next beam harmonic of less than 5MHz are considered. In order to get an estimate of the upper bound the values are indicated also for the case with resonance shifted exactly to the beam harmonic.

This cavity mode model applies only to frequencies below cutoff of the beam slots. For a top-bottom symmetric cavity, one has the condition that the electric field in the beam plane must either be perpendicular or parallel to the beam plane. Only the second type of modes can be excited by the beam current. In the case of beam slots, the propagation of modes out of the cavity depends on the coupling of the cavity fields to the beam slot. But this coupling depends on the polarization of the fields. The cutoff frequency where all polarizations can propagate into the beam slot is estimated by $f_C = c/(2L_{WG})$ with beam slot height of $L_{WG} = h_{WG} \approx 4cm$ leading to $f_{CV} \approx 3.7GHz$ and with beam slot width of $L_{WG} = w_{WG} \approx 2.66m$ leading to $f_{CH} \approx 56.4MHz$.

Appendix B

List of Calculated Modes

B.1   Cavity Modes

f_0 [MHz]		Q_0 [-]	in Cavity	Voltage $[kV/pC]$	
51.0404	50.63281	29'130	C1	8.97	4'100
51.0405	50.63281	29'130	C2	8.97	4'100
51.0405	50.63281	29'130	C3	8.97	4'100
51.0406	50.63281	29'130	C4	8.91	4'100
72.2332		33'310	C1	8.01E-4	
72.2332		33'335	C2	8.13E-4	
72.2332		33'328	C3	7.85E-4	
72.2332		33'160	C4	8.27E-4	
97.7344		37'415	C1	0.132	
97.7344		37'544	C2	0.193	
97.7344		34'367	C3	0.134	
97.7344		37'081	C4	0.338	
122.938		41'817	C1	3.34E-3	
122.938		41'893	C2	5.74E-3	
122.938		42'032	C3	8.24E-3	
122.940		17'028	C4	7.32E-3	
132.306		44'790	C1	0.178	
132.306		44'780	C2	0.143	
132.306		44'780	C3	0.137	
132.306		44'797	C4	0.143	
143.694		47'236	C1	6.25E-3	
143.694		47'245	C2	6.94E-3	
143.694		45'847	C3	5.87E-3	
143.694		47'276	C4	6.19E-3	
149.549		44'759	C1	5.68E-5	
149.547		45'313	C2	1.02E-3	
149.550		40'931	C3	5.27E-3	
149.547		45'657	C4	5.24E-2	

150.773	151.8	29'716	C5	6.40	3'200
206.091		54'859			7.52E-2
206.098		54'910			2.40E-3
206.099		54'752			6.87E-4
206.099		53'211			1.22E-2
247.903		58'032			3.38E-7
247.913		49'672			1.58E-5
247.917		50'122			1.83E-4
247.960		53'641			8.16E-6
250.086		60'867			1.68E-2
250.086		60'736			1.07E-3
250.087		60'634			9.48E-2
250.087		60'507			2.28E-2
260.372		4'116			4.48E-2
307.923		10'117	C5		5.05E-2
558.147		6'911	C5		5.97E-2

Table B.1: **Cavity modes:** Mode at C4 122.9MHz couples to C1 & C3 therefore lowering of Q_0. The eigenmodes at 149.5MHz have field-energy in C1 to C4. Resonance frequency C1-C5 are also tuned to operation frequency.

B.2 Vacuum Chamber Modes

f_0 [MHz]	Q_0 [-]	Voltage $[kV/pC]$
54.6845	1'368	1.90E-6
54.7435	5'093	1.14E-4
55.2631	122.9	5.17E-5
55.4508	1'796	6.02E-6
57.4763	1'269	7.15E-5
58.6990	4'918	2.51E-6
58.7656	5'191	1.46E-4
59.0168	5'510	2.46E-5
73.6273	103.9	6.60E-5
76.4437	4'486	5.01E-5
76.5666	750.1	6.65E-5
77.8727	2'425	7.17E-5
78.5503	140.7	9.29E-5
81.9829	2'379	2.51E-5
82.7765	3'959	7.78E-5
83.9048	4'727	1.54E-5
91.7687	171.5	1.88E-4
96.8376	156.4	3.63E-4

Table B.2: **Vacuum chamber modes:**

B.3 Mixed Modes

f_0 [MHz]	Q_0 [-]	Voltage $[kV/pC]$
101.056	14'015	1.11E-5
101.787	4'377	1.47E-5
102.491	15'948	4.36E-5
102.924	2'362	2.95E-4
103.932	9'333	1.55E-5
103.994	7'797	2.72E-4
104.276	5'949	2.87E-5
104.674	8'769	7.26E-5
106.981	6'543	1.64E-6
107.280	6'453	8.08E-7
108.327	9'881	1.96E-6
110.814	2'495	5.37E-5
111.118	3'384	1.30E-5
111.607	552.9	2.63E-4
111.919	3'989	5.67E-5

114.024	5'549	6.94E-6
114.998	1'977	2.91E-5
115.305	6'308	3.29E-5
116.003	5'703	1.78E-5
122.720	328.9	1.51E-4
124.459	4'106	6.13E-5
124.588	3'786	7.82E-5
125.404	15'035	6.02E-7
125.848	302.1	2.61E-5
127.070	3'329	6.74E-6
127.204	9'397	4.66E-6
127.902	1'220	5.35E-5
128.422	10'806	2.98E-6
130.699	7'681	8.06E-5
130.917	8'675	2.84E-4
131.596	9'332	5.27E-6
136.412	2'487	2.18E-5
147.904	22'177	1.78E-4
148.055	19'735	7.58E-6
148.426	22'993	1.38E-5
148.640	4'571	1.76E-5
152.380	11'695	1.43E-5
152.413	12'209	2.65E-4
154.385	11'300	5.59E-5
154.751	7'583	1.54E-4
155.170	1'040	6.37E-5
157.474	11'055	5.72E-6
157.481	11'060	7.21E-6
195.499	34'918	1.49E-05
195.565	30'423	1.55E-04
195.763	41'908	2.33E-04
195.929	33'471	3.03E-05
196.830	4'434	7.33E-06
197.085	14'334	1.21E-05
203.093	17'121	6.80E-05
203.093	16'939	1.36E-04
203.602	41'735	2.31E-05
203.665	39'359	8.16E-06
203.767	35'609	6.05E-06
203.815	33'697	2.81E-05
205.222	15'604	9.14E-05
205.942	3'883	7.59E-05
207.763	16'378	4.99E-05
207.766	16'348	5.72E-06

245.756	19'876	5.75E-07
246.657	15'675	1.17E-06
253.090	44'965	3.92E-03
253.171	36'626	2.58E-02
253.234	38'961	1.72E-01
253.312	31'609	2.98E-02
255.974	30'008	2.33E-06
258.843	16'027	5.72E-06
258.853	16'356	6.38E-06
259.027	12'908	6.58E-06
259.111	27'459	1.09E-05
299.351	53'189	1.24E-02
299.804	20'156	3.62E-04
299.810	20'082	5.37E-05
300.345	16'768	1.41E-04
302.111	38'194	4.51E-04
302.300	51'376	4.20E-04
302.318	42'991	1.54E-03
302.372	48'735	3.32E-03
302.624	22'484	8.75E-04
303.486	17'549	1.70E-04
303.707	17'106	4.48E-04
303.718	18'028	1.06E-05
306.635	7'416	7.43E-06
306.661	14'847	5.21E-05
307.210	864	1.37E-05
308.139	59'786	1.83E-01
308.144	61'455	2.31E-01
308.144	61'556	1.40E-01
308.146	58'508	8.84E-02
353.870	23'473	6.78E-04
354.403	43'787	1.16E-01
354.425	44'921	3.88E-02
354.455	39'523	4.07E-01
354.499	37'027	3.92E-01
354.577	26'652	2.62E-02
354.592	36'477	2.46E-02
354.607	42'937	6.04E-02
354.621	48'533	1.13E-01
354.811	24'338	6.47E-04
354.813	30'127	4.08E-03
354.868	42'394	1.02E-02
354.885	40'431	2.99E-02
354.956	16'375	5.65E-02

354.983	15'718	8.20E-04
355.422	17'616	1.55E-03
355.568	18'674	5.42E-02
355.575	29'563	1.18E-01
355.576	39'668	8.60E-02
355.585	31'206	3.81E-03
404.021	31'005	6.78E-03
404.052	42'239	1.68E-03
404.057	39'092	8.05E-03
404.071	54'834	3.22E-03
404.181	20'593	2.06E-03
404.278	7'505	4.96E-03
404.491	48'874	1.85E-02
404.491	67'741	3.10E-02
404.492	64'038	2.16E-03
404.507	39'345	1.24E-03
404.953	4'545	8.28E-02
404.998	63'177	3.13E-01
405.024	33'348	4.57E-02
405.043	38'035	4.12E-02
405.123	22'852	2.07E-02
405.683	3'583	2.09E-03
406.036	4'127	1.97E-05
406.090	8'302	2.77E-05
406.202	55'755	8.78E-03
406.236	41'588	2.83E-03
454.545	28'824	7.62E-04
454.577	22'778	3.27E-05
454.643	42'950	1.82E-03
454.744	8'929	3.04E-04
454.909	22'249	7.11E-04
455.101	23'032	4.19E-04
455.477	5'184	2.87E-03
455.585	16'156	1.13E-03
455.848	51'587	2.88E-03
455.889	58'139	3.10E-03
455.905	48'246	6.87E-05
455.932	50'658	8.49E-03
456.288	24'355	1.54E-03
456.475	11'823	4.04E-04
456.686	10'163	2.46E-04
456.774	3'558	5.09E-04
456.856	17'874	2.73E-04
456.926	48'336	5.09E-03

456.936	55'679	5.29E-03
456.940	48'479	4.96E-05
505.391	17'134	2.21E-04
505.499	28'780	1.15E-04
505.508	37'572	2.20E-05
505.603	59'206	1.68E-04
505.687	37'555	3.98E-05
505.765	19'945	1.04E-03
505.938	23'251	8.77E-05
506.045	22'977	5.67E-04
506.175	17'553	4.49E-03
506.466	27'769	5.31E-03
506.780	32'508	4.11E-04
506.826	32'038	2.99E-03
506.865	55'774	2.22E-03
506.881	64'121	4.93E-03
506.928	30'833	4.01E-03
507.001	52'430	5.20E-04
507.051	54'721	1.21E-03
507.063	61'397	7.00E-04
507.096	33'247	3.62E-04
507.192	36'450	5.96E-04
555.441	37'246	1.71E-04
555.552	19'880	6.46E-04
555.663	20'659	3.12E-04
555.815	17'100	9.54E-05
555.912	45'270	6.67E-04
555.950	34'036	8.31E-04
556.015	32'249	4.70E-04
556.182	42'989	1.89E-03
556.536	10'089	2.67E-03
556.606	984	1.44E-05
556.679	34'070	5.60E-03
556.949	31'293	8.83E-03
557.106	30'379	3.21E-02
557.142	56'256	5.53E-02
557.158	46'589	5.91E-03
557.169	36'434	1.32E-02
557.502	14'846	9.37E-04
557.674	62'014	5.23E-03
557.693	70'016	1.25E-03
557.700	20'506	3.00E-04
557.749	4'439	4.91E-03
557.948	31'610	3.55E-04

557.995	672	1.77E-04
558.039	19'039	1.16E-04
558.259	20'658	4.46E-04
558.396	1'946	4.52E-04
558.508	58'318	6.95E-05
558.525	48'094	1.36E-04
558.542	23'327	4.64E-06
606.526	942	2.37E-03
606.538	1'986	9.91E-05
606.697	13'692	4.23E-03
606.704	41'432	2.43E-04
606.716	9'901	1.91E-03
606.758	45'246	6.16E-03
607.203	27'973	7.98E-04
607.339	7'485	1.31E-03
607.540	19'992	1.51E-03
607.621	34'440	5.21E-02
607.707	25'169	7.76E-04
607.779	3'466	2.01E-03
607.917	9'707	1.79E-03
607.990	31'649	3.02E-04
608.014	37'071	1.17E-04
608.038	48'412	2.34E-02
608.079	18'517	4.01E-03
608.255	44'853	3.27E-03
608.480	7'408	1.48E-03
608.581	13'204	1.45E-04

Table B.3: **Mixed modes:** The four modes at 308.1MHz and 355.6MHz are main cavity modes which couple strongly to the vacuum chamber.

Appendix C

Reduced Variables for Numerical Computation

Position of the particles in the fixed laboratory frame:

$$\tilde{\mathsf{xxpt}}_{i=0,2,4}[mm] = 1000 \cdot x_{i=1,2,3}[m] \qquad \text{(C.1)}$$

Momentum of the particles in Cyclotron Units in the fixed laboratory frame depend on speed of light c, momentum p and rest energy of the particle E_0 in SI-units:

$$\tilde{\mathsf{xxpt}}_{i=1,3,5}[CU] = \frac{c}{E_0} \cdot p_{i=1,2,3}[-] \qquad \text{(C.2)}$$

$$\frac{cp}{E_0} = \beta\gamma \qquad \text{(C.3)}$$

$$\gamma^2 = 1 + \sum_{i=1,3,5} \tilde{\mathsf{xxpt}}_i^2 \qquad \text{(C.4)}$$

Magnetic field in kilo Gauss:

$$\tilde{\mathsf{bfld}}[kG] = 10 \cdot B[T] \qquad \text{(C.5)}$$

Particle charge in pico Coulomb:

$$\tilde{\mathsf{QBUNCH}}[pC] = 10^{12} \cdot q[C] \qquad \text{(C.6)}$$

Time steps in nano seconds:

$$\tilde{\mathsf{dt}}[ns] = 10^9 \cdot dt[s] \qquad \text{(C.7)}$$

Bibliography

[1] S. Adam, *Methoden zur Berechnung der longitudinalen Raumladungs-Effekte in Isochronzyklotrons*, Thesis ETHZ 7694, (1985).

[2] S. Adam, *Space Charge Effects in Cyclotrons - From Simulations to Insights*, 14th Cyclotron Conference, Cape Town , pp. 446, (1995).

[3] A. Adelmann, *3D Simulations of Space Charge Effects in Particle Beams*, Thesis ETHZ, (2002).

[4] A. Adelmann et al., *Recent Results on Simulations of High Intensity Beams in Cyclotrons*, Proceedings Cyclotrons 2004 Conference Tokyo, (2004).

[5] ANSYS, Inc., Southpointe, 275 Technology Drive, Canonsburg, PA 15317.

[6] P. Arbenz and W. Petersen, *Introduction to Parallel Computing*, Oxford Univ. Press, (2004).

[7] Z. Bai et al., *Templates for the Solution of Algebraic Eigenvalue Problems, A Practical Guide*, SIAM, Philadelphia, 2000.

[8] P. Balleyguier, *A Straightforward Method for Cavity External Q Computation*, Particle Accelerators, Vol. 57, pp. 113-127, (1997).

[9] P. Balleyguier, *External Q Studies for APT SC-Cavity Couplers*, Proceedings LINAC-2000 Conference, (2000).

[10] C. K. Birdsall, *Plasma Physics via Computer Simulation*, McGraw-Hill Book Company International Student edition, (1985).

[11] J.P. Blaser and H. Willax, *Progress report on the 500MeV isochronous cyclotron.*, Gatlinburg conference on isochronous cyclotrons, IEEE, Nuclear Science-13, Nr.4, pp.194, (1966).

[12] J.P. Blaser, *Strahlbelastung der Kavitaeten und Phaseninstabilitaeten*, PSI Note (April 1967).

[13] H.G. Blosser, *Sectored Cyclotrons*, Particle Accelerators Conference 1965, IEEE Trans. Nucl. Science-12 pp. 985.

[14] H. Blosser and M. Gordon, Nucl. Instr. Meth. **13**, 106, (1961).

[15] M. Bopp et al., *Coupled Field Analysis of the New Ring Cyclotron Cavity,* PSI scientific and Technical Report 2001, VI, pp. 9-10, (2002).

[16] D. Boussard, *Beam Loading*, Proceedings CERN Accelerator School 5th Advanced Accelerator Physics Course, 1995, pp. 415-435.

[17] H. Bruck, *Accélérateurs circulaires de particules*, Presses Universitaires de France (1966).

[18] B.W. Char, *Maple V, First Leaves: A Tutorial Introduction to Maple V*, Springer-Verlag, (1992).

[19] A.W. Chao, *Physics of Collective Beam Instabilites in High Energy Accelerators*, John Wiley and Sons, (1993).

[20] R.E. Collin, *Guided Waves*, IEEE Press, (1991).

[21] CUBIT-Homepage, http://cubit.sandia.gov

[22] J. Duppich et al., *A New and Dedicated Accelerator and Beam Transport System for Proton Therapy at the Paul Scherrer Institute (PSI)/Switzerland*, Poster presented at PTCOG01 Conference, November 2001, Tsukuba, Japan.

[23] H. Fitze et al., *Upgrade Concepts of the PSI Accelerator RF-Systems for a projected 3mA Operation*, Cyclotrons 2001 Conference, East Lansing, pp.300-302, (2001).

[24] M. Frigo et al., *FFTW: An adaptive software architecture for the FFT*, Proc. of ICASSP, Volume 3, (1998).

[25] M.A. Fuhrmann, *Compact Complex Expressions for the Electric Field of 2-D Elliptical Charge Distributions*, Am. J. Phys. **62**(12), 1994, pp. 1134-1140, PEP-II/AP Note 34-93.

[26] R. Geus, *The Jacobi-Davidson algorithm for solving large sparse symmetric eigenvalue problems with application to the design of accelerator cavities*, Thesis ETHZ No. 14734, (2002).

[27] R. Geus et al., *PYFEMAX: A Python Finite Element Maxwell Solver*, PSI scientific and Technical Report 2002, VI, pp.51-53, (2003).

[28] M.M. Gordon, Nuclear Instruments and Methods, 18/19, pp. 268, (1962).

[29] G. Goubau, *Elektromagnetische Wellenleiter und Hohlräume*, Wissenschaftliche Verlagsgesellschaft M.B.H. Stuttgart, (1955).

[30] W. Greiner, *Klassische Elektrodynamik*, Theoretische Physik, Vol 3, Verlag Harri Deutsch, (1991).

[31] W. Greiner, *Spezielle Relativitätstheorie*, Theoretische Physik, Vol 3A, Verlag Harri Deutsch, pp.206, (1992).

[32] H. Haf et al., *Höhere Mathematik für Ingenieure*, B. G. Teubner Stuttgart, (1993).

[33] R.W. Hockney et al., *Computer Simulation Using Particles*, McGraw-Hill International Book Company, (1980).

[34] R.W. Hockney and J.W. Eastwood, *Computer Simulation Using Particles*, McGraw-Hill International Book Company, (1981).

[35] J.D. Jackson, *Classical Electrodynamics*, John Wiley & Sons, (1975).

[36] W. Joho, *Tolerances for the SIN Ring-Cyclotron*, SIN Report TM-11-4, March 1968.

[37] W. Joho, *High Intensity Problems in Cyclotrons*, 9th Cyclotron Conference Caen, pp.337, (1981).

[38] A. Kabel, *Maxwell-Lorentz Equations in General Frenet-Serret Coordinates*, Proceedings of the Particle Accelerator Conference 2003, (2003).

[39] D. Kajfez, *Q Factor*, Vector Fields, (1994).

[40] D. Keefe (Editor), *Impedance Beyond Cutoff*, Particle Accelerators, Gordon and Breach Science Publishers, Special Issue, Vol. 25 #(2-4), (1990).

[41] S.R. Koscielniak and S. Adam, *Simulation of Space-Charge Dominated Beam Dynamics in an Isochronous AVF Cyclotron*, Proceedings Particle Accelerator Conference 1993, (1993).

[42] Y.Y. Lau and D. Chernin, *A Review of the AC space-charge effect in electron-circuit interactions*, Phys. Fluids B, **4**, 11, pp.3473, (1992).

[43] L.Q Lee et al., *Solving Large Sparse Linear Systems in End-to-End Accelerator Simulations* SLAC-PUB-10320, (2004) See also URL http://www-group.slac.stanford.edu/acd.

[44] G.E. Lee-Whiting, *Beam-Cavity Interactions in the SOC*, Proceedings of Symposium on Separated Orbit Cyclotrons and Beam-Cavity Interactions, oxford, July 1966, RHEL/M 124, pp.13-28, (1966).

[45] Z. Li et al., *High Performance Computing in Accelerator Structure Design and Analysis*, Submitted to Nuclear Instruments and Methods A, (2004).

[46] The MAFIA-Collaboration, *User's Guide MAFIA Version 4.00,* CST GmbH, Lauteschlägerstr. 8, D-64289 Darmstadt, Germany, (1997). See also URL http://www.cst.de.

[47] F. Marti et al, *Analysis of a Cyclotron Based 400 MeV/u Driver System for a Radioactive Beam Facility*, Michigan State University Cyclotron Laboratory Report 1131, (August 1999).

[48] F. Marti et al, *Study of Space Charge Effects Using a Small Storage Ring that Works in the Isochronous Regime*, Cyclotrons 2004 Conference, Tokyo, to be published, (2004).

[49] *MeshTV Getting Started Manual*, UCRL-MA-127441 Rev.1, Version 4.3, (2002). http://www.llnl.gov/bdiv/meshtv/.

[50] S. Meyers, *Effektiv C++ programmieren*, 3. Auflage, Addison-Wesley, (1998).

[51] C. Misner, K.S. Thorne and J.A. Wheeler, *Gravitation*, W.H. Freeman and Company, San Francisco, (1973).

[52] http://www.hpfem.jku.at/netgen/

[53] A. Novokhatski, *Self-consistent Model for the beams in accelerators*, Proc. ICAP'98, Monterey Ca., USA, September 1998.

[54] F. Pedersen, *Beam Loading Effects in the CERN PS Booster*, IEEE Trans. Nucl. Sci. Vol. 22, No. 3, 1975.

[55] K. Pöschl, *Mathematische Methoden in der Hochfrequenztechnik*, Springer Verlag, (1956).

[56] E. Pozdeyev, *A Fast Code for Simulation of the Longitudinal Space Charge Effect in Isochronous Cyclotrons*, Cyclotrons 2001 Conference, East Lansing, pp.411-413, (2001).

[57] W.H. Press et al, *Numerical recipes in C++: the Art of Scientific Computing*, 2nd edition, Cambridge University Press, (2002).

[58] P. Ramachandran, *MayaVi: A free tool for CFD data visualization*, 4th Annual CFD Symposium, Aeronautical Society of India, August, (2001).

[59] M. Reiser, *Theory and Design of Charged Particle Beams*, John Wiley and Sons, (1994).

[60] F. Reuse, Lecture Notes EPFL, *Introduction à l'electrodynamique et à l'optique quantique*, EPFL Repro.

[61] J.R. Richardson, *Sector Focusing Cyclotrons*, Progress in Nuclear Techniques and Instrumentation Vol. 1,edited by F.J.M. Farley, (1965).

[62] K.W. Robinson, *Radiofrequency Acceleration II.* CEA(MIT-Harvard)-11 Report, 1956.

[63] F.M. Russell (Editor), *Proceedings of Symposium on Separated Orbit Cyclotrons and Beam Cavity Interactions*, Oxford, July (1966), RHEL/M 124 Rutherford High Energy Laboratory, Chilton, Didcot, Berkshire.

[64] U. Schryber, *Stabilitätsuntersuchungen einer Beschleunigungskavität unter Strahlbelastung*, PSI Internal-Report TM-04-16, 1970.

[65] W.M. Schulte and H.L. Hagendoorn, *The Theory of Accelerated Particles in Cyclotrons*, Nuclear Instruments and Methods, 171, pp. 409-437, (1980).

[66] W.M. Schulte and H.L. Hagendoorn, *Special Applications of a General Orbit Theory for Accelerated Particles in Cyclotrons*, Nuclear Instruments and Methods, 171, pp. 439-443, (1980).

[67] P. Sigg, *Konische Beschleunigungskavität Messergebnisse am 1:5 Modell*, PSI Note, 4.03/B6 66, (1966).

[68] J.C. Slater, *Microwave Electronics*, D. Van Nostrand Company, (1950).

[69] W.L. Smirnow, *Lehrbuch der hoeheren Mathematik*, Verlag Harri Deutsch, (1995).

[70] T. Stammbach et al., *The Feasibility of High Power Cyclotron*, Nuclear Instruments and Methods B, 144, 1-4, pp.1-7, (1996).

[71] T. Stephani, *PSI SCC Cavity Design - Design Review*, Accel Report 1200-BP-E0898-0, December 2001.

[72] T. Stephani, *PSI SCC Lumped Circuit Model - Design Review*, Accel Report 1200-BP-E0886-0, December 2001.

[73] L. Stingelin, *Beam-Cavity Interactions in High-Intensity Cyclotrons*, PSI scientific and Technical Report 2002, VI, (2003).

[74] L. Stingelin et al., *Beam-Cavity Interaction Simulation for the PSI Ring-Cyclotron*, Proceedings Cyclotrons 2004 Conference Tokyo, (2004).

[75] L. Stingelin, *Computational Electrodynamics on the LINUX-Cluster*, PSI scientific and Technical Report 2001, VI, p.26, (2002).

[76] Y. Sun, *The Filter Algorithm for Solving Large-Scale Eigenproblems from Accelerator Simulations*, Thesis Stanford University, (2003).

Curriculum Vitae

Personal Information

Name	Lukas STINGELIN
Date of Birth	28th of June 1972
Nationality	Swiss
Citizen of	Muttenz BL

Education and Training

2001-2004	PSI, Villigen and CRPP, ETH Lausanne
Position held	PhD student in the PSI rf group
1995-2000	Swiss Federal Institute of Technology, Lausanne
Title of qualification awarded	Physicist ETH Lausanne Plasma physics, master thesis: Discharge phenomena of the PSI high power rf-window
1992-1995	Minerva Institute, Basel
Title of qualification awarded	Swiss federal maturity type C (scientific)
1988-1992	Emil Haefely & Cie AG, Basel
Title of qualification awarded	Electronics technician

Work Experience

2000-2001	Paul Scherrer Institute, Villigen
Occupation or position held	Physicist Elaboration of subject for PhD-thesis, Design of rf-structures
1993-1994	Bank Sarasin & Cie AG, Basel
Occupation or position held	50%-position as timekeeping controller
1992	Emil Haefely & Cie AG, Basel
Type of business or sector	High voltage test systems
Occupation or position held	50%-position as electronics technician